Time analysis and clock characterization for bi-static radar for asteroid tomography

Ricardo Granados Alfaro

Communauté
UNIVERSITÉ Grenoble Alpes

THÈSE

Pour obtenir le grade de

DOCTEUR DE LA COMMUNAUTE UNIVERSITE GRENOBLE ALPES

Spécialité : **OPTIQUE ET RADIOFREQUENCES**

Arrêté ministériel : 25 mai 2016

Présentée par

Ricardo GRANADOS ALFARO

Thèse dirigée par **Etienne LE COARER, Ingénieur de Recherche, IPAG**, et
codirigée par **Alain HERIQUE, Maître de Conférences, IPAG**

préparée au sein du **Laboratoire Institut de Planétologie et d'Astrophysique de Grenoble**
dans **l'École Doctorale Electronique, Electrotechnique, Automatique, Traitement du Signal (EEATS)**

Analyse de temps et characterization d'horloges pour un radar bistatique pour la tomographie d'astéroïdes.

Time analysis and clock characterization for bi-static radar for asteroid tomography.

Thèse soutenue publiquement le **7 novembre 2019**,
devant le jury composé de :

Monsieur BERNARD SCHMITT
DIRECTEUR DE RECHERCHE, CNRS DELEGATION ALPES, Président
Monsieur, ALAIN REINEIX
DIRECTUER DE RECHERCHE, SNRS CENTRE-LIMOUSIN-POITOU-CHARENTES, Rapporteur
Monsieur, ENRICO RUBIOLA
PROFESSEUR, INSTITUT FEMTO-ST and INRIM, TORINO, ITALY, Rapporteur
Monsieur, ETIENNE LE COARER
INGENIEUR DE RECHERCHE, UNIVERSITE GRENOBLE ALPES, Directeur de thèse
Monsieur, ALAIN HERIQUE
MAITRE DE CONFERENCES, UNIVERSITE GRENOBLE ALPES, Co-directeur de thèse
Monsieur, DIRK PLETTEMEIER
PROFESSEUR, UNIVERSITE TECHNIQUE DRESDEN – ALLMAGNE, Examinateur
Monsieur, WLODEK KOFMAN
DIRECTEUR DE RECHERCHE, CNRS DELEGATION ALPES, Invité
Monsieur, KARL SCHUSTER
DIRECTEUR DE RECHERCHE, IRAM, Invité

“Nothing is yours. It is to use. It is to share. If you will not share it, you cannot use it.”

— Ursula K. Le Guin, The Dispossessed

Abstract

Keywords: Asteroid; Tomography; Radar; Bi-static; Time Analysis; Clock; OCXO

Small bodies, like comets and asteroids, are of interest for the study of the origin of the Solar System since they have experienced little changes throughout time. Therefore, by understanding their evolution we can learn about the evolution of the Solar System itself. This information can be useful for future space exploration or for planetary defense. Nowadays, there are several space missions studying or about to study small bodies, but only a few instruments are destined to study the interior of small body cores.

Radio waves interact with the medium they are propagating through and will undergo different modifications depending on the properties of the material. Therefore, radar is the ideal method to study the internal structure of an asteroid. The wave's properties, such as its velocity, will be affected by its travel through the nucleus dependent on the dielectric properties of the asteroid. We propose a new bi-static low-frequency radar (LFR) based on the instrument CONSERT which was onboard the Rosetta mission. This LFR primary objective is to measure the propagation delay between two electronics, one posed on the asteroid's surface and the other orbiting around it. The signal will be transmitted through the body's nucleus and will be affected by its composition and heterogeneity. By measuring different signal characteristics, such as the propagation delay, we can deduce the composition properties of the object.

The main objective of this thesis is to study and understand how the clock drift between radar electronics will affect the measurement of the propagation delay in order to propose compensation methods to improve science return. The initial step of the thesis is to provide an understanding of the clock signal generation and how the stability of the signal will be affected over time by different processes like temperature, the voltage supply, or aging. To understand how these instabilities will impact the propagation delay measurement, we analyze the long scale drift of radar instruments. For this, we developed a time model of the radar based on time events. The model was used to build a simulator using a simple model of the clock signal generation. With this simulator, we show that the time errors have a different effect on the bi-static radar at different time scales, but that these different time scales are correlated. We propose a method to estimate clock drift from radar data to compensate for time errors.

To validate the model, a test bench is designed and developed measuring time differences between two clocks. Using the test bench data as input for the simulator allows to estimate the impact on instrument performances and to estimate performances of the compensation methods. The data from the test bench is used for the validation of the selected clocks for the mission and will be used for their characterization. This clock characterization will help to improve the simulator for different tests, as we can include the real models for frequency instabilities.

To conclude, we present the limitations of the compensation methods, as well as the improvements in the electronic design and operation of the instrument as a result of the time analysis.

Résumé

Les petits corps, comme les comètes et les astéroïdes, présentent un intérêt pour l'étude de l'origine du système solaire, car ils n'ont connu que peu de changements au fil du temps. Par conséquent, en comprenant leur évolution, nous pouvons en apprendre davantage sur l'évolution du système solaire lui-même. Cette information peut être utile pour une future exploration spatiale ou pour la défense planétaire. De nos jours, plusieurs missions spatiales étudient ou sont sur le point d'étudier les petits corps, mais seuls quelques instruments sont destinés à étudier l'intérieur des petits corps.

Les ondes radio interagissent avec le milieu à travers lequel elles se propagent et subiront différentes modifications en fonction des propriétés du matériau. Par conséquent, le radar est la méthode idéale pour étudier la structure interne d'un astéroïde. Les propriétés de l'onde, telles que sa vitesse, seront affectées par son parcours dans le noyau en fonction des propriétés diélectriques de l'astéroïde. Nous proposons un nouveau radar bi-statique à basse fréquence (LFR) basé sur l'instrument CONSERT embarqué dans la mission Rosetta. L'objectif principal de ce LFR est de mesurer le temps de propagation entre deux composants électroniques, l'un posé sur la surface de l'astéroïde et l'autre en orbite autour de celui-ci. Le signal sera transmis à travers le noyau du corps et sera affecté par sa composition et son hétérogénéité. En mesurant différentes caractéristiques du signal, telles que le délai de propagation, nous pouvons en déduire les propriétés de composition de l'objet.

L'objectif principal de cette thèse est d'étudier et de comprendre comment la dérive d'horloge entre les électroniques de radar affectera la mesure du temps de propagation afin de proposer des méthodes de compensation pour améliorer le retour scientifique. La première étape de la thèse consiste à fournir une compréhension de la génération du signal d'horloge et de la manière dont la stabilité du signal sera affectée dans le temps par différents processus tels que la température, l'alimentation en tension ou le vieillissement. Pour comprendre l'impact de ces instabilités sur la mesure du délai de propagation, nous analysons la dérive à grande échelle des instruments radar. Pour cela, nous avons développé un modèle temporel du radar basé sur des événements temporels. Le modèle a été utilisé pour construire un simulateur à l'aide d'un modèle simple de génération de signaux d'horloge. Avec ce simulateur, nous montrons que les erreurs de temps ont un effet différent sur le radar bi-statique à différentes échelles de temps, mais que ces différentes échelles de temps sont corrélées. Nous proposons une méthode pour estimer la dérive de l'horloge à partir des données radar afin de compenser les erreurs de temps.

Pour valider le modèle, un banc de test est conçu et développé en mesurant les différences de temps entre deux horloges. En utilisant les données du banc d'essai comme entrée pour le simulateur permet d'estimer l'impact sur les performances des instruments et d'estimer les performances des méthodes de compensation. Les données du banc d’essai sont utilisées pour la validation des horloges sélectionnées pour la mission et seront utilisées pour leur caractérisation. Cette caractérisation d'horloge aidera à améliorer le simulateur pour différents tests, car nous pouvons inclure les modèles réels d'instabilités de fréquence.

Pour conclure, nous présentons les limites des méthodes de compensation, ainsi que les améliorations apportées à la conception électronique et au fonctionnement de l'instrument à la suite de l'analyse temporelle.

Dedication

A mi familia, mi mamá, mi papá y mi hermana, que siempre estuvieron ahí y me han apoyado durante toda mi vida. Sin ellos, no estaría donde estoy hoy. A Aline, que aunque nuestros caminos se separen, fue un gran apoyo durante el doctorado. Siempre será parte importante de mi vida y tendrá un lugar en mi corazón, además de que hay un Chihuahua que todavía nos une. Por último, al antes mencionado chihuahua, Chilaquil, el chihua, la rata, que a pesar de ser especial, siempre tiene amor incondicional.

In the IPAG laboratory,

Firstly, I would like to give thanks to my supervisor Alain HERIQUE for the project and the help given during my PhD. To Etienne who gave me options for the next step in my professional career. To the radar team: Sonia, Marc, Oriane, and especially Wlodek who gave me insightful comments about my thesis. To Yves who helped me with everything he could.

To the Electronic lab, especially to Sylvain ROCHAT, Bruno TRAVERS and Batist SOUKIASSIAN, who worked with me and help me put the test bench needed for my thesis into reality.

To the people involved in all the administration especially to Valeri CHOPIN and Fabienne BOUCARD, who I asked for help very frequently to solve infinite doubts. And lastly, thanks to all the people that are working in the lab that make this a pleasant place to work, the people in charge of management of the building and the direction of the lab.

For my friends,

In favor of my mental health and anxiety I will keep this part short. The idea of forgetting someone or not mentioning something important will hunt me for the rest of my life. Therefore, I thank all my friends for the support, for the moral sustain, for money support, and for the friendship given that held me stable enough to finish this work and without which it would have been an unbearable burden for myself. I will treasure all of those moments in my heart and you should know that I will be forever yours.

Acknowledgements

The Low Frequency Radar inherits from CONSERT/Rosetta founded by CNES and DLR. The LFR development has been supported by the CNES's R&T program ("CONSERT Next Generation" study) and by the ESA's General Studies Program (AIM Phase A).

The Ph.D. studies were funded by CONACYT-México.

Table of Contents

List of Tables

List of Figures

List of Acronyms

ADC	Analog to Digital Converter
AIDA	Asteroid Impact & Deflection Mission
AIM	Asteroid Impact Mission
AV	Allan Variance
BPSK	Binary Phase Shift Key
CONSERT	Comet Nucleus Sounding Experiment Radio Transmission
DAC	Digital to Analog Converter
DART	Double Asteroid Redirection Test
DDMTD	Digital DMTD
DMTD	Dual Mixer Time Difference
ESA	European Space Agency
FPGA	Field Programmable Gate Array
IF	Intermediate Frequency
IQ	In-phase and Quadrature
LFR	Low-Frequency Radar
MAD	Modified Allan Deviation
OCXO	Oven Controlled Crystal Oscillator
PLL	Phase-Locked Loop
SAR	Synthetic-Aperture Radar
SNR	Signal-to-Noise Ratio

Chapter 1.

Introduction

Small bodies, like comets and asteroids, are remnants of the origin of the Solar System (Gehrels, 1971). Considered to have undergone minimum changes since its formation, they offer a great opportunity to study their evolution and therefore to study the origin and evolution of the Solar System itself (Michel et al., 2016).

Most asteroid studies are done with remote surface sensing from Earth and flyby space missions. These techniques explore the objects' characteristics such as its albedo, gravity, rotation, etc., and then the results are compared with laboratory analogs of meteorites found on Earth (Britt & Consolmagno, 2003) or with theoretical models to infer conclusions. Some missions, like Hayabusa, have even collected samples and brought them back to Earth (Uesugi et al., 2019). However, we are still limited to suppositions and hypotheses for some characteristics that cannot be measured with remote sensing, such as the bodies' internal structure.

The study of the internal structure of asteroids is valuable for several reasons. One of the main interests is understanding the evolution of asteroids and therefore better understanding the origin of the Solar System and of our planet. Other interests concern planetary defense. This field of research is committed to protecting Earth from any hazardous body in its trajectory. Even though the present-day impact rate is lower than during the early stages of our planet, there are records of impacts that had great repercussions on the evolution of life, such as the Chicxulub impact 65 million years ago. This meteorite was partly responsible for the extinction of non-avian dinosaurs (Chapman, 2004). While not dangerous in itself, the more recent explosion of a 20 m asteroid over Chelyabinsk, Russia (Brown et al., 2013), provided a good reminder of the need to detect these objects. Therefore understanding the internal structure is fundamental to develop the technologies necessary to detect and deflect these threats.

Another interest of the internal structure study of asteroids concerns the potential future human exploration of these bodies. Even though the main efforts for human exploration have been focused on Mars, in recent years Near-Earth Objects have also

received some interest as a transitional step before Mars exploration. The greater versatility of human exploration, as opposed to robotic missions, also promises greater scientific payoff (Boden, Hein, & Kawaguchi, 2015).

1.1. Asteroid study missions

The first asteroid studies were done using telescopes in the optical range. This permitted to establish their orbits (Gehrels, 1971). Later, other ground-based methods such as infrared, spectrophotometry, and radar became available, which allowed the possibility to explore other asteroid characteristics, including reflectivity, mass, size, albedo, etc.

There is a rich history of space missions to asteroids in the Solar System. In 1991 the space mission Galileo was launched. Its destination was Jupiter, but on its way there it performed the first asteroid flybys — of 951 Gaspra and 243 Ida, the latter of which was found to have a small moon orbiting it. In addition to Galileo, several other missions encountered asteroids and studied them during their journeys to their principal objectives. Examples of this are: the 1994 mission CLEMENTINE, destined to observe the Moon and repurposed afterward to do a fly-by of the asteroid Geographos, although a malfunction after the Moon phase put end to the mission before reaching the asteroid (Siddiqi, 2002); the 1997 Cassini mission to Saturn, passing 2685 Masursky in 2000; the 1998 mission Deep Space 1, visiting 9969 Braille in 1999 as its first target; Stardust, launched in 1999, which practiced its flyby technique on the asteroid 5535 Annefrank in 2002; and Rosetta, launched in 2004, flying by 2867 Steins in 2008 and 21 Lutetia in 2010 (“Missions to asteroids,” n.d.).

Naturally, there were also missions with the primary objective of studying asteroids. NEAR-Shoemaker (1996) visited 433 Eros in 1998 (Cheng et al., 1997), which gave the first high-resolution photos of an asteroid surface (Veverka et al., 2001). Hayabusa, launched in 2003, arrived at 25143 Itokawa in 2005 and returned samples taken from the asteroid’s surface (Nakamura et al., 2011).

There are also missions ongoing or planned for the near future. Dawn (launched 2007) is a mission to orbit the asteroids 4 Vesta and 1 Ceres (Palmer, Heggy, & Kofman, 2017; Russell et al., 2016). Hayabusa 2 (2014), a mission to 162173 Ryugu is a sample

return mission (Tsuda, Yoshikawa, Saiki, Nakazawa, & Watanabe, 2018; Watanabe et al., 2017), which has already sent landers to the asteroid's surface at the time of this work's writing. OSIRIS-Rex (2016) a sample return mission to visit 101955 Bennu in 2018-2021 (Lauretta et al., 2017). And recently announced, the Psyche mission is planned to launch in 2022 to 16 Psyche, a metal type asteroid to be visited ("Psyche Mission – A Mission to a Metal World," n.d.).

Despite all the missions that have studied asteroids, however, there are none that have studied directly the internal structure of the nucleus of an asteroid.

1.2. Study of the internal structure of small bodies

As a result of the lack of internal studies, for a long time questions about comets' and asteroids' interiors have been posed in different publications (Campo Bagatin, Alemañ, Benavidez, & Richardson, 2018; Housen, n.d.; Richardson, Leinhardt, Melosh, Jr, & Asphaug, n.d.). Studying the internal structure of these bodies will translate into verifying theories and hypotheses about small body formation and Solar System evolution. For example, it is impossible to use classical optical remote sensing on board to be sure to distinguish between a monolithic body or a gravitational aggregate or to determine the body's porosity or grain-size distribution (Herique et al. 2017). Another example is that by now the proposed theory of the formation of binary asteroid systems is based in some inferences of the internal structure (Jacobson & Scheeres, 2011). Therefore the study of internal structure is important to answer this kind of questions.

Two known ways to study the internal structure of small bodies *in-situ* are using seismic waves or radio waves. The former uses mechanical waves that transmit through the body. By studying the scattering and decay of these waves it is possible to deduce information about the internal structure (Walker, Sagebiel, & Huebner, 2006). The latter uses electromagnetic waves of different wavelengths that interact with the body, and, in the same manner as the previous method, by studying the changes produced in the emission we can deduce different properties of the internal structure (Kofman et al. 1998). The electromagnetic technique is the one that we will focus on.

The Rosetta mission was the first mission to attempt to measure the internal structure of the comet 67/P by using the bi-static radar instrument CONSERT. In this

work we will describe a new bi-static low-frequency radar which will also be used to study the internal structure, but this time of an asteroid. This new instrument will inherit from CONSERT parts of its design and operation. Therefore it is of interest to first review in more detail the Rosetta mission and the CONSERT instrument.

1.3. Rosetta mission

After the successful mission GIOTTO to the comet 1P/Halley in 1986 (Reinhard, 1986), the Rosetta mission was a logical next step and it was approved in November 1993. Rosetta was originally intended to launch in 2003 to the comet 46P/Wirtanen, but due to problems with the Ariane rocket, the mission was postponed. It was finally launched in March 2004 with a new objective, the comet 67/P Churyumov-Gerasimenko. The Rosetta mission is named after the basaltic stone that was the principal key to unveiling the mysteries of ancient Egypt, and the Rosetta mission was expected to unveil information about the origin of the building blocks of the Solar System (Glassmeier, Boehnhardt, Koschny, Kührt, & Richter, 2007). The main objectives were: global characterization of the nucleus, chemical, mineralogical, and isotropic compositions of volatiles and refractories, and origin of comets (Taylor, Altobelli, Buratti, & Choukroun, 2017).

The spacecraft used four planetary gravity assist maneuvers to reach the comet, three of them around the Earth and once around Mars. During these gravity assists, the spacecraft flew near two asteroids in the main asteroid belt, 2867 Steins and 21 Lutetia (Glassmeier et al., 2007). After its flyby of Lutetia, the spaceship reached distances of 4.5 times the distance of Earth to the Sun, which was the limit for the solar generator to maintain all systems actives. From June 2011 to January 2014 the spacecraft went into hibernation mode to survive this far distances from the Sun (Ferri et al., 2012). After this period a successful hibernation exit was achieved and the spacecraft had its first rendezvous with the comet 67/P in August 2014 (Glassmeier et al., 2007).

The first mission objective was to do mapping and to choose a landing site for Philae, which was the Landing counterpart of the mission (Biele and Ulamec 2008). On November 12th, 2014, Philae was successfully deployed (Ulamec et al., 2015). Then the mission entered its main phase — observing the comet on its way to perihelion on August 2015 as well as after it.

Philae was expected to use two different systems to keep it on the ground after touch down, a cold gas system intended to push the lander to the surface and two anchoring harpoons, but none of both worked correctly (Biele et al. 2015). Even though the landing of Philae on the comet was not as expected, the instruments returned valuable information on the comet. Among the results coming from this mission are the discovery of molecular hydrogen, nitrogen and oxygen in the coma of 67P, which indicates that they were attached to the nucleus in a low-density and low-temperature environment, like in a pre-solar cloud. Comet 67/P has a bi-lobed shape, and the continuous series of layers of the comet's "body" are independent of the ones of the "head". This indicates that these were two planetesimals formed independently before they merged in a low-velocity collision. The mission gave great insight into the formation of the comets in the Solar system, but also opened new questions that remain without an answer for now (Barucci & Fulchignoni, 2017).

The Rosetta mission contained among its instruments a bi-static radar named CONSERT, Comet Nucleus Sounding Experiment by Radiowave Transmission. This instrument had the objective of studying the internal structure of the comet 67/P. By transmitting radio waves through the asteroid, CONSERT was able to measure specific characteristics of the comet. We will describe CONSERT in detail next, but first, it is of interest to review how we can study the internal structure of a body using radio waves (Kofman et al. 1998, 2007).

Figure 1. OSIRIS wide-angle camera image taken on 20 September 2016, when Rosetta was 13.7 km from the center of Comet 67P/Churyumov–Gerasimenko. The scale is 1.28 m/pixel and the image measures about 2.6 km across. Credit: ESA/Rosetta/MPS for OSIRIS Team MPS/UPD/LAM/IAA/SSO/INTA/UPM/ DASP/IDA

Chapter 2.

Small bodies radar tomography by bi-static radar

Radar was invented in 1930 with the purpose of detecting approaching aircraft. Since then, radar has been the subject of many improvements and diversification of its applications. Radar uses the time of travel of an electromagnetic wave and its modification between a transmitter and a receiver to infer different characteristics of the target or the propagation medium. Radar is a technology long used in diverse fields, i.e. ground penetrating radar (Davis & Annan, 1989), aeronautics and air-traffic control, exploration of planets like Venus whose surface cannot be optically imaged, meteorology, imaging SAR, archeology, etc. (Skolnik, 2008). Therefore radar is a mature tool with great utility for planetary missions, and in particular for asteroid surface, sub-surface and internal structure study. The near subsurface and internal structure of asteroids are almost unknown and this technology can help characterize the body from a partial to a global scale.

Radio waves interact with the medium they are propagating through and will undergo different modifications depending on the properties of the material. Therefore, radar is the ideal method to study the internal structure of an asteroid. Radio wave penetration through a material — in this case, the asteroid's nucleus — is approximately related to the wavelength (λ), but also it depends on the size of the heterogeneities in the medium. A wave will propagate coherently where heterogeneities are smaller than λ, and will also propagate coherently in a medium whose size is larger than λ. This means the radio wave will be scattered or lose coherence if it finds heterogeneities the size of λ. It will also be refracted at any interface. Frequency varies approximately inversely to penetration depth for high-loss materials, and bandwidth determines the range resolution and will be mainly limited by technical constraints (Kofman et al. 1998; Heggy et al. 2012; Herique et al. 2017; Davis and Annan 1989).

The wave's properties such as its velocity will also be affected by its travel through the nucleus. This is determined by the dielectric properties of the asteroid. The dielectric permittivity ε_r is a complex number: the real part ε_r' relates the wave velocity

through the material and the imaginary part ε_r'' is associated with the absorption. Which holds for $\varepsilon_r' \gg \varepsilon_r''$.

There are different types of radar, mono-static, bi-static, multi-static which refers to the number of electronics involved in the transmission and reception of the signal. In this work, we will focus on the bi-static radar in transmission, which is a radar with two separate electronics Figure 2.

To summarise, radio is a technology capable of studying the internal structure of a small body and can reveal different characteristics of the nucleus depending on the interaction of the radio wave with the materials and structure of the body.

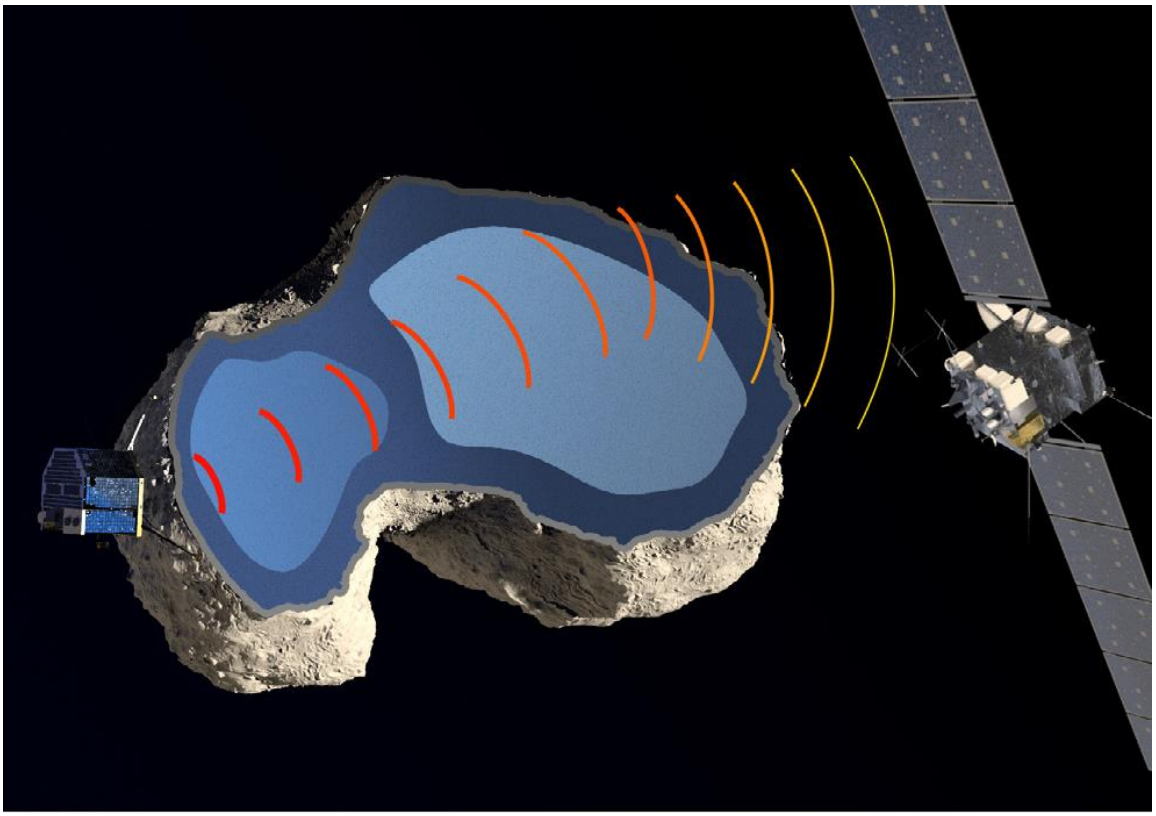

Figure 2. Bi-static radar configuration. Artist's view from CONSERT/Rosetta credit: CGI/Rémy Rogez; shape model: Mattias Malmer CC BY SA 3.0, Image source: SA/Rosetta/NAVCAM, ESA/Rosetta/OSIRIS/MPS/UPD/LAM/IAA/SSO/INTA/UPM/DASP/IDA)

2.1. CONSERT

2.1.1. Instrument description

CONSERT was the only instrument aboard the Rosetta spacecraft capable of studying the internal structure of the comet. It was a bi-static radar composed of two electronics: one onboard the Rosetta spacecraft orbiting the body (the Orbiter) and the other onboard Philae, a lander system that was placed on the comet surface (the Lander). These two electronics transmitted electromagnetic waves between them. This transmission was done for different positions of the Orbiter around the comet, which means that for some transmissions the signal went through the comet Figure 3.

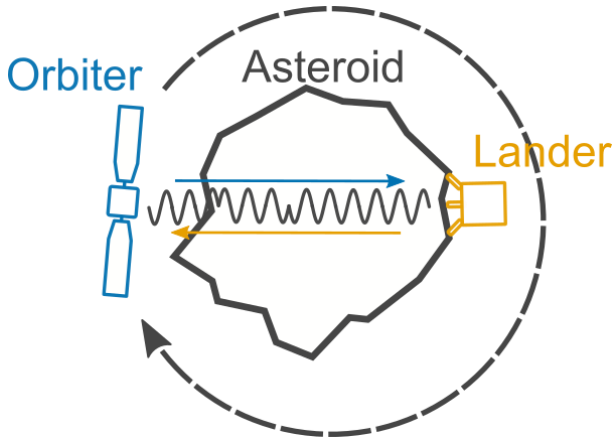

Figure 3. Bi-static radar operation. Graphical depiction of the signal traveling through the asteroid.

The radio wave frequency of 90 MHz was chosen with a-priori information of the body's composition, to be able to travel through the nucleus and be received by the other electronic. The propagation delay of the signal was measured accurately. This propagation delay was a function of the Orbiter's and Lander's relative positions but also of the reflections and refractions of the signal inside the nucleus of the comet. The idea was to have several cuts for different orbits and obtain a tomographic image of the internal structure (Kofman et al. 1998).

2.1.2. Scientific objectives of CONSERT

The instrument's main objective was to deduce the comet's dielectric properties by measuring the propagation delay of the radio wave through the nucleus (Kofman et

al. 2007). This is linked directly to the mineralogy and the porosity of the comet material. This information is crucial to understanding the formation and structure of the nucleus. (Kofman et al. 1998). Through measuring propagation delay, attenuation and scattering of the radio wave it is possible to characterize heterogeneities like voids and boulders and to discriminate between monolithic or aggregate structure. The dielectric permittivity is directly related to the constitution of the materials that compose the comet and to the distribution of its components; the propagation delay directly relates to the estimation of the average permittivity along the path of transmission; and the scattering of the signal is related to the internal structure, as the size of the components will attenuate and scatter the signal.

The path loss of the radio wave through the comet offers information about the mean absorption of the body, which is related to the materials that compose the body. The number of different paths and their variations against the propagation path is directly related to the internal structure, allowing us to map interfaces via reflections. The results are then compared with theoretical models and laboratory models of asteroids (Heggy et al., 2012).

2.1.3. CONSERT functioning principle

The instrument design was constrained by planetary mission conditions, such as mass, size, and power, and weather conditions such as operational temperature, and radiation and vibration intensity. It was also constrained by the body selected for the study. CONSERT required that the signal in the Lander and in the Orbiter had good SNR at reception and was coherent during the experiment to permit global processing of the signal for different Orbiter positions.

In a trade-off between technical constraints, signal penetration and spatial resolution, the carrier frequency chosen was 90 MHz, with a bandwidth of 10MHz, and a sampling frequency of 10MHz in IQ configuration. This translates to a resolution of 20 m in the comet nucleus. The bandwidth chosen shows that the noise is mainly dominated by the galactic noise, over the electronic noise of the antenna and electronics. The galactic noise is shown in Figure 4.

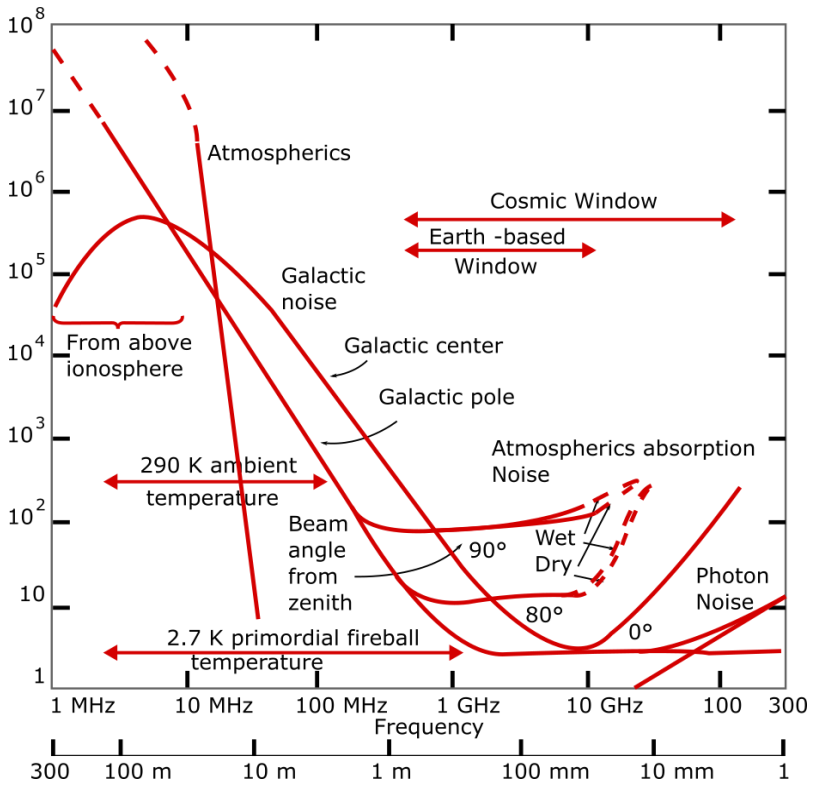

Figure 4. Galactic noise Antenna sky temperature as a function of the frequency and zenith angle re-edit from (Kraus, 1986).

Bi-static radar means two separate electronics. There are two clocks, one on each electronic. Even though the clocks have the same frequency nominally, in reality, there is an offset from the expected frequency. This difference will produce a drift in phase between the two clocks, and also drift in the calendars. This clock drift, combined with the planetary constraints for the instrument design, limits the type of clocks that can whose, and also imposes design and operation constraints for the instrument.

The bi-static radar can work in a one-way mode, meaning that one electronic do the transmission and the other receives it, and after, by knowing the absolute values of time for both electronics we can measure the propagation delay. In a one-way operation of the radar, the accuracy needed from the clocks was of 100 ns during the whole Orbit (8h), meaning that the clock stability should be of $\Delta f/f \approx 10^{-12}$ — which was not achievable with clocks under the planetary mission constraints given to CONSERT. To reduce this requirement in frequency stability, CONSERT used a transponder concept, which reduces the stability needs to $\Delta f/f \approx 10^{-7}$, by using a two-way propagation. This two-way transmission is what in radar domain is known as a Sounding. We call it a Ping-

Pong transmission, where the first transmission (Ping) is a synchronization signal and the transmission back (Pong) is the science signal.

The use of the transponder concept reduces the frequency stability requirement but it splits it into different time scales. We will develop the time analysis in the next chapter, nevertheless, we can note that as there is presence of different time scales the errors at each scale have different impacts, but these errors will be correlated. This impacts will be reflected in errors in the phase of the signal received as well in the propagation delay measured by the system. The time scales of interest for the Transponder concept are the Coherent Accumulation which is the accumulation of several transmitted codes, the time from reception and transmission on the Lander, and time synchronization of the transmission and reception windows between electronics to allow communication. As said before, during the next chapter each time scale will be presented in detail as well as the errors at each one.

2.1.4. In-Time Transponder Concept

The in time-transponder concept implemented in CONSERT, as previously mentioned, consists of two identical electronics, one electronic placed on the body's surface and another one orbiting the body (called the Asteroid in this section for general description purposes), shown in Figure 5. The Lander is an active "delayed reflector". This means that the signal transmitted by the Orbiter is received by the Lander and re-transmitted back later with a known delay (Barbin et al., 1999). With this operation, the signal is measured in the time reference of the Orbiter, relaxing the constraint of clock stability (Kofman et al. 2007).

The measurement sequence is as follows: First, the Orbiter transmits a coded signal through the Asteroid to the Lander (Figure 6). The Lander receives this signal and pulse-compresses it to find the propagation delay. Then the Lander sends back the same coded signal but synchronized to the peak detected. The Orbiter samples the signal and stores it for transmission to Earth. If we pulse-compress the signal received by the Orbiter, the propagation delay measured on the Orbiter signal corresponds to twice the propagation delay of the signal through the Asteroid — but the reflections and second paths have the distance of only one travel through the asteroid to the main peak.

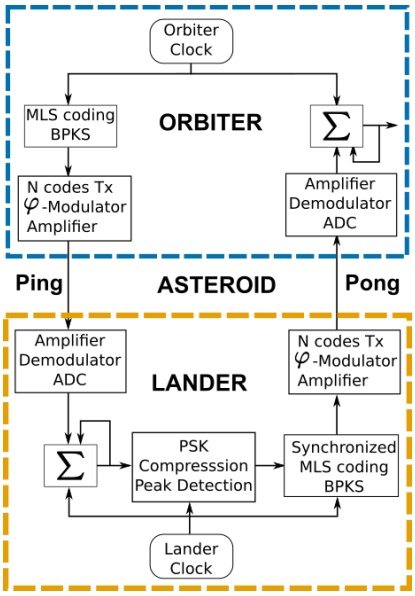

Figure 5. Transponder concept block diagram. Both electronics have an accumulation of codes at reception. The only difference between both is the peak compression and detection present in Lander.

As the signal travels through the Asteroid, the SNR is very low at reception. Therefore the signal transmitted is a Binary Phase Shift Key (BPSK) code. Several codes are transmitted continuously, making the transmission periodical, and at reception, these codes are accumulated to improve the SNR.

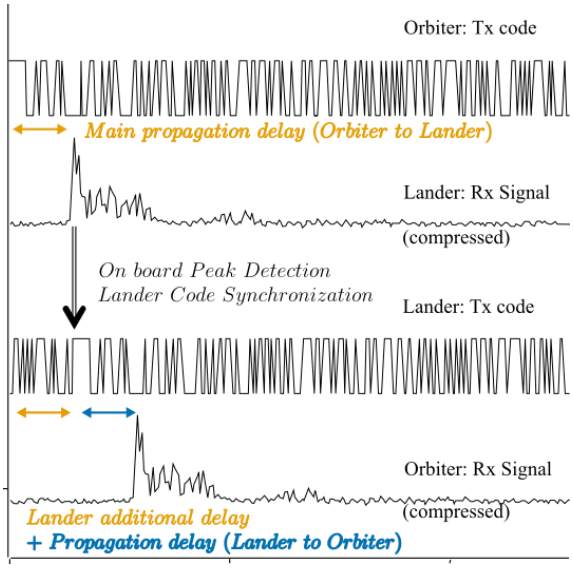

Figure 6. In-time transponder sequence. Notice the propagation delay measured in Orbiter is twice the real propagation time.

2.1.5. CONSERT operation

The operation of CONSERT starts with a warm-up phase. This phase permits the clocks to reach the frequency stability needed. After this, to guarantee the frequency stability is lower than the 10^{-7} constraint, a frequency calibration is performed. During the direct line of sight between both electronics, the Lander transmits a pure sinusoid wave to the Orbiter. The Orbiter uses this pure frequency to lock a PLL and correct its own frequency. This tuning phase is also used for the time synchronization of the calendars with a 10 ms accuracy (Barbin et al., 1999). It is important to note that this process needs high SNR to be performed correctly. The electronics then wait until its time to start with the science transmissions at the occultation of the Orbiter by the Asteroid and begin the science transmissions. A Sounding is performed approximately every 2.5 seconds (Rogez et al., 2016), and for a complete Orbiter orbit, this results in a Scan of the Asteroid. Table 1 shows the principal parameters of the instrument.

Table 1 Main Parameters of the Philae Lander and Rosetta Orbiter Instrument (Herique et al. 2015)

Mass	3 kg on orbiter, 2.3 kg on Philae
Average Power	3 W on orbiter and Philae
Clocks	10 MHz SOREP (see detail later)
Nominal operation	$\Delta f/f < 2 \times 10^{-7}$
Degraded mode if offset	$2 \times 10^{-7} < \Delta f/f < 4 \times 10^{-7}$
Transmission	90 MHz carrier, BPSK modulation
Pseudo noise code	$255 \times 100\ ns = 25.5\ \mu s$
Code repetition	Up to 200 ms
Rf power	2W/Orbiter, 0.2 W/Lander
Receiver	Band 86-94 MHz (-3 dB), linear phase
Gain range	30-90 dB with AGC
Demodulation	I and Q “synchronous” detection
ADC	8 bits 10 MHz ADC on each channel
Processing	
Real time coherent integration	1024 code periods (26 ms, +30 dB on SNR) 256 periods (+24 dB on SNR), in degraded mode
On-board the Lander	Code compression (+24 dB on SNR) and peak detection
Telemetry (data rate)	Orbiter: 8 kbits/measurement point 65Mbits/Orbit Lander: 20 Mbits/Orbit (depending on how often the complete set of data will be transmitted).

After the science acquisition (after occultation) and during the direct line of sight, the code transmission is repeated and these transmissions are used as a calibration of the lander delay with comparable weather conditions, i.e. the ones in the science transmissions (Figure 7). It is important to note that after the tuning phase and until the end of the Scan, both electronics work autonomously and separately. Meaning that each clock in each electronic is responsible for the schedule of the operation.

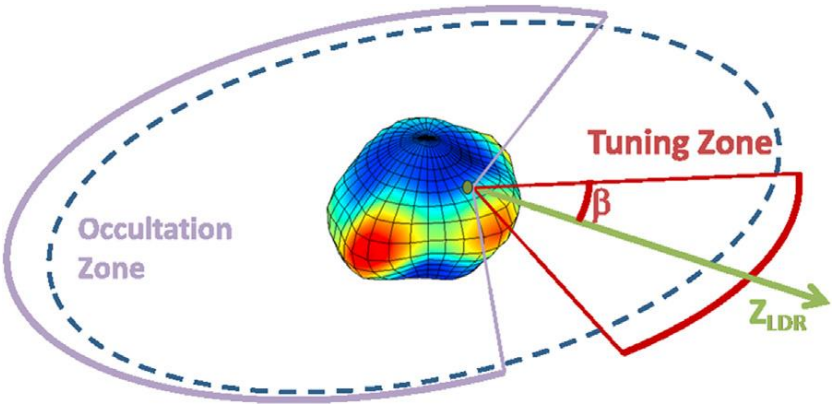

Figure 7. CONSERT science sequence. Rosetta orbit is shown by the blue dashes. Lander Z-axis (Z_{LDR}) vector shows the lander 'up' axis and position. Warm-up and tuning occur when Rosetta and Philae are in visibility, in the tuning zone (red), science sounding in the occultation zone (purple). Calibration takes place just after exiting the occultation zone. (Rogez et al., 2016)

2.1.6. CONSERT signal

The CONSERT coded signal is a Maximal-Length Sequence code. This type of code has a similar structure to a random sequence, and therefore the autocorrelation function is desirable. These codes are also called pseudorandom noise. For CONSERT the code was composed of 255 symbols. The receiver accumulates 1024 codes to improve the SNR. The improvement coming from the accumulation is that the signal obtains a gain of a factor of N while the noise just increases by a factor of $\sqrt{N}$.

The received signal for both Lander and Orbiter is first filtered by analog electronics, i.e. the antenna and filters, then it is demodulated and sampled at 10 MHz in IQ configuration. The IQ demodulation mixes a local oscillator signal with the signal to take it to baseband, but it mixes the signal with two signals phase sifted 90° generating two different channels, the In-Phase and Quadrature channels. After it is pulse-compressed to find the propagation delay (Figure 8). This sampling period gives the accuracy limit of the time measurement (+/-50ns).

The time analysis performed for this instrument shows the presence of a sampling error that will introduce a time error in the propagation delay measured on the Lander and Orbiter (Pasquero, Hérique, & Kofman, 2017). The sampling error is a jitter uniformly distributed in one sampling step, after several Soundings. This error will be fully explained and illustrated in the section "Time Model in-time transponder".

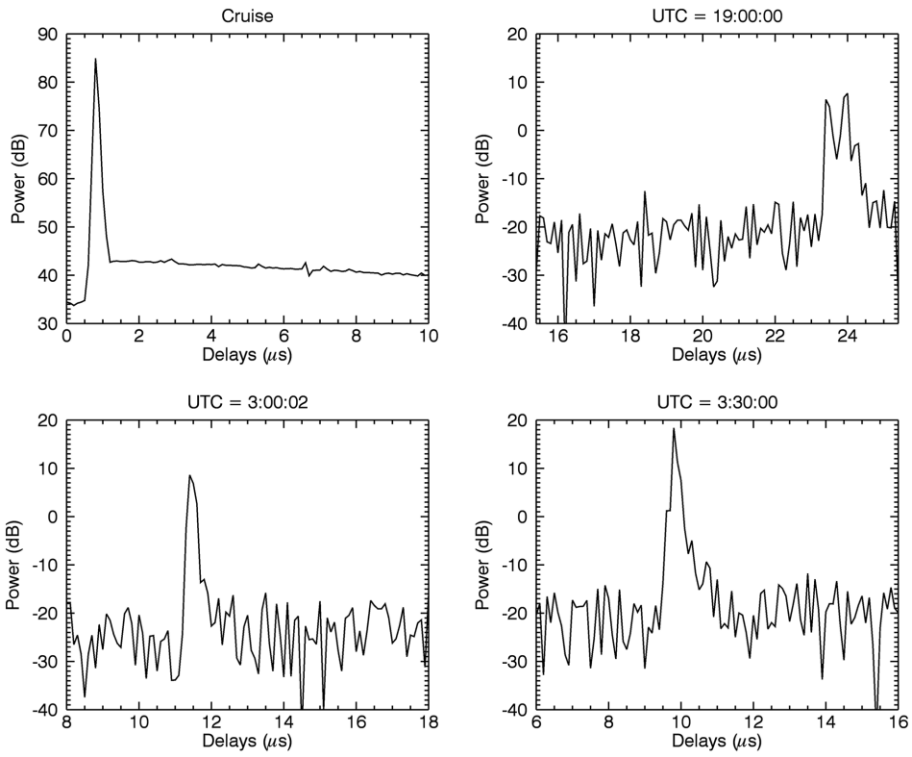

Figure 8. CONSERT signals as a function of time delay. Signals that have propagated through the nucleus, as measured at the output of the matched filter, are presented for different measurement times and compared to the calibration signal during the cruise phase (Wlodek Kofman et al., 2015).

To increase the accuracy of the propagation delay measurement, (Pasquero et al., 2017) propose methods to increase it to over 1/20 of the sampling period limit. The classical compression method uses a reference signal equal to the transmitted, containing the same N points, and therefore there are N time-shifted reference signals to perform the compression. This method limits the resolution to the time resolution between the points. To increase it, it is possible to model the signal and generate a reference signal with more than N points. For this, it is necessary to model signals with a smaller step than the sampling of the signal, and it is needed to take into account the aliasing of the signal in the frequency domain because this is the main limit for this method. In CONSERT aliasing was one of the main limitations, because of the sampling frequency in our new proposed radar we expect this problem is reduced as the sampling frequency has increased.

The data returned from the CONSERT experiment consists of the 255 complex samples of the signal propagated from Lander to Orbiter and 21 samples of the

correlation function around the maximum value measured in the Lander, and every 25 Soundings a complete signal of the Lander is transmitted. This limited transmission of Lander data is due to limitations in the data budget available in the mission.

2.1.7. CONSERT results

Several articles have been published showing the results obtained by the Rosetta mission's study of the internal structure, and how the data from CONSERT helped other objectives such as the localization of Philae (Kofman et al. 2015; Herique et al. 2015; Herique et al. 2016; Ciarletti et al. 2017).

CONSERTs data shows from the measurement of the propagation delay and the form of the signal, that there was no scattering observed down to -20 dB it is possible to conclude that the measured part of the comet is very homogeneous for a scale of 10's of meters. However, the well-defined two or three paths on the propagation delay could signal the presence of larger structures (Kofman et al. 2015).

Another very important mission contribution from CONSERT was helping to reduce the landing site window to an area of about 21 by 100 square meters. This result was achieved by using the ability of CONSERT to measure the relative distance between Rosetta and Philae and also by using simulations using different values for the dielectric properties of the comet (Herique et al. 2015).

The analysis of the signal propagated through the comet permitted to deduce the average of the real permittivity 1.27 ± 0.05. By using dielectric properties of mixtures of ices, refractories, and porosity, this result suggests that the porosity is of 75%-80% and the dust-to-ice ratio is between 0.4 and 2.6 and that the dust permittivity is lower than 2.9 (Herique et al. 2016).

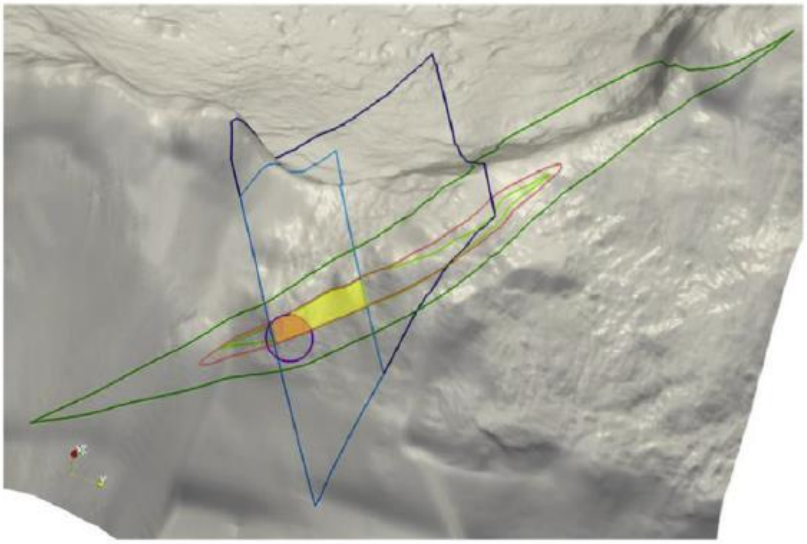

Figure 9. Search Campaign 4 - Lander localization from CONSERT data: Projected location of Philae on the surface of 67 P. Light green polygon: line of sight measurements min/max±1 sigma. Dark green polygon: min/max distance±3 sigma. Light blue: propagation through the comet at a maximum of 325m and±3 sigma. Dark blue: propagation through the comet at a maximum of 1000m and±3 sigma. Red ellipse: zone with RMS error below 1.0. Purple circle: from joint inversion of permittivity and position. Yellow zone: taking into account all measurements (22.5×106.5m2) Orange zone. The most likely estimate (22.5×41.5m2). Credits: ELLIPSE: ESA/ROSETTA/PHILAE/CONSERT; SHAPE MODEL: ESA/ROSETTA/MPS FOR SIRIS TEAM MPS/UPD/LAM/IAA/SSO/INTA/UPM/DASP/IDA (O'Rourke et al., 2019).

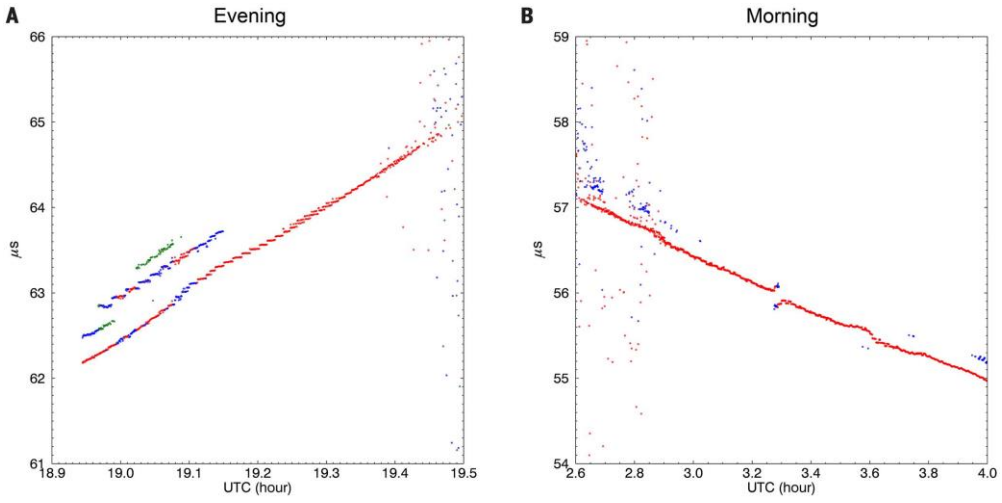

Figure 10. Measured propagation time between Philae and Rosetta as a function of observation time. Evening (A) and morning (B) measurements. Red corresponds to the strongest signal, blue to the second strongest, and green to the third strongest. Second and third are in the interval of 6 dB below the red one. The dispersed dots correspond to delays not correctly detected due to the noise (Kofman et al. 2015).

2.1.8. Possible enhancement

From the data analysis from CONSERT is possible to recognize different effects over the signal received in the Orbiter. One of the most interesting effects is a phase rotation. This effect is well defined in the on-ground calibration data of CONSERT. We will talk in more detail about these effects during the Simulator section where we will compare the data from the calibration of CONSERT against the results obtained by the simulator of the transponder.

The main problems presented in the transponder concept are the time errors in the phase of the signal received and in the propagation delay measured. These errors are a consequence of not only one reason, but several with different origins. Among this we can find, the errors generated by the system, the SNR from the noise in the environment and electronics and the one that we will focus on during this work: the clock drift between both electronics.

As long as there is a clock frequency difference between both electronics, a phase deviation in the signal will be presented in the received signal onboard the Orbiter. Also, this phase error can be unfolded as a time accumulation error.

The main improvements that we directly obtain by doing a time analysis of the Transponder Concept are the possibility of having an absolute phase reference of the signal for the whole mission, which translates into a science return improvement by permitting full coherent analysis of the data. Another improvement is the possibility of onboard corrections from real-time knowledge of the frequency drift between clocks.

The difference between the Low-Frequency Radar (LFR) and CONSERT will consist in: the direct measurement of clock drift between clocks; the use of temperature and housekeeping data to improve the estimation; the proposal of compensation techniques for the science data; and the improvement of calibration which, as mentioned before in CONSERT, was a weak point of the design by expecting high SNR for the lock of the PLL.

Also, the characterization of the clocks will help in the improvement of all the operation design, which will translate into electronic design improvement and

optimization of the operation times, giving possibility to increase science times and reduce power consumption.

2.2. Low-Frequency Radar (LFR)

As stated before, frequency plays an important part in the type of information we can obtain and drives the type of instrument to be designed. To cover different resolutions for different body properties, our group works in parallel in two different instruments: a High-Frequency Radar (HFR) for regolith studies and subsurface, and a Low-Frequency Radar (LFR) for global characterization of the interior. Both of them correspond to different approaches to the radar technique. The former is a monostatic radar, which means that the transmitter and receiver are located in the same place, and the latter is a bi-static radar which means its transmitter and receiver are located in different places.

In this work, we will focus on the bi-static radar, in the same configuration as CONSERT onboard Rosetta. This instrument needs two separate electronics. One is placed on the surface of the asteroid and the other orbits around it. This radar will transmit through the asteroid a signal from one electronic to the other. The radio-wave will change speed and will be attenuated and scattered during its travel through the asteroid due to changes in the asteroid's composition and internal structure. By measuring these effects, it is possible to deduce some of the asteroid's characteristics, like the dielectric property. This technique is limited to small bodies on the order of 1 km because the signal cannot reach the other side with sufficient power to be detected and also the selected frequency has its own limits to travel through the body. This also means that for selecting the frequency of the instrument, prior knowledge of the objective body is needed to propose correct instrument design.

2.2.1. AIDA mission

We will consider the proposed scenario for the AIDA/AIM mission. Even though this mission was not funded by the ESA Member States, our instrument could be readjusted for any other body for a future mission. In this work, we will present instrument development under the stated scenario, up to phase A/B1 of the AIDA/AIM mission by ESA (Herique et al. 2018).

The Asteroid Impact Mission (AIM) is the ESA part of the mission while the Double Asteroid Redirection Test (DART) is the counterpart developed by NASA. The conjoint mission is named Asteroid Impact & Deflection Assessment (AIDA). AIDA mission will be the first mission to use a kinetic impactor to deflect an asteroid's path. The mission was intended to visit the Didymos binary system and deflect the moonlet (Michel et al., 2016).

The main scientific objectives of AIM as a standalone mission were to characterize the mass, size, detailed morphology, and density of the moonlet; determine the dynamical properties of the system; and determine the surface and sub-surface properties, internal structure and the thermophysical properties of the moonlet. It was also meant to test the technology in deep space as part of a low-cost mission. The main tests included autonomous navigation, optical communication, close proximity operations, micro-lander and deep-space inter-satellite communications (Michel et al., 2016).

The AIM mission was to be composed of several elements. The spacecraft would arrive at the Didymos system and deploy different components. One component would be the Lander MASCOT 2, based on the MASCOT 1, the lander on board of the HAYABUSA 1 mission. This Lander would deploy different instruments on the surface of Didymoon. AIM would also release 2 U3 CubeSats COPINS that would create a constellation around the moonlet. This group of separate elements would allow for the demonstration of deep-space inter-satellite communications. These CubeSats could also be used for potential measurements that pose a high risk for the main spacecraft (Michel et al., 2016).

The Didymos system is binary, which means there are two bodies orbiting each other. A binary system offers the possibility of studying two bodies, while both are in the field of view of the instruments. In this case, the main one (Didymain) is bigger than the secondary (Didymoon). Didymain has a roughly spherical shape with an estimated diameter of 775 m, and Didymoon has a diameter of 163 m. The distance between their centers is considered to be 1050 m. The system orbit and both equators are in the same plane.

A binary system study with a landing payload also imposes an *a-priori* study of temperature at the surface. If the moonlet's rotation is synchronous with its orbit around the primary and the poles of their orbits are parallel to the heliocentric orbit, there will be eclipses in the hemisphere facing the primary, inducing temperature changes in the surface.

A binary system may contain dust and boulders between the two main bodies, even though the Didymos system is expected to have passed this developmental stage and is thus not expected to have any of this material. Considering the rotational speeds, however, could give insight into the possibility of flying dust, in order to anticipate protection of the cameras and instruments.

2.2.2. LFR instrument description

LFR inherits the function design from CONSERT. The improvements in terms of design include the use of an FPGA board for the digital processing of the data. This adds versatility to the design, as a large part of the system is now in digital form.

The instrument is designed to resolve a 5% variation in the mean porosity along the propagation path of 160m, and a resolution better than 15 m on the optical length is required. This means a resolution of 50ns (bandwidth = 20MHz). The trade-off between dielectric losses of 20 dB for an S type asteroid, the galactic noise in this bandwidth and 40 dBm of transmission power yield that the carrier frequency should be 60MHz. With these specifications, the Signal-to-Noise Ratio is of 60 dB after processing.

The signal, as in CONSERT, is transmitted between both electronics. This signal is a BPSK code (Binary Phase Shift Key). The code is composed of 255 symbols. The code, as described previously, is accumulated 1024(2048) times to improve the SNR. The number of accumulations is limited by clock drift and link budget (orbiter to lander relative position). Table 2 shows the principal parameters of the LFR instrument.

Table 2. LFR specifications for Orbiter and Lander electronics for AIM mission.

Characteristic	Orbiter	Lander
Frequency (carrier)	60 MHz	
Bandwidth	20 MHz / 30 MHz	
Signal Modulation	BPSK	
Resolution	10-15 m	
Polarization	Circular	Linear
Tx power	12 W	
Pulse repetition	5 seconds	
Sensitivity	Dynamic = 180 dB	
Mass	1390 g	1250 g
Power max / mean	50 W / 10 W	
Typical Data	1 Gbit	0.3 Gbit

2.2.3. Scientific objectives

The instrument has three primary objectives:

- Measure the internal structure of the smaller body of the system, Didymoon. This will allow us to characterize the structural homogeneity of the body.
- Derive an estimate of the average complex dielectric permittivity of Didymoon, which relates to the porosity and mineralogy of the material.
- Determine the 3D internal structure of Didymoon.

The instrument can also be used for secondary objectives to help accomplish other measurements: ranging measurements, which will help contribute to the study of the dynamical state of the system and determination of its mass; measuring the distance between Orbiter and Lander during descent and after, and post-DART characterization of the moon.

2.2.4. LFR Antennas

The Lander antenna is deployed after reaching the final destination. This antenna has a V shape that provides linear polarization with high efficiency for the transmission through the body. This tubular boom antenna system was developed by the enterprise Astronika, and it is able to deploy 1.4 m antennas consuming approximately 2 W. The

Lander has a secondary antenna set, which is deployed just after separation this antennas will allow operation during the descent and will be useful later for secondary objectives and also for direct line of sight operation Figure 11.

The antenna in the Orbiter is composed of 4 booms in the spacecraft corners, this array provides a circular polarization. Each of these booms will be of 1.5 m and are phase-shifted 90° to each neighbor.

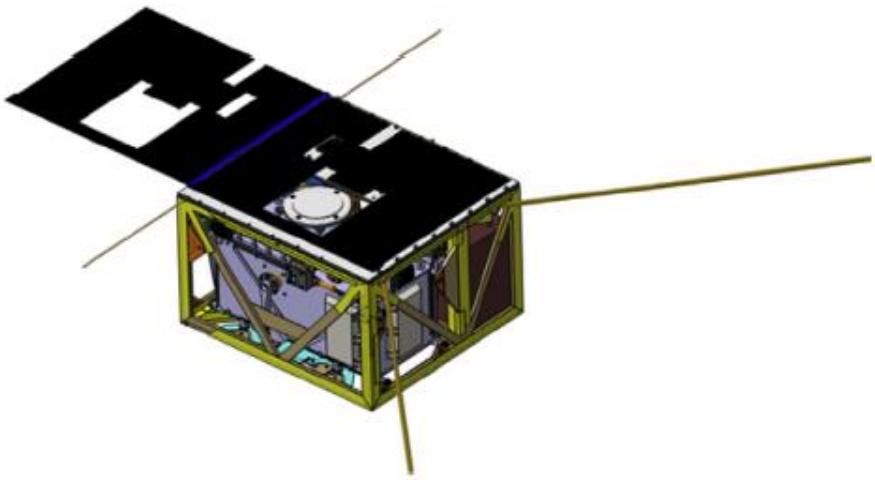

Figure 11. Lander antennas: V-shaped dipole and secondary dipole antenna. MASCOT2 accommodation (Alain Herique et al., 2019).

2.2.5. LFR Electronic box

Both systems, Orbiter and Lander, are electronically equivalent. They are equipped with a matching network, the Reception and Transmission switch, DAC and ADC depending on the transmission or reception path, FPGA, microcontroller and an OCXO. Both electronics work as automats sending and receiving a BPSK code modulated at 60 MHz (See Figure 5).

The reception path receives the signal through the antenna. The signal is filtered and adjusted in amplitude with amplifiers and attenuators. Then the signal is mixed with an 80 MHz signal. This mixing takes the carrier frequency of 60MHz to an intermediate frequency (IF) of 20 MHz. The signal is filtered to remove aliasing and then is sampled by an ADC at 120 MHz. This sampling frequency will give 6 points per symbol for a

signal of 20 MHz bandwidth, which will increase the accuracy of the measurement (see Table 3).

In the transmission path, the signal is generated in the FPGA. It is then amplified in a two-stage amplifier and sent to the antenna for transmission.

Table 3. Frequency plan for sampling frequency @100 MHz (From LFR Instrument document)

			Negative							Positive					
			FI image 1		**Main**		FI			FI		**Main**		FI image 1	
Radar Signal	60	MHz			-70	-50						50	70		
LO	80	MHz	-150	-130			-30	-10		10	30			130	150
sampling	100	MHz	-250	-230	-170	-150	-130	-110		-90	-70	-50	-30	30	50
			-350	-330	-270	-250	-230	-210		-190	-170	-150	-130	-70	-50
			-50	-30	30	50	70	90		110	130	150	170	230	250
			50	70	130	150	170	190		210	230	250	270	330	350

Frequency plan for sampling frequency @ 120 MHz (From LFR Instrument document)

			Negative							Positive					
			FI image 1		**Main**		FI			FI		**Main**		FI image 1	
Radar Signal	60	MHz			-70	-50						50	70		
LO	80	MHz	-150	-130			-30	-10		10	30			130	150
sampling	120	MHz	-270	-250	-190	-170	-150	-130		-110	-90	-70	-50	10	30
			-390	-370	-310	-290	-270	-250		-230	-210	-190	-170	-110	-90
			-30	-10	50	70	90	110		130	150	170	190	250	270
			90	110	170	190	210	230		250	270	290	310	370	390

The E-box (Figure 12) is designed to be compatible with the MASCOT2 lander. MASCOT2 is a variant of the lander platform MASCOT designed to fly in HAYABUSA2 mission to the asteroid (162173) Ryugu (Ho et al., 2017).

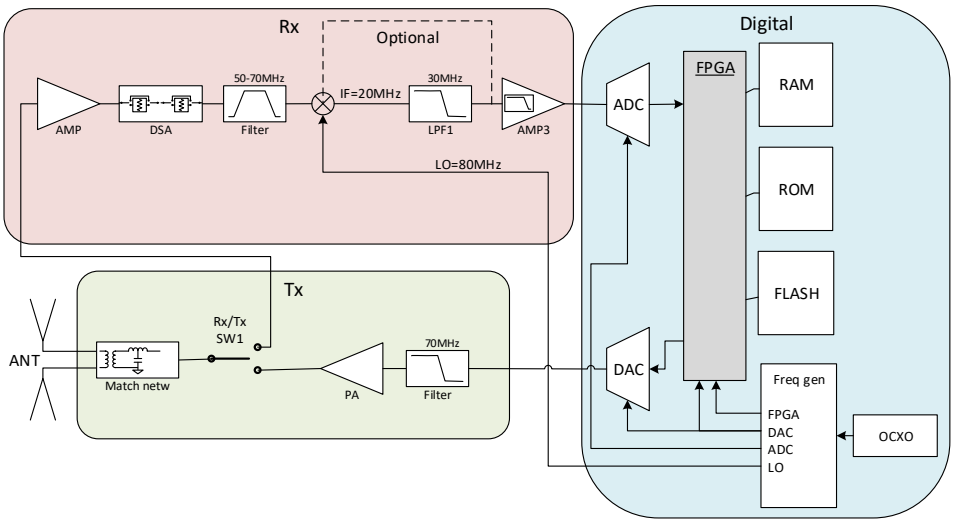

Figure 12. Block schematic of the LFR system architecture showing electronic box including a transmitter (Tx), Receiver (Rx) and digital module (Herique et al. 2018).

LFR Digital Board

The digital processing is performed between an FPGA and a microcontroller. After the received signal is transformed to IF, the signal is sampled by the ADC with 12 bits at 120 MHz. The FPGA is in charge of the coherent accumulation; this process increases the SNR and after accumulation, the size of data is framed to 16 bits. Then the signal is IQ-demodulated digitally. After this, in the Lander, there are two more tasks in the reception path. The signal is passed to the microcontroller to perform the pulse compression and peak detection, which are duties more adequate for a sequential component. In this case the accuracy of the peak detection, ideally, is limited by the sampling step. In contrast, the Orbiter only does the accumulation and store the values for transmission to Earth.

At transmission level in the Lander, the FPGA generates the coded signal and synchronizes it to the delay detected in the pulse compression. The signal generation of the DAC is a pure binary signal.

The frequency of the sampling was selected in a trade-off between aliasing and synchronization. The chosen sampling frequency of 120 MHz has the risk of aliasing, as shown in Table 3 in the red cells with the image of the intermediate frequency after being sampled with no filtering, but it was preferred over the 100 MHz. This decision was made because the reception frequency and the transmission frequency are generated from the same 10 MHz master clock. This means that reception and transmission frequencies will not be synchronized for all times and will introduce a time error in the phase of the signal. This could be solved but requires to introduce a new delay in the transmission back to the Orbiter. We will cover this synchronization error in the time analysis chapter.

All digital electronics will be driven by a 10 MHz ultra-stable clock. From this 10 MHz signal and the use of PLL all the needed frequencies will be generated.

2.2.6. LFR Operation

The operation of the LFR starts in direct sight of the Orbiter and the Lander and continues during the occultation of the Orbiter by the asteroid. All this time the LFR onboard the Orbiter and Lander work autonomously; this means that the clock on board each instrument supplies the timing for the FPGA and electronics to perform the

acquisition and transmission and provides the carrier signal to be transmitted. This automats work independently and depend only on the stability of the clocks for the correct timing.

Operation modes

There are 3 operation modes designed for LFR based in CONSERT: Sounding, Ranging and Stroboscopic. There is also a calibration mode used for frequency calibration and/or time synchronization. This calibration mode depends on the characterization of the clocks, meaning that the operation could be used once during the mission, or once for each Scan, depending on the accuracy of the clocks used.

Sounding mode: The principal mode to characterize Didymoon, it consists of transmission from Orbiter to Lander and back. This two-way propagation needs to be synchronized for the duration of the occultation of the Orbiter by the asteroid.

Ranging mode: This mode is similar to Sounding but is used, principally, during the descent of the Lander to the asteroid, and permits us to measure the distance between both electronics.

Stroboscopic mode: The pulse frequency repetition (PFR) of both electronics is slightly different, creating a stroboscopic effect that will permit some Soundings to be synchronized every number of Soundings. This eliminates the need for synchronization before starting the Sounding, but it loses some Soundings for science return. This mode was used in CONSERT to help find the localization of Philae after the bouncing in the landing.

Monostatic mode: This mode employs the radar as a monostatic system retrieving the signal that comes back to the Orbiter. Used in CONSERT but not planned to be used for LFR.

2.3. General Approach of the thesis

As we have said before, radar is a technology with the maturity and the functionality to do internal structure studies in an asteroid. Therefore we propose a bi-static radar at low-frequency to explore the interior of these bodies. The time analysis of the radar can deliver useful information to improve the science return and possibly relax

design and operational constraints. This time analysis will break the transponder concept presented above and will present different time scales of interest. These timescales are the Coherent Accumulation, Reception to Transmission in the Lander, Sounding to Sounding and the Transmission and Reception windows between both electronics. For this, it is needed a good understanding of the clock generation signals to understand the way the time errors will affect the measurement. The time analysis of the instrument and its simulation will help to understand the error correlations at different time scales. Also, it will render useful to propose clock drift estimations as well as compensation methods for the clock drift error coming from different causes like temperature and aging. Figure 13 is a block diagram that will help follow the course of the research.

First, we will analyze the clock generation and how to model it (**Clock Model**). After, a time model of the transponder concept will be developed (**LFR Time Model**). **LFR Time Model** will be used with the **Clock Model** to develop a simulator to generate **Synthetic Data** of the transponder concept that will give a first insight of the effects of clock drift in the propagation delay measurement (dark green-dotted lines, Synthetic Data). This time model doesn't consider the shortest time scale, and also does not consider the short term stability as it is not as limiting for the transponder concept as it is for other radars, which are highly affected by short term noise. Also in this time model and analysis we focus on the long term effect.

In the second part, we will design and develop a **Test Bench** that will deliver **Real Data** (green-solid lines, Real Data) of the time difference between two clocks. This data can be used to explore noise and frequency stability ($\Delta f/f$, which will be explained in detail in the next chapter) of the clocks using Allan Variance tools and validate and characterize the clocks. **Test Bench** data output of time difference data can be used with the **LFR Time Model** in the simulator to produce and estimate clock drift $\frac{\widehat{\Delta f}}{f}$ (pink-solid line). This estimated clock drift can be used with the **LFR Time Model** to estimate the time difference between Orbiter ($\widehat{OT}$) and Lander ($\widehat{LT}$) times to know the estimated phase difference ($\Delta\widehat{\varphi}$) (magenta-dotted line). The time difference ($\Delta\varphi$) measured by the test bench can be compared to the estimated time difference ($\Delta\widehat{\varphi}$) to characterize and validate the reconstruction of the phase and time (red blocks).

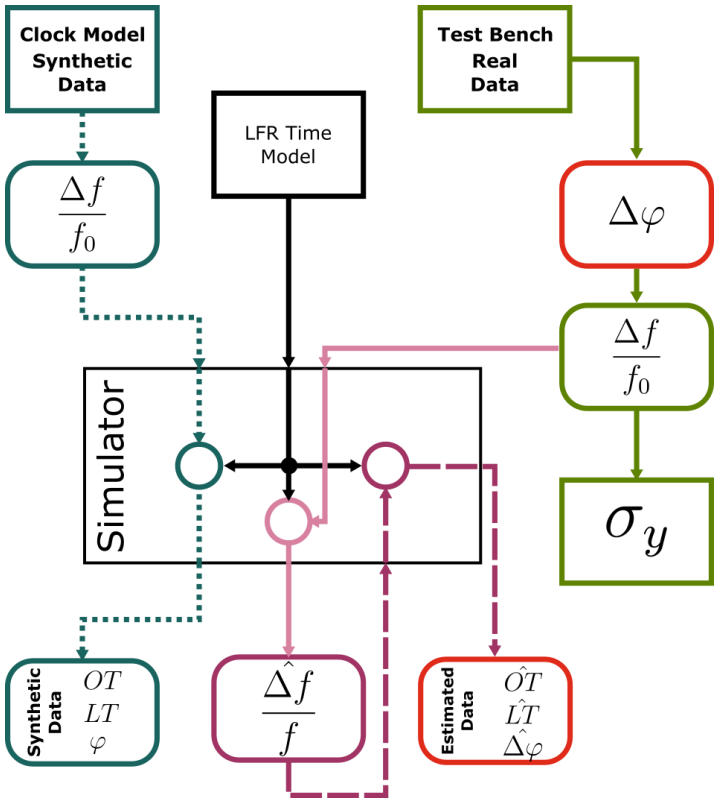

Figure 13. Block diagram of the methodology and steps of the thesis.

2.3.1. Research objectives

This thesis presents the time analysis, tools and software development to understand the time errors in long time scales for a bi-static radar used to study the internal structure of an asteroid.

- **Purpose:** Improve science return by providing compensation methods for the phase and propagation delay measured by directly measuring the clock drift between clocks during operation. Improve operation design in calibration and synchronization by understanding time generation signals. Improve the electronic design by providing information with the time analysis.

- **Problem:** Two electronics means two clocks, therefore clock drift between clocks will affect the measurement. Also, the system introduces time errors which can degrade the signal quality.

- **Solution:** By studying the time analysis of the transponder, and how the clocks generate the time signals we can characterize the clocks, and moreover create compensation techniques to remove the deterministic errors introduced by the clocks. This will lead to an improvement in the operation design as well as in the electronic design of the instrument itself.

2.3.2. Thesis organization

During **Chapter 1** we gave a brief explanation of the scientific objectives and the justification of the mission. Explaining the importance of the internal structure study of asteroids, showing the scientific interest but also an applied interest in planetary defense and future human exploration and exploitation.

Chapter 2 showed an explanation of bi-static radar and an introduction of electromagnetic wave tomography. We briefly described the CONSERT experiment aboard Rosetta, from which LFR inherits its design. Also, we gave the general description of LFR and a detailed revision of the specifications and requirements, followed by a complete review of the electronics and digital processing used for the bi-static radar. These two first chapters function as the background of this thesis.

After these first two introductory chapters, we will introduce in **Chapter 3** the time analysis of the transponder. This chapter will set the base of the theoretical time analysis of the radar used. Since a bi-static radar coherent result depends on the knowledge of both electronics' times and phase with accuracy, we need a complete time analysis from clock generation to operational concepts. First we start with an explanation of how the clock signal is generated and the frequency and time stability of clocks. Subsequently, we show the long-term time analysis of the bi-static radar, explaining each of the time scales of interest. The time errors in each time scale have different effects but they are correlated. We also propose a change in the transponder structure to be able to measure clock drift between clocks. With this time analysis we observe in what manner

errors are introduced in the propagation delay measurement and we are able to compensate for these errors.

In **Chapter 4** we explain in detail from design to development and results, a simulator of the long term operation of the transponder concept. This simulator uses the time model developed in Chapter 3 and in conjunction with the clock model presented too in chapter 3 the simulator is capable of synthesizing the time deviation between both clocks. This simulation will let us have a full understanding of the correlation between the errors and the effects at different time scales. Also, it will let us explore in a first approach the clock drift technique proposed in the last chapter.

To validate this analysis and compensation, we needed real data from clocks. In **Chapter 5** we explain the design and implementation of a test bench to measure time difference and accumulated time error between two clocks. We describe the selection of the clocks used for the mission and the processing performed to process the data and validation of the test bench.

In **Chapter 6** we explain in detail how to introduce the data into the simulator to test the compensation methods. We cover the compensation methods used for the Sounding to Sounding frequency requirements. We define the accuracy of the clock drift measurement as well of the compensation methods. We also present the validation of the clocks for the selected mission.

And finally, in **Chapter 7** we give a review of the important conclusions obtained during this thesis and we expose our ideas for future work and perspectives about a Low-Frequency Radar for asteroids tomography.

Chapter 3. LFR Time Analysis

3.1. Introduction to clocks

The time analysis starts from the clock signal generation. Understanding the process of generation and how it is affected by environment and design is crucial for the time analysis of the transponder concept. Therefore first we will review the clock signal generation.

The use of clocks is reported since ancient times, where mechanic and solar clocks were predominant. Nowadays timekeeping has been taken over by electronics. Keeping track of time is fundamental for several human activities, from knowing at what time to wake up to go to work to navigation and exploring the universe. Some of the most notable uses of timekeeping are radio astronomy, the study of elemental particles, and navigation signals like GPS. There are different techniques to measure time, but currently, the most-used technologies are based on crystal oscillators and atomic references.

How to generate time? A periodic event such as the rising of the sun can be used to define time. The relationship between the frequency of the event's occurrences and the time between them is $frequency = 1/time$. The oldest frequency standard was the rotation of the Earth, where the time between events is a day. The need for time events shorter than a day made the invention of clocks inevitable.

A clock is composed basically of two components: an oscillator and an event counter. The oscillator or frequency standard is any system capable of generating a waveform that is periodic and with a fixed frequency and the event counter is capable to count the transitions generated by the oscillator. We will see later that this "fixed" frequency will vary over time for different reasons. Nowadays we recognize three classes of frequency standards: mechanical resonators, electronic resonators and atomic resonators (Hellwig, 1977). The technologies most used for timekeeping are mechanical quartz crystal oscillators and atomic resonators.

3.1.1. Types of oscillators

Atomic resonator

The atomic reference is based on the resonance of atoms. In a gas, the atoms have one of two possible energy states, referred to as hyperfine levels. These two types of atoms in the gas are almost equal in number. It is possible to separate both states using, for example, a magnet. One of the two states is subjected to microwave radiation. This microwave radiation will trigger the changing of some of these atoms to the other state. The number of atoms that change state depends on the frequency applied: the closer the frequency of the radio wave is to the resonance frequency of the atom, the more atoms will change state. **The SI unit of time, the second, is currently defined by taking the fixed numerical value of the cesium frequency $\Delta\nu_{Cs}$, the unperturbed ground-state hyperfine transition frequency of the cesium 133 atoms, to be 9,192,631,770 when expressed in the unit Hz, which is equal to s^{-1}.** ("BIPM - revision of the SI," n.d.).

Quartz Crystal Resonator

Quartz crystal resonators use the piezoelectric effect of quartz crystals. This means that compression or dilatation of the crystal will generate a voltage, and conversely, a voltage applied to the crystal will generate compression or dilatation of the crystal. This effect depends directly on the orientation of the cut of the crystal, so this property is taken in advantage to produce different types of crystal oscillators. This generated oscillatory signal is then used with an event counter to stablish a counting of cycles letting to measure time in multiples of the period of the signal generated.

Since the frequency depends on physical characteristics of the quartz and of the electronic circuit involved, environmental changes will produce an effect on the frequency generated.

3.1.2. Frequency stability

The accepted way to characterize an oscillator is by its stability, i.e. how precisely and for what time the frequency standard can deliver a specific frequency without change. The stability will be affected by different processes that will be explained later in this chapter. The terms *accuracy*, *stability*, and *reproducibility* are often used in

the qualification of frequency standards. Figure 14 shows a visual representation of stability and accuracy. Reproducibility means that after the system is turned off and after some time turned on again, it can continue having the same stability and accuracy as it had before.

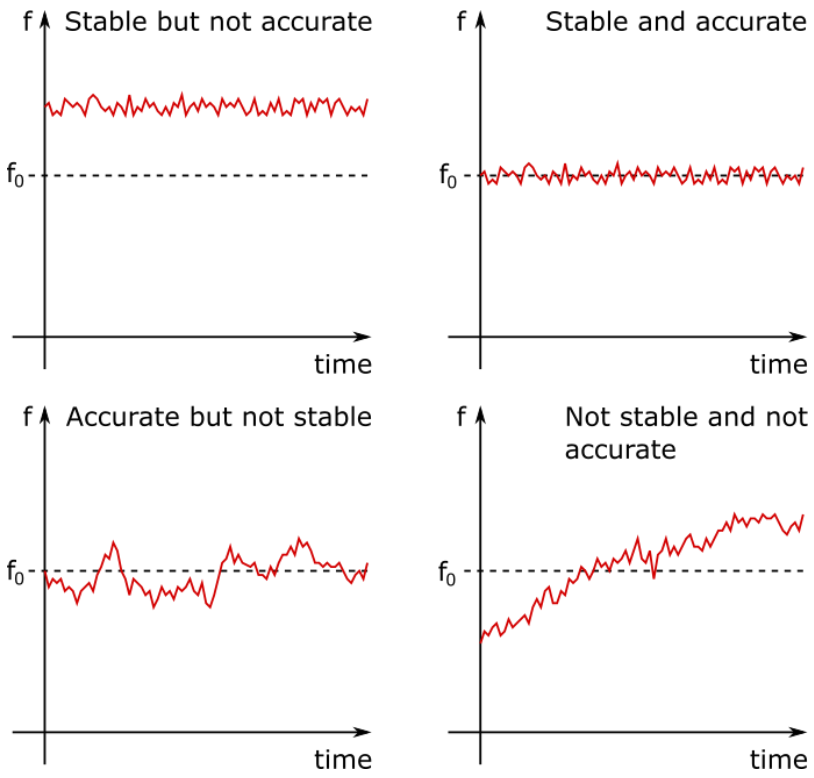

Figure 14. Clock stability characterization. Clock characterization depends on two main characteristics: the stability and accuracy of generating a specified frequency for all time (Riley & Riley, 2008).

Time-domain stability analysis is usually done with measurements of time error (phase) or fractional frequency between clocks. The usual model for an oscillator signal of a sinus clock generator is as follows (Riley & Riley, 2008):

$$V(t) = [V_0 + \epsilon(t)]sin(2\pi f_0 t + \phi(t))$$

Where V_0 is the amplitude of the signal, $\epsilon(t)$ is a random variation in the amplitude, f_0 is the nominal frequency and $\Phi(t)$ is the function describing how the phase changes over time. In this case, we consider that the variation in amplitude $\epsilon(t)$ is negligible and does not introduce a change in phase. And we also consider that signal is sinusoidal and doesn't contain any higher-frequency harmonics coming from non-

linearity in the generation. This case of small-amplitude noise $\epsilon(t) \ll V_0$ is very common for high-quality generators (Allan, Howe, Walls, & Sullivan, 1990).

Frequency stability analysis requires studying the variations in instantaneous frequency, which is the time derivative of the phase (Howe, Allan, & Barnes, 1981):

$$f(t) = f_0 + \frac{1}{2\pi}\frac{d\phi}{dt}$$

One must understand that for oscillator measurements we need two oscillators. So we will always compare one oscillator against another, almost always comparing against one several orders of magnitude better. Due to the dual nature of the measurement, it is useful to define the fractional frequency — a dimensionless value to be used for the stability analysis. This dimensionless value is also known as the frequency offset and in the timing and frequency literature is commonly expressed as y and it is the difference between an oscillator and the reference (nominal value), divided by the reference:

$$y(t) = \frac{\Delta f}{f} = \frac{f(t) - f_0}{f_0}$$

Also, this value can be measured in time domain. It involves the measurement of phase difference between both clocks.

$$\frac{\Delta f}{f} = \frac{\Delta t}{T}$$

Where Δt is the phase deviation, or accumulated time error, and T is the measurement period.

It is impossible to measure instant frequency; so a sampling time is needed between to phase difference measurements. So what we are really measuring is the average fractional frequency $\bar{y}$ over that duration τ is (Allan et al., 1990):

$$\bar{y}(t) = \frac{x(t+\tau) - x(t)}{\tau}$$

Where $x(t)$ is the time difference between clocks in seconds and τ the time between measurements also in seconds.

The stability of the oscillators will be affected by several different processes, for example, temperature, time, vibration, radiation, phase noise, as represented in Figure 15. These processes generate an effect called drift. Drift is the systematic and random change in frequency of the oscillator over time. We can divide these processes into two main groups: deterministic and random.

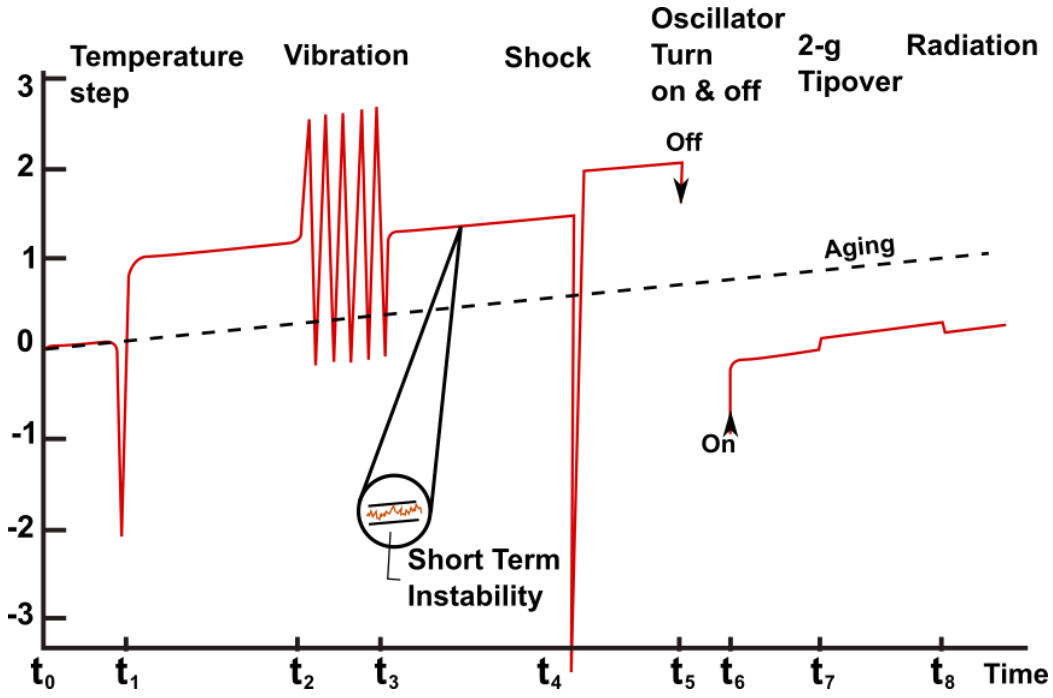

Figure 15. Processes that affect the frequency stability in a quartz oscillator modifying the output frequency (Vig & Meeker, 1991)

3.1.3. Deterministic processes

The major long-term influence over stability comes from deterministic processes. We will focus our attention on specific processes that, due to the nature of the planetary mission, are the ones with more impact on the operation of the instrument.

Aging

Aging is the process that generates frequency changes in time when the oscillator is measured with all the other environmental variables constant. This means that this is an internal process of the oscillator. It appears to be a mass transfer from or onto the resonator surfaces. This means that to reduce this effect, the oscillator should be sealed in a fully hermetic package.

Aging can take any sign — positive or negative — and sometimes it can change sign. Aging is usually modeled as a logarithmic effect, meaning that at the beginning the changes are greater than later on. After this initial stabilization time, it is usually common to use a linear model to describe the effect of aging for short time periods. This process continues even if the clock is turned off, but at the time that it is turned on it can start a new aging cycle (Vig & Meeker, 1991).

It is important to not confuse this process with clock drift. In this case, aging is inherent to the oscillator, leaving out all the environmental effects that contribute to the complete clock drift (*MIL-PRF-55310F*, n.d.).

Temperature

The temperature will affect the frequency stability of the oscillator, as well of all the electronics involved in the clock generation, (i.e. power supply, cables, boxes). In planetary missions the temperatures for the electronics can vary drastically depending on whether the spacecraft is in the sun or is shadowed by the body of study. This could make the temperature one of the principal contributors for frequency instabilities in the project.

This relation between temperature and frequency stability depends on the type of cut to create the crystal used. Different cuts drive different temperature dependence functions (Ballato & Vig, 1978). One way to reduce this effect is to use a temperature-compensated oscillator or, like in this project, an Oven-Controlled Crystal Oscillator (OCXO). The OCXO includes an oven which maintains the temperature of the oscillator constant. This type of oscillator improves the changes in stability due to temperature variations, but nevertheless it does not eliminate them.

Initial frequency offset

Even if two oscillators are marked with the same nominal frequency, due to inaccuracies in the elements and fabrication the real frequency will not be exactly the same. This means that when turned on and after the stabilization period the two frequencies are close but different. This difference in frequency will accumulate time error over time.

Others

There are other processes that create changes in the frequency of the oscillator, such as radiation and power supply variations. These processes do not generate stability changes as important as the processes heretofore mentioned, and can or cannot be taken into account for simulations and analysis. In the next section, we will take real values of real clocks to understand the order of magnitude of the changes in stability for each process, but first, we will review the random processes.

3.1.4. Random processes

Random processes do not have a deterministic response. This makes them aleatory, but it is possible to characterize them in a probabilistic way to provide some predictions. These elements are present in oscillator signal generation, producing random phase changes and random frequency variations over time.

The most common way to describe phase noise or random phase fluctuations in the frequency domain is $S_\varphi(f)$, defined as the one-sided power spectral density, with physical dimensions rad^2/Hz. The standard 1139 IEEE recommends the use of $\mathcal{L}(f)$ where $\mathcal{L}(f) = \frac{1}{2}S_\varphi(f)$ (IEEE Standards Coordinating Committee 27 (SCC27) on Time and Frequency, IEEE-SA Standards Board, & Institute of Electrical and Electronics Engineers, 2009).

The most-used model for describing the phase noise in oscillators is a power-law function:

$$S_\varphi(f) = \sum_{i=-4}^{0} b_i f^i$$

Where b_i is the coefficient of intensity at that exponent of the power law, and f is the frequency in hertz, normally measured from the carrier. This function normally is plotted on a log-log scale. This plot will give insight into the type of noise that is present in the oscillator depending on the slope of the plot, as shown in Table 4 and Figure 16 (Rubiola, 2008).

These types of noise are regularly encountered in signal generation. In telecommunications and radar, this phase noise represents limits to the accuracy of the measurements and transmission (Rubiola, 2008). The magnitude and frequency values will vary from types of oscillators, we will present in the next sections 3 clocks, one used in CONSERT and 2 selected for LFR to see the orders of magnitude that we will encounter.

Table 4 Noise types and their representative slopes in the phase noise spectrum.

Law	Slope	Noise process	Units of
$b_0 f^0$	0	White phase noise	rad^2/Hz
$b_1 f^{-1}$	-1	Flicker phase noise	rad^2
$b_2 f^{-2}$	-2	White frequency noise	$rad^2\ Hz$
$b_3 f^{-3}$	-3	Flicker frequency noise	$rad^2\ Hz^2$
$b_4 f^{-4}$	-4	Random walk frequency	$rad^2\ Hz^3$

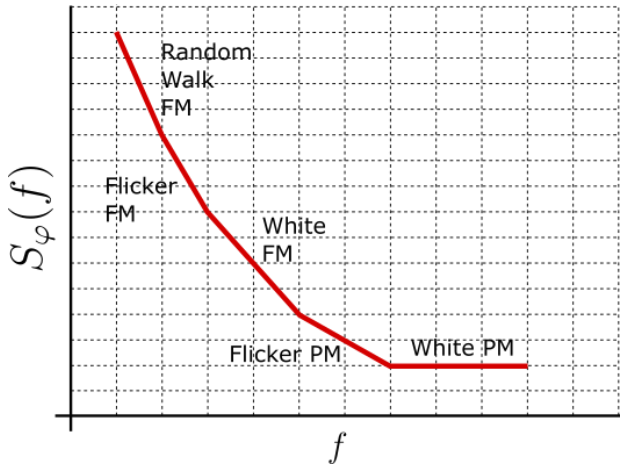

Figure 16. Phase noise profile, showing the power-law model. Notice how different slopes represent different noise types.

3.1.5. Allan variance

The Allan Variance (AVAR) is the most used method to analyze the stability of oscillators. It is the sum of the squared differences of adjacent values of fractional frequency, divided by the number of data points and by two. To obtain the deviation, we calculate the square root of the variance (Allan, 1966; Howe et al., 1981).

$$\sigma_y(\tau) = \sqrt{\frac{1}{2(M-1)} \sum_{i=1}^{M-1} (y_{i+1} - y_i)^2}$$

Where y_i is the fractional frequency defined in the Frequency Stability section, and can be replaced by the real value measured of the averaged fractional frequency $\bar{y}$. From the calculation of the fractional frequency, we can perform averages over different values $m\tau$. This can only be done if there are no dead times between the measurements. The plot of the Allan Deviation (ADEV) as a function of τ gives valuable information about the type of noise, in the same manner as the power-law function does for the phase noise. The ADEV slopes describe the type of statistics that the noise presents (see Figure 17).

From the AD, other tools were developed to characterize different noise types that the normal AD is not able to distinguish. Therefore for this work, we will base the time domain analysis in the Modified Allan Deviation (MDEV), symbolized here by $M\ \sigma_y(\tau)$. It is a simple variation of the AV that includes an additional average over phase which helps to differentiate between White and Flicker Phase noise, which the AV is incapable of doing.

$$M\ \sigma_y(\tau) = \sqrt{\frac{1}{2m^4(M-3m+2)} \sum_{j=1}^{M-3m+2} \sum_{i=j}^{j+m-1} \sum_{k=i}^{i+m-1} (y_{k+m} - y_k)^2}$$

It is possible to convert from the phase spectrum to the time domain variance, but it is only approximate and will include errors. There are some advantages of the use of the variance as they incorporate the effects of the spur signals, which are difficult to evaluate in the phase spectrum.

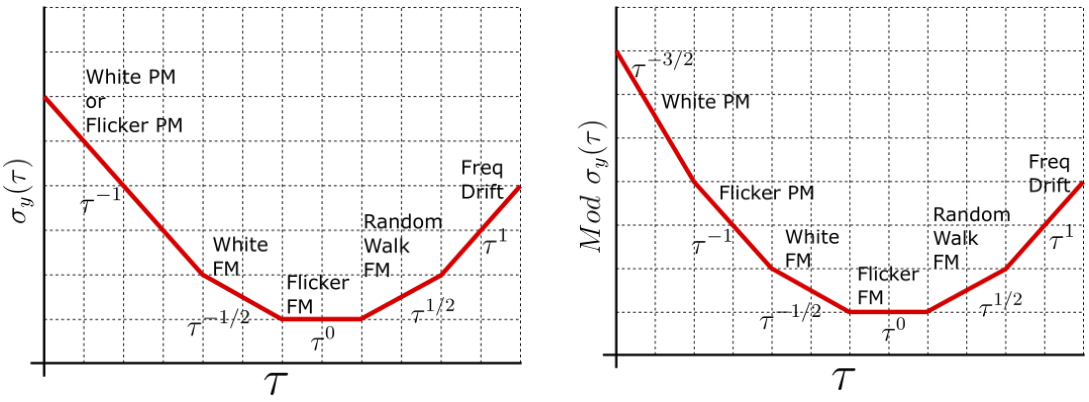

Figure 17. Allan Deviation and Modified Allan Deviation plots in logarithmic scale. Each slope represents different types of noise. Notice that the MAD solves the difference between White and Flicker Phase noise. (Re-edit from (Riley & Riley, 2008))

3.1.6. Clock model

The most used documents in terms of standards and normativity in oscillator design construction and characterization are: (IEEE Standards Coordinating Committee 27 (SCC27) on Time and Frequency et al., 2009) and (*MIL-PRF-55310F*, n.d.).

These documents use a clock model which includes different types of parameters that affect the stability of the clocks, including, aging, temperature, initial frequency offset, etc. The clock model used is

$$x(t) = T_0 + y_0 t + \frac{1}{2}at^2 + \int_0^t T(t)dt + \int_0^t V(t)dt + \cdots + \varepsilon(t)$$

Where:

$x(t)$: $Time\ Error$
T_0: $Initial\ Time\ Error$
y_0: $Initial\ Frequency\ error$
a: $Aging$
$T(t)$: $Temperature\ error$
$V(t)$: $Voltage\ error$
$\varepsilon(t)$: $Random\ noise\ process$

The ellipsis shows the possibility of including any other type of process that could change the frequency of the clock, but in this case, we will use only the ones shown.

The aging in this model proposed is a linear model, which is useful for short terms of time, we will include instead of this basic model the one provided by Rakon for its clocks which is a logarithmic model.

$$ag(t) = A \cdot \ln(Bt + 1) + C$$

Where A, B, and C are parameters obtained by the characterization of the clock. So we will include this model in place of the linear model.

$$x(t) = T_0 + y_0 t + \int_0^t ag(t)dt + \int_0^t T(t)dt + \int_0^t V(t)dt + \cdots + \varepsilon(t)$$

3.1.7. CONSERT and LFR clocks

It is convenient to look at the specifications of the clocks selected to understand the order of magnitude and units used by all of these processes. For instance, in Table 5 we find the specifications of the clocks used for the CONSERT and LFR instruments. In the subsequent paragraphs, we will analyze the CONSERT clock values, but it is just needed to do a comparison in the orders of magnitude to evaluate of the same manner the other clocks, but considering that CONSERT clocks have the lower frequency stability it will give an order of the worst possible errors.

The clocks selected for CONSERT were EWOS 0513 from SOREP. These clocks were Oven Controlled Crystal Oscillators (OCXO) — this means that the package includes an oven to maintain temperature around the crystal constant. This reduces the frequency dependence on temperature. These clocks are low-power-consumption and very small in size and weight, making them the best option for the instrument. More accurate clocks, such as atomic clocks, lack the size, weight and power consumption characteristics to be an option for the planetary constraints assigned to CONSERT. It is important to notice that the clocks used in CONSERT had a real performance better than the announced.

The clock selection for LFR was made in accordance with the planetary constraints of size, weight, price, and power consumption, and with the absolute frequency requirements needed for the transponder that will be explained in detail in the next sections. From several models, 9 in total, we chose two clocks that we were able to

adjust to our needs. The selected clocks were from Rakon and Syrlinks. More information about these clocks will be given in Chapter *Real clock measurement.*

For the temperature, the relation of frequency stability to temperature is usually described as linear for the possible working interval. In some cases for OCXO, the function between stability and temperature can be different, but usually, the operating temperatures are specified for the linear range.

Table 5 Main characteristics of CONSERT Master Oscillator EWOS 0513 from SOREP. (The data is taken from (Barbin et al., 1999)). And the main characteristics of RAKON and SYRLINKS selected clocks for LFR.

	Unit	SOREP EW OS513 CONSERT	RAKON 408 LFR	EWOS 0830 LFR
Operating temperature range	$°C$	-40 to +60	-40 to 75	-30 to 70
Mass	g	5	70	15
Volume	cm^3	2.5	40	<10
Power supply warming up	mW	1200mW for less than 1 minute	5000	2000
Warm-up time	s	60		
Power supply steady state @ -40°C	W	175 in vacuum	3	0.5
Power supply steady-state @+25°C	mW	60 in vacuum	-	-
Frequency stability vs. Temperature	ppm	0.4 from -40 to +60°C	0.06	0.02
Frequency stability vs. supply voltage	ppm	0.2 from 4.75 to 5.25V	0.001	0.004
Short term Allan variance ($\tau = 1s$)		$5 \cdot 10^{-11}$	$5 \cdot 10^{-12}$	$4.1 \cdot 10^{-11}$
Aging per year	ppm	1	0.1	0.1
External Frequency Control Range	ppm	10		

For the specific mission of CONSERT and LFR, the temperature variation of interest is the temperature difference between both clocks. This means that if both clocks are varying in temperature in similar ways, the frequency stability changes can also be similar. The expected temperature for the orbiter is close to 20 °C and for the Lander is expected a large variation depending on the final landing position (i.e. -25 to 5 °C). We will observe the worst scenario to have an idea of the possible frequency deviation possible for this case. The worst scenario is when the clocks are at opposite

temperatures (one at -40 and the other 60°C), which could be a possible scenario when one clock is in the shadow and the other one is illuminated by the Sun — although the difference is expected to be smaller due to the fact that the electronics will generate heat, reducing the change inside the electronic box. In this case of both clocks being at opposite temperatures, the frequency stability change could be as large as 0.4 ppm, supposing linear and equal change for both clocks, and this could drive the clocks' stability beyond the specified constraints. This means that temperature could have a significant impact on stability and in the measurement.

Changes in the power supply will also generate changes in the stability, but as we can see from Table 5, the value of the changes in stability against voltage supply variation are lower than the ones due to temperature. The maximum change is expressed for a 5% change in the power supply. This is a huge change in voltage and we expect smaller changes in the power supply source. There is a dedicated DC/DC converter to stabilize the power supply, meaning that the changes in the power supply of the clocks will be negligible against other types of processes affecting the stability.

Aging is not a problem for small time intervals, i.e. a Scan, but it is of interest at the start of the internal study mission. It is common for planetary missions to have a travel time on the order of years from launch to starting the science phase. This time could take the clock stability to values that are not in compliance with the constraints imposed for the instrument. In this case, we can see that over a year the stability can be changed on the order of 1 ppm per year. If both clocks age in different directions or at different rates, this effect could take them outside the compliance range, needing a calibration before starting the mission. The CONSERT experiment revealed that the specifications of the clocks were some orders of magnitude better in aging than the value reported in the datasheet. This could make us think that newer clocks could have this improved behavior reducing the effects during long terms of time.

Short-term stability is usually depicted as an Allan variance or Allan deviation value. These values give the expected noise at a certain averaging time, usually on the order of seconds. However, to have a complete idea of the short-term noise it is also important to see the phase noise profile, given in the clocks' datasheets. This phase noise profile can be converted to a root mean square value of jitter that is much easier to work with, but also gives a hint towards the type of noise we can expect. In our case for

all clocks, the phase noise results lower than the absolute requirement of 0.1 ppm for Coherent Accumulation time scale, showing a 10^{-11} variance for 1 second.

3.2. Requirement analysis for each time scale

The use of the in-time transponder concept explained in the CONSERT section Figures 5 and 6, reduces the frequency requirement from 10^{-12} to 10^{-7}, but it splits the requirement into four different time scales. This time scales are distributed from short term to long term. The effects of the clock drift will have a different impact at each time scale, but the errors will be correlated. We recognize for the transponder concept four different time scales that are: Coherent accumulation, Ping to Pong, Sounding to Sounding, Tx-Rx window (Figure 18). All of them will be explained in detail later.

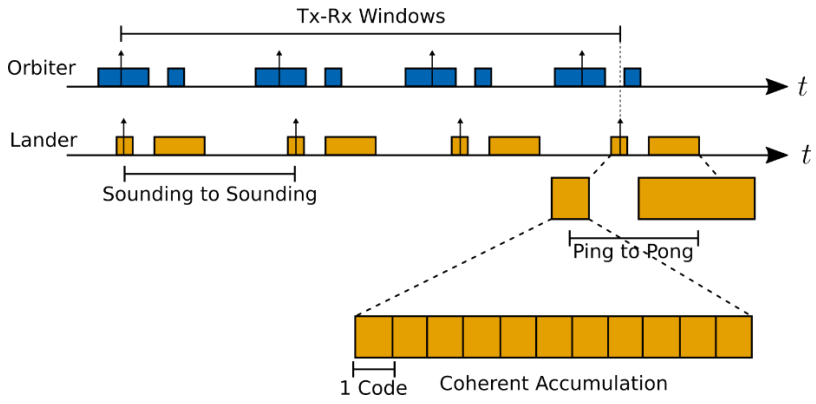

Figure 18. Time scales in transponder structure. We recognize 4 different time scales. The timeline in the diagram represents a Scan where several Soundings are Performed.

We recognize two different types of frequency requirements that can be addressed separately: absolute and stability type.

- **Absolute**. Where the frequency difference between the two clocks should be less than a given maximum to allow science return. This type cannot be compensated in post-processing.

- **Stability**. Where the knowledge of the frequency drift permits compensation in post-processing and it is not mandatory for this to be satisfied during the mission to allow science return.

3.2.1. Coherent accumulation

The transponder structure is designed to transmit the signal through the asteroid; the Lander and Orbiter do not have sufficient power to transmit the signal to the other instrument and receive it with sufficiently high SNR.

To overcome this low SNR at reception, a coherent accumulation of several codes is performed. A change in phase from code to code will degrade the improvement of the SNR. The constraint for Coherent Accumulation is that the phase drift must be less than 80° in the 60 MHz carrier, which is 3.7 ns for 2048 accumulated codes and 160°, which is 7.4 ns for 1024 codes. There are 2048/1024 codes accumulated, which is approximately 26 ms/13 ms of accumulation time respectively. This value was chosen in order to have a decrease of 3 dB in the SNR of the signal accumulation with clock drift with an additive white Gaussian noise. This analysis could be found in Annex C. The more codes accumulated the better the SNR, limited by clock drift and by the relative movement of the Lander with respect to the Orbiter to allow the full transmission window to travel the same path.

This requirement is an absolute requirement and needs to be achieved by design or by calibration before the operation. No compliance in this constraint results in no science return, there is no possible post-processing correction.

3.2.2. Ping to Pong

It is the time between reception and transmission in the Lander. This time should remain constant in the orbiter reference for all soundings in the whole orbit.

The calendar accuracy must be better than the signal resolution over twenty. This means that the error time in the calendar between reception and transmission of the Lander should be less than approximately 2 ns considering a time symbol of 50 ns and a time between Ping and Pong of 100 ms. This constraint guarantees that the propagation delay error is 20 times smaller than the symbol time and will not affect the detected peak position.

This time error impacts directly the propagation delay measurement. This requirement is a stability type, the knowledge of the clock drift between both clocks can be used to compensate this error in post-processing.

3.2.3. Sounding to Sounding time reference

The time from one Sounding to the next Sounding should remain stable for the whole orbit or at least several Soundings. The time error should be less than one sampling step over several minutes. This means 8.33 ns over 10 minutes which means 120 Soundings with 5 seconds between Soundings. A time error less than this is sufficient to avoid a movement of the peak by the clock drift. Any miss-detection of the peak due to low SNR can be reconstructed and the data re-synchronized.

This requirement is a stability type, the knowledge of clock drift between both clocks can be used to compensate the error on post-processing.

3.2.4. Sounding to Sounding phase reference

From Sounding to Sounding, the phase between clocks should remain stable. As in the coherent accumulation, the requirement objective is a change no larger than 80° of the carrier signal over several Soundings to allow coherent processing. In this case, a change of less than ~ 3 ns of the carrier during 1 hour is needed to allow coherent processing.

This constraint permit to improve the science return with a coherent analysis using data for different Soundings for 1 hour. This requirement is of the stability type, where knowledge of the clock drift between clocks can help to compensate this error.

3.2.5. Tx-Rx windows

The calendars in Lander and Orbiter should remain synchronized during the whole orbit. The reception window of one electronic should be synchronized with the transmission window of the other electronic. This permits to establish the transponder communication. One could expect that windows move few codes: this means 10 ms during 12 hours of the complete orbit. In this case, extra care is taken: as shown in Figure 18, we use a larger transmission window than the reception window, allowing

some error margins in the calendar drift. The bigger this window movement the bigger the transmission window should be to avoid the reception window to fall outside.

The transmission window can be extended but will impact power consumption. This is an absolute type requirement. Failing to comply with this constraint means no science return. It is not possible to compensate in post-processing.

3.2.6. Frequency stability summary

In Table 6 are all the constraints condensed for different time scales and for different time references as the phase of carrier, time symbol or few codes. The frequency requirements are expressed as $\Delta T/t$ where ΔT is the allowed time change and t is the time period over which the change is allowed. Each column is a time scale, and each row the time reference used. The two absolute type requirements are marked in orange.

Table 6. Frequency requirements are shown for each time scale and for the time reference needed. The values shown are just the order of magnitude.

	Coherent Accumulation (~26 ms/~13 ms)	Ping to Pong (~100 ms)	Sounding to Sounding (~1 hour / ~10 min)	Tx-Rx Window (~12 hours)
Carrier Phase (~3 ns)	10^{-7}		10^{-12}	
Time Symbol (50 ns)		10^{-8}	10^{-11}	
Few Codes (10's ms)				10^{-7}

3.3. Time Model in-time transponder

The main goal for the time analysis of the in-time transponder is to understand how the clock drift will impact the measurements for long periods of time (i.e. one Scan). It is important to remark that the transponder helps to reduce the frequency stability needed by the clocks but it splits this requirement into different time scales. Each time scale will be affected differently by the clock drift but the errors will be correlated. By understanding these errors in each different time scale is possible to design compensation methods for each different time scale.

It is useful to remind the full sequence of the transponder in order to follow the time scales explanation. In a first transmission, the Orbiter sends to the Lander a group of modulated coded signals, the Lander does a coherent accumulation of this codes,

noting that the reception (accumulation) time is smaller than the transmission window to avoid any mismatch in the calendar synchronization due to clock drift. After the Lander pulse compresses the code to find the peak position, and synchronize the same coded signal to that delay and sends it back after a known delay. The Lander again sends a group of codes and the Orbiter does the coherent accumulation and stores the signal to be transmitted to Earth. From this transponder cycle we remember shortly the time scales, explained in the last section, expected in order of time length are:

- **Coherent Addition**: which is the accumulation of codes to improve SNR of the received signal. And the point of interest is the phase at the carrier level.

- **Ping to Pong**: The time between the reception and transmission in the Lander should remain the same for the complete Scan. The reference is at time accuracy level or symbol time level.

- **Sounding to Sounding**: The phase and the calendar schedule should remain constant for all the Soundings in the Scan. The interest is the same as Coherent Addition at carrier level.

- **Tx-Rx windows**: The reception window of one electronic should be inside the transmission window time during the Scan to permit communication. The interest falls in the transmission and reception windows level.

3.3.1. Time events model

The time model used for the transponder is based on time events. There are three main time events in a Sounding that are considered for the analysis — t_{OS}, t_{OT} and t_{OR} — which are the start of the Sounding, Orbiter transmission time and Orbiter reception time (see Figure 19). The time events for transmission and reception are considered in the center of the windows, meaning that there is the same number of codes before and after the time event. All these events are referred to the Orbiter time.

The same time event occurs in both automats (see Figure 19), but the action is different, for example, while in the Orbiter the transmission event is executed in the Lander the Reception event is active.

$$t_{OT} = t_{lR}$$

Both events are activated after the same number of clock cycles of each master clock. But, as the clocks have slightly different frequency due to the clock drift, this time events will not be at the same time.

$$t_{LR} \neq t_{OT}$$

Notice that nomenclature will help to recognize which clock is the reference: upper-case letters will refer to Orbiter time reference and lower-case letters to the Lander time reference. We will use the Orbiter time as the reference for the complete time analysis. To make it simpler also the drawings and plots will use a color code: blue will be used to depict Orbiter related events and color orange will be used for the Lander.

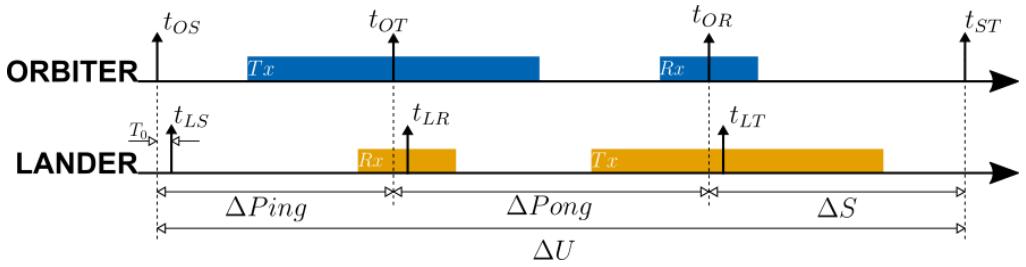

Figure 19. Time diagram of one Sounding. Two different sizes of windows: Transmission longer than the reception window. There are 3 time events: Start time, Orbiter Transmission and Orbiter Reception.

The start of the Sounding is a value which is used as a reference in the Sounding but has no meaning in the operation of the transponder. The times between each time event are named as delta times. As said before, this delta times or the times between time events are multiples of the master clock reference used by the system. As a summary of the time event model:

- There are three main time events:
    - $t_{OS} = t_{lS}$: Orbiter start time is performed after the same number of clock cycles of its master clock than Lander start time with its own master clock. In the same way $t_{OT} = t_{lR}$, $t_{OR} = t_{lT}$.
- Time events are in the center of the transmission and reception windows.

- The time between time events is a multiple of cycles of the master clock in each electronic.

Now we will consider different cases using clock drift and propagation delay values, to understand how the time from one automat is referred to the other. Considering no clock drift $(\Delta f/f = 0)$ and synchronized calendars $(T_0 = 0)$, the time events on the Orbiter and the Lander should be completely synchronized.

$$t_{ls} = t_{OS} = t_{LS}$$

$$t_{lR} = t_{OT} = t_{LR}$$

$$t_{lT} = t_{OR} = t_{LT}$$

Meaning that if a transmission time event from Orbiter to Lander is at t_{OT}, the reception time event is exactly at the same time and the signal will be received time-shifted by the propagation delay of the signal going from Orbiter to Lander. This is the reflection that both electronics count the same number of clock cycles and if both frequencies are equal the absolute time reference will be the same. Instead, if the frequency of both clocks is different even if both electronics count the same number of counts of their clock reference the absolute time reference will be different.

$$t_{ls} = t_{OS} \neq t_{LS}$$

$$t_{lR} = t_{OT} \neq t_{LR}$$

$$t_{lT} = t_{OR} \neq t_{LT}$$

In Figure 20 we show four cases which will let us understand in more detail the effect of the clock drift at measuring the propagation delay. This figure uses and ideal version of clocks and synchronization. The figure represents the transmitted and received signals as a peak from the pulse compression, in dark orange the arrows show the time events.

The first case shows that there is no clock drift and no propagation time delay $(\Delta f/f = 0, \tau_0 = 0)$ this means that $t_{lR} = t_{OT}$. When there is no propagation delay

and times are synchronized the transmitted code is the one received. This is an idealized case, in every system, we expect a system delay caused by electronics.

The second case shows the case where the clock drift is equal to zero and the time delay is different from zero $(\Delta f/f = 0, \tau_0 \neq 0)$. In this case, the propagation measured in the Lander is the same as the propagation delay between both electronics.

The third case shows a system where there is clock drift and the propagation delay is equal to zero $(\Delta f/f \neq 0, \tau_0 = 0)$. The Lander will measure a propagation delay proportional to the desynchronization of calendars.

And the fourth case shows the case where propagation delay and clock drift are different from zero $(\Delta f/f \neq 0, \tau_0 \neq 0)$. In this case, we can see that clock drift will introduce directly an error in the propagation delay measurement.

The instrument is turned on by a command from the onboard clock of the Orbiter and the Lander. It is not possible to guarantee that the two parts will be turned on at the same time, so the start of their calendars will be different. A synchronization process is used to reduce this error to the order of milliseconds typically, but this introduces an initial error T_0 between both calendars. In Table 7 are the time events for one Sounding shown in Figure 19; note that the Lander times are expressed in Orbiter reference time.

Table 7. Time events from the time model showed in Figure 19

Orbiter	**Lander**	
	Referred to last time event	Referred to start time event
$\boldsymbol{t_{OS} = 0}$	$t_{LS} = t_{OS} + T_0$	$t_{LS} = t_{OS} + T_0$
$\boldsymbol{t_{OT} = t_{ST} + \Delta Ping}$	$t_{LR} = t_{LS} + \Delta Ping\left(1 + \frac{\Delta f}{f}\right)$	$t_{LR} = t_{OT} + \Delta Ping\frac{\Delta f}{f} + T_0$
$\boldsymbol{t_{OR} = t_{OT} + \Delta Pong}$	$t_{LT} = t_{LR} + \Delta Pong\left(1 + \frac{\Delta f}{f}\right)$	$t_{LT} = t_{OR} + (\Delta Ping + \Delta Pong)\frac{\Delta f}{f} + T_0$
$\boldsymbol{t_{OS2} = t_{OR} + \Delta U}$	$t_{LS2} = t_{LT} + \Delta S\left(1 + \frac{\Delta f}{f}\right)$	$t_{LS2} = t_{OS2} + \Delta U\frac{\Delta f}{f} + T_0$

Where ΔU is the time between the start time of one Sounding to the next Sounding start time event — what is known as the pulse repetition interval (PRI) and $\Delta S = \Delta U - \Delta Ping - \Delta Pong$. Note that the clock drift is not time-variant during one Sounding but it will be from one Sounding to the next one. This is a result of the

temperature and aging being the main contributors for the frequency instability, both of which are slow time effects. This will not be the case for Sounding to Sounding where the clock drift will be time-dependent. Also note that the short term is not considered, the phase noise and short term values for the possible clocks to be used are sufficiently stable in the short term to not be included in the time analysis.

This model gives the time events for both electronics referenced to the Orbiter time. Note that Lander times are the Orbiter times plus the error coming from clock drift and initial error synchronization.

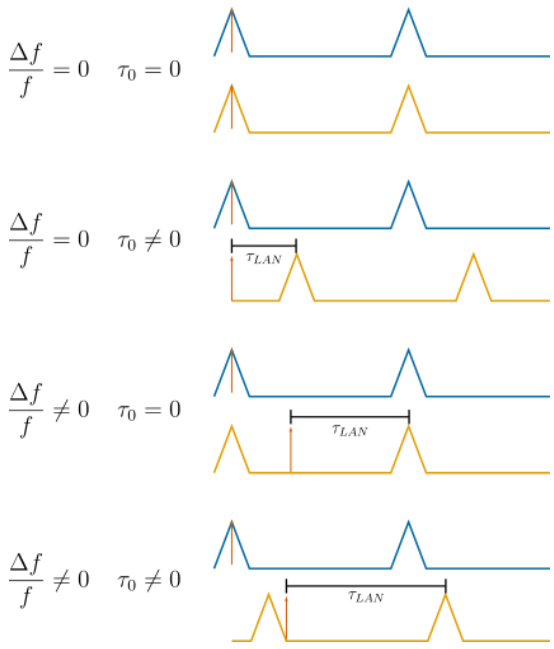

Figure 20. Different possible combinations between propagation delay and clock drift. The peak received will be moved either by propagation delay or by clock drift.

3.3.2. Peak position measured in the Lander

To measure the peak position in the Lander in an ideal system with no clock drift $(\Delta f/f = 0)$ and synchronized $(T_0 = 0)$ it is sufficient to do:

$$\tau_{LAN} = t_{OT} + \tau_0 - t_{LR}$$

Where the τ_0 represents the propagation delay between electronics

(see Figure 21). In the figure, we can see the time events marked as strong orange arrows, the sampling points as smaller black arrows and the triangular peak represents the peak of the pulse compression of the code. $\Delta code$ is the duration of the code, and as we can see it is periodic due to sending several codes in each transmission. In this case, the sampling points in relation to the code size in time are not at scale, but it permits to have a better visualization of the measurement. In the case that there is no clock drift and no initial time error, the peak position measured in the Lander τ_{LAN} is exactly the propagation delay τ_0 between both electronics.

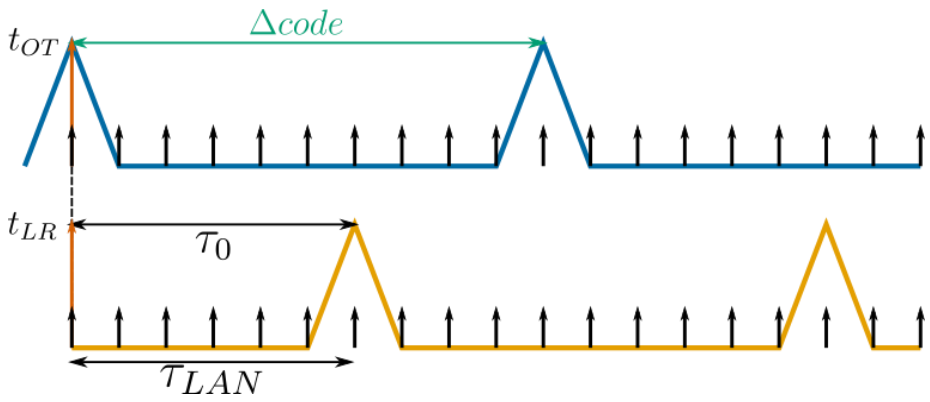

Figure 21. Peak detection measured in the Lander considering no initial time error and no clock drift.

Due to the periodicity of the code for coherent accumulation, the peak position measurement is limited to one code length. In other words, if the propagation delay is greater than the code length, the measurement would need to use other data coming from different instruments to solve the ambiguity. To introduce this limitation, the modulo operator (mod) is applied to the peak position measured by the Lander.

$$\tau_{LAN} = [(t_{OT} + \tau_0) - t_{lR}]$$

$$\tau_{LAN} mod(t_{code})$$

This means that the Lander will measure the propagation delay modulo the code length, limiting the output of the operation to one code length, and needing more information to solve the ambiguity.

By substituting the values of the time events with clock drift and initial time error, we can see the effect on the calculation of the peak position in the Lander.

$$\tau_{LAN} = (t_{ST} + \Delta Ping + \tau_0) - \left[t_{ST} + T_0 + \Delta Ping(1 + \frac{\Delta f}{f})\right]$$

$$\tau_{LAN} = \tau_0 - T_0 - \Delta Ping \frac{\Delta f}{f}$$

3.3.3. Propagation delay measured in the Orbiter

We consider that the signal from reception to transmission on the Lander doesn't suffer or has constant delays from electronics, i.e. it is constant for all Soundings, and the reception and transmission subsystems inside the Lander are synchronized. The phase received is the one that is transmitted back. The propagation delay measured by the Orbiter is obtained in a similar way to the one in the Lander. We take the difference between Lander time event transmission t_{LT} and Orbiter time event reception t_{OR}. Again the modulo operator is applied in order to respect the pulse compression of the code.

$$\tau_{ORB} = [t_{lT} + \tau_0 - t_{OR}] mod(t_{code})$$

By using the values of the time events expressed in Table 7 we obtain the next expression

$$\tau_{ORB} = \left[\tau_0 + T_0 + \Delta Ping \frac{\Delta f}{f} + \Delta Pong \frac{\Delta f}{f}\right] mod(t_{code})$$

As explained before, the propagation delay of the Lander will be included in the propagation delay measured in the Orbiter due to the time-shifting of the code transmitted back to the Orbiter. That is the whole purpose of the in-time transponder structure. Therefore the propagation delay in the Lander will be included in the time-shifting of the original code, expressed in the next equation as $\boldsymbol{\tau_{LAN}}$.

$$\tau_{ORB} = \left[\tau_0 + T_0 + \Delta Ping \frac{\Delta f}{f} + \Delta Pong \frac{\Delta f}{f} + \boldsymbol{\tau_{LAN}}\right] mod(t_{code})$$

After the reduction of terms we obtain the expression of the propagation delay measured in the Orbiter:

$$\tau_{ORB} = 2\tau_0 + \Delta Pong\frac{\Delta f}{f}$$

If the propagation delay measured in the Orbiter is divided by 2, the result is the real propagation delay plus the error coming from the clock drift over the time between reception and transmission in the Lander. This division by two limits the possible propagation delay measurement to half of the code length unless other data is used to solve the ambiguity. In Figure 22 the propagation delay is greater than half of the length of the code. After the second transmission back to the Orbiter and adding the propagation delay measured by the Lander, the total propagation delay is longer than the code length and applying the modulo operator reduces this propagation delay to a value smaller than half of the propagation delay.

The phase propagation over this Ping-Pong is maintained. The phase received is the one that is transmitted back if and only if the reception and transmission subsystems in the Lander are synchronous.

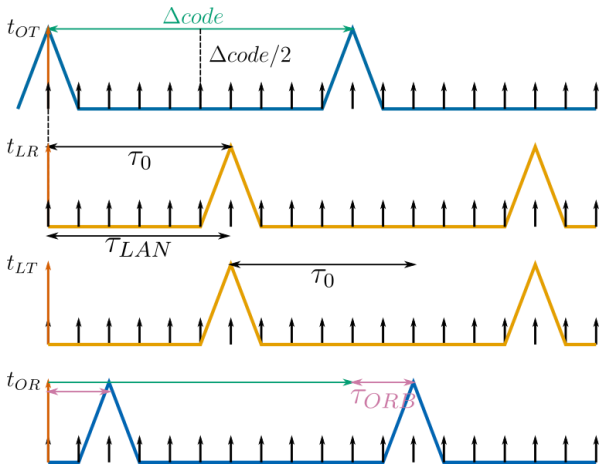

Figure 22. Complete transmission process. Showing the ambiguity introduced by the division by two of the propagation delay in the Orbiter for propagation delays longer than half code length.

3.3.4. Time errors introduced by the system

The transponder model also includes some time errors that come from the system itself, and this means by the real operation of the system. This means that these time errors are not coming from the clock drift but from the way the system works. These errors will help improve the time model of the in-time transponder for the long term.

Sampling time error

As we stated in the electronics description, the reception of the signal passes through an analog to digital converter. This conversion samples the signal with a specific sampling speed — 120 MHz. There is the possibility that the transmission peak will arrive in between two sampling points, in contrast with the last analysis where we considered that the peak arrived in exactly a sampling time. This will make a shift of the peak to the nearest sampling point, ahead or behind, in the Lander, causing an error in time $\Delta\tau_{LAN}$ (see Figure 23). The sign of $\Delta\tau_{LAN}$ will depend on whether the arriving peak is closest to the previous or the next sampling point.

Because the system is asynchronous, the reference is lost from Sounding to Sounding, causing this error to be uniformly distributed in one sampling step. This error is introduced in both receptions. The Orbiter sampling error can be reduced by using post-processing techniques to enhance the accuracy like in CONSERT (Pasquero et al., 2017); however, we expect less error in LFR due to the 120 MHz sampling frequency. If there is need to measure the propagation delay in the Orbiter during the mission or without any post-processing there will be the same effect on both sides.

For the case of the Lander, this error is added directly to the measurement of the propagation delay.

$$\tau_{LAN} = t_{OT} + \tau_0 + \Delta\tau_{LAN} - t_{lR}$$

This error is calculated by taking the modulo of the propagation delay measured in the Lander τ_{LAN} with respect to the sampling period $Ts = 1/Fs$.

$$\Delta\tau_{LAN} = (t_{OT} + \tau_0 - t_{lR})\, mod(Ts)$$

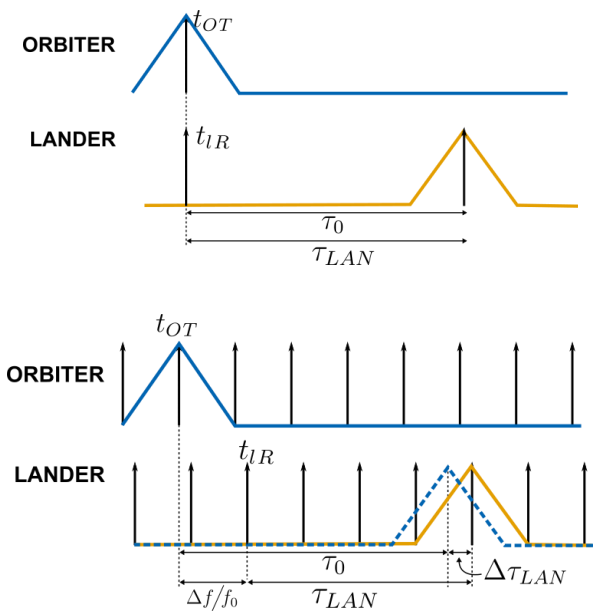

Figure 23. Sampling error effect. Top: peak position measured in the Lander with infinite time accuracy. Bottom: jitter caused by the reception of a peak between two sampling points. The result is a time error added to the peak position and change in the power received.

SNR peak time error

The signal-to-noise ratio of the received signal will directly impact the accuracy of the detection of the peak. This means as the SNR is lower, the peak detection is harder to achieve, and it can be displaced, introducing an error in the time of detection. The relationship between SNR and the peak detected can be described with the variance in the estimation of the propagation delay coming from the Cramer Rao Lower Bound (CRLB). Even though this model is very simple, it can give a first approximation of the expected movement when the signal has sufficient SNR to detect a peak. This model considers a limited-bandwidth signal, a limited-bandwidth reception system, and that the expected noise inside this bandwidth is pure white noise (Kay, 1993). This model is also more accurate at high SNR values, so we consider for the application of this model that the signal detected is the true peak and there is no error in the peak detected with any other side lobes.

$$var(\hat{\tau}) = \frac{1}{SNR_E \times B_{RMS}^2}$$

Where SNR_E is Signal-to-Noise Ratio in terms of energy of the signal and B_{RMS}^2 is the Root Mean Square bandwidth of the signal.

The Root Mean Squared bandwidth is defined by

$$B_{RMS}{}^2 = \frac{\int_{-\infty}^{\infty}(f)^2|S(f)|^2 df}{\int_{-\infty}^{\infty}|S(f)|^2 df}$$

As the coded signal used is a pseudorandom code MLS, the spectrum is constant inside the signal bandwidth, therefore:

$$|S(f)|^2 = A \qquad over\ 2B$$

$$B_{RMS}{}^2 = \frac{\int_{-B}^{B}(f)^2 A\, df}{\int_{-B}^{B} A\, df} = \frac{B^2}{3}$$

The result is the same for a band-limited signal that is not centered at 0 frequency.

So the variance of the estimated time delay is:

$$var(\hat{\tau}) = \frac{1}{SNR_E \times \frac{B^2}{3}}$$

The SNR_E is based on energy, so to be able to use power SNR we can use the following conversion:

$$SNR_E = \frac{E_s}{N_0/2}$$

Where $N_0/2$ is the power density of the noise and E_s is the energy of the signal defined as

$$E_s = \int_0^{T_s} s^2(t)dt$$

And the power:

$$P_s = \frac{E_s}{T_s}$$

Where T_s is the duration of the time signal. The noise is defined by

$$P_n = \frac{N_0}{2} 2B$$

$$SNR = \frac{P_s}{P_n}$$

Therefore the energy SNR_E based on the power of the signal is as follows:

$$SNR_E = 2BT_sSNR$$

Where B is the bandwidth of the system, T_s is the observation time of the signal and SNR is the known Signal-to-Noise ratio between powers.

$$\sigma_{\hat{\tau}} = \frac{\sqrt{3}t_{Symb}}{\sqrt{2BT_sSNR}}$$

In our case, the bandwidth is limited at reception by the antenna and filters. Limiting the Bandwidth to 20 MHz, the same as the signal bandwidth, the length of the signal T_s is one code length that is the observation time, i.e. 255 symbols times 50 ns. And the SNR is the expected ratio of power and noise expected at the output of the coherent accumulation. We must emphasize that this model comes from de Cramer-Rao Lower Bound, which describes the lower value, but we can expect in reality an accuracy worst to the one offered by the model (Carter, 1987).

We introduce this value in the peak position measured in the Lander and in the Orbiter as follows:

$$\tau_{LAN} = [t_{OT} + \tau_0 - t_{lR} + \sigma_{\widehat{\tau L}}]mod(t_{code}) + \Delta\tau_{LAN}$$

$$\tau_{ORB} = [t_{lT} + \tau_0 - t_{OR} + \tau_{LAN} + \sigma_{\widehat{\tau O}}]mod(t_{code})$$

3.4. Clock-drift-follow technique (Pong-Pong technique)

One way to improve science is by improving the time delay measurement and by knowing the absolute time and phase reference for all Soundings. One way to do this is by compensating the time errors introduced by the deterministic drift of the clock. This

can be done by characterizing the clocks before travel and also by introducing a modification of the transponder structure normal operation. This modification will allow measuring directly the clock drift between clocks during the mission without altering the electronic design.

The modification implemented in the transponder is the addition of a second Lander-to-Orbiter transmission (Figure 24). If the time between transmissions is sufficiently small to consider that the signal traveled through the same path and that all the parameters such as temperature, position, etc. are fixed, it is possible to say that the difference between the two propagation delays of the two Pong transmissions is coming only from the clock drift. The possible values between transmissions are limited by the relative movement of the two electronics, which is slow, nevertheless, the time is limited to values under 1 second.

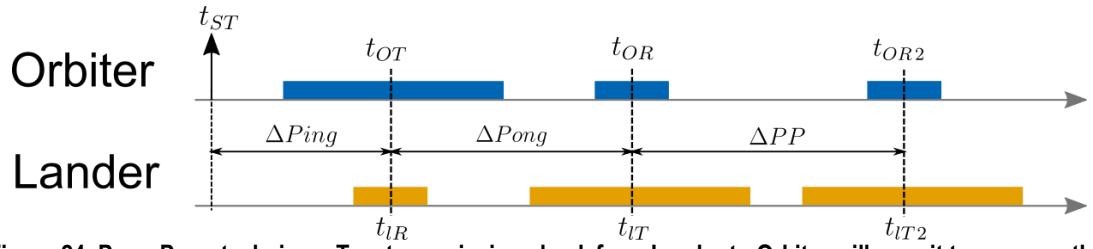

Figure 24. Pong-Pong technique. Two transmissions back from Lander to Orbiter will permit to measure the clock drift between clocks.

The signals received by the Orbiter will be pulse-compressed to find the peak for the two transmissions. The difference between these peaks divided by the time between transmissions is the clock drift between clocks. This measurement can be done on Earth for post-processing compensation, or onboard to be used for calibration purposes.

$$\frac{\Delta f}{f} = \frac{\Delta t}{T} = \frac{\tau_{ORB2} - \tau_{ORB}}{\Delta PP}$$

The last equation shows that when there is clock drift present, an increase in the time between Pong transmissions will also modify the minimum time difference between both propagations. So the accuracy of the measurement will depend directly in the accuracy of the propagation delay measurements of both Pong Transmissions and in the time between transmissions.

System limitations are the sampling frequency, which will limit the accuracy of the peak detection. For Earth, post-processing is possible to improve this accuracy as explained in (Pasquero et al., 2017). In LFR this limitation in the peak detection is reduced because there is less aliasing from the fact that the sampling of the signal is performed at 120 MHz giving 6 points per symbol. Nonetheless, the accuracy of the Pong-Pong measurement of the clock drift depends on the accuracy of the peak position and the time between transmissions.

External factors are the SNR of the received signal that will modify the accuracy of the peak detected. The relative movement between the Lander and Orbiter will limit the time between the two Pong transmissions, limiting the accuracy of the measurement of the clock drift.

There are two values that need to be defined in order to optimize this procedure: the time between Pong transmissions and the number of Pong-Pong transmissions during one Scan. It may be possible that the clock drift will not vary sharply over tens of Soundings, and so it won't be necessary to measure the clock drift each Sounding. Both of these values will be discussed in detail in the next sections and also the accuracy achievable.

Chapter 4. LFR simulation

To understand the impact of the clock drift in the transponder structure operation of LFR, a simulation of the instrument was developed. Because of the existence of different time scales, the simulation of the instrument is divided into two parts: the short-term and the long-term simulation. While we give a brief explanation of the short-term simulator, in this work we will mainly focus on the long-term simulations.

4.1. Short-term LabView simulator

A short-term simulator was already implemented previously in this work. This simulator was developed in Lab View and only simulated a Ping transmission which included models of the analog electronic signal distortion as implemented with filters. The clock drift was also implemented. The interest of this simulator was to directly see the impact in a Ping transmission.

This simulator generates the coded signal first and then modulates the carrier signal with it. The signal is affected by the clock drift, meaning that the code is circular time-shifted. The code is then introduced to several filters that recreate the transmission and reception chains. First, it goes through an amplifier that represents the Power Amplifier in the transmission path and after it is filtered by a band-pass filter that simulates the antenna with a bandwidth from 50 to 70 MHz. Noise is then added to the signal which represents the galactic noise of the medium at the bandwidth of the antennas. Then the signal crosses all of the analog chains of the reception channel. Which are more filters, representing the reception antenna, and a couple of amplifiers and filters to condition the signal.

Before going to the digital domain, the signal is mixed with an 80 MHz signal that takes the carrier to an intermediate frequency of 20 MHz. The signal is then “digitalized” (Note that the simulation is already digital however all the processes prior to the “digitalization” step have a sampling frequency very high to represent the analog world). Subsequently, the coherent accumulation is performed, adding the selected number of codes. Afterward, IQ demodulation is performed and introduced into a matched filter. The highest peak is found, and the propagation delay can be estimated.

This simulator was used to test the effect of phase noise in the signal but unfortunately could not be used for a long-term simulation. Therefore, in this work, a long-term simulator is developed which permits the visualization of the behavior of the transponder structure for long time intervals.

4.2. Long-term simulation

As stated before, the transponder concept reduces the absolute frequency requirements, but it splits them into 4 different time scales. The effect and impact of the clock-drift will be different for each time scale, but the errors will be correlated. The long-term simulator helps to understand these effects and determine in what way the errors are correlated. This information is useful for proposing calibration and compensation techniques for the errors coming from the deviation of the frequency of the clocks.

Using a theoretical clock model, it is possible to introduce the clock-drift into the simulation. The model uses information about temperature, power supply, phase noise and other parameters of interest in the frequency deviation. With the clock model, the simulator generates the time events needed for both electronics for a whole Scan. We will consider the time in the Orbiter as the reference time. For simplicity, it is assumed that the Orbiter clock has no drift and the Lander will include both stability movements added. This means that the worst-case scenario is taken into account.

4.2.1. Assumptions for the simulator

- **Coherent Accumulation is not considered**. The simulator is focused on the long-term effects of the clock drift. It is assumed that this process is performed correctly.

- **SNR is high enough for peak detection.** For each Sounding, the SNR of the received signal is high enough to permit a peak detection without ambiguities. Therefore, for each sounding a peak is detected in both electronics.

- **Frequency is stable during one Sounding**. Therefore the frequency difference is only calculated once for each Sounding. This is valid because the clock drift is driven by the temperature and aging effects which act slowly in time.

- **Propagation delay Constant.** The propagation delay used in the simulation is considered constant for the complete Scan. This to allow that the only movement of the propagation delay is coming from the clock drift.

- **Constant or no delay from electronics.** The simulator does not take into account any delay coming from processing or electronics that have not been mentioned before.

- **The temperature has a linear relation with frequency stability.** For temperature, the model considered shows a linear relationship between frequency stability and temperature. But the model can be improved by characterizing the clocks.

4.2.2. Algorithm

Here we list the steps used for the simulator which is synthesized in the next points for the Nth Sounding:

i. Creation of Orbiter time events (reference time, no clock drift). Recursively use the last time event and add the next delta time to create the second time event.

ii. Calculate the frequency difference between clocks using different proposed functions for temperature, voltage, aging and phase noise. This gives the frequency difference for that specific Sounding.

iii. Create Lander times using the last time of the Lander starting with the time error synchronization and adding the delta time affected by the frequency difference calculated.

iv. Arithmetically introduce the time errors of the sampling error, and SNR and calculate the peak position measured by the Lander.

v. Arithmetically introduce the Lander peak position measured time into the calculation of the Orbiter propagation.

4.3. Results from simulation

For the tests with the simulator, we will use a set of fixed parameters. These parameters are: 5000 Soundings, a Pulse Repetition Interval (PRI) of 5 seconds, a constant propagation delay of 2 time symbols, an accumulation time of 1024 codes, the times $\Delta Ping = \Delta Pong = \Delta PP = 100\ ms$ will be equal, ΔS will be the time needed to make each Sounding of 5 seconds and a sampling frequency of 120 MHz. Unless stated otherwise, we will use these parameters in the following.

The first results from the simulator were used to do cross-validation between the model and the simulator implementation. The first objective was to verify the expected behavior:

a) Peak position measured in the Lander should produce values in the range of 0 to 254 Symbols. This is an effect caused by the measurement modulo the code length.

b) The peak position measured in the Lander is quantized due to the sampling error. The Symbol length is six times the sampling frequency, therefore, the peak detection should show six quantized steps every Symbol.

c) After several Soundings, the produced sampling error should show a uniform distribution over one sampling step.

d) Propagation delay measured in the Orbiter should show a variation of half the sampling step due to the division by two.

This simulation does not take into account the signal nor the smallest time scale (Coherent Accumulation). It is based on time events, therefore, only the time for the two electronics is synthesized and used to calculate the propagation delays.

4.3.1. Accumulated time error

For the first exercise, we use the LFR parameters in the simulator, introduce a constant frequency difference and watch the accumulated time error between both electronics times. This constant frequency difference will make the time difference between Orbiter and Lander drift apart. By introducing a constant value of $\Delta f/f = 1 \times 10^{-9}$ for 5000 Soundings (~7 hours) the expected accumulated time error is of 25μ seconds. Notice that for a constant value of clock drift, the accumulated time error is a straight line (Figure 25).

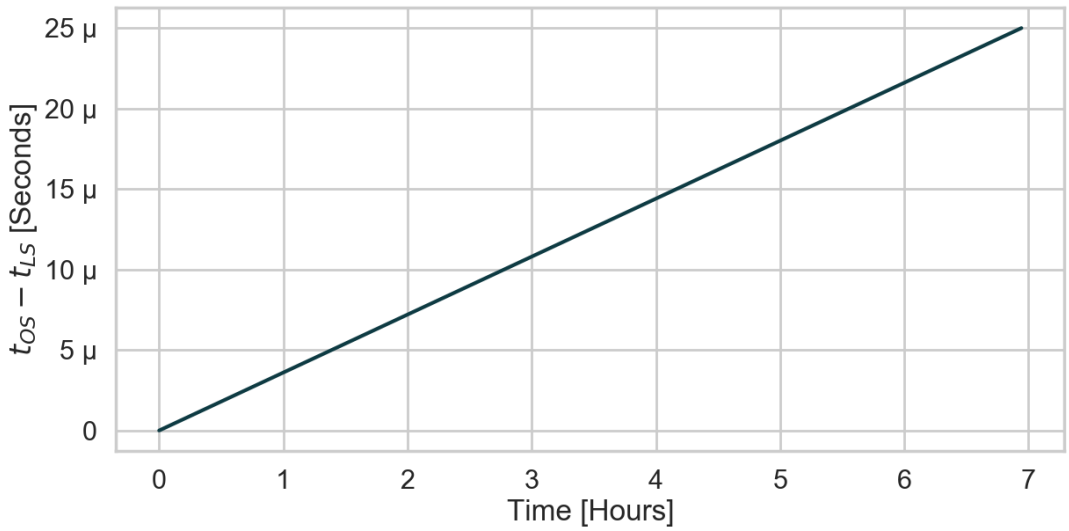

Figure 25. Accumulated time error. Difference between clock drift of Lander and Orbiter start time events, using a constant frequency difference between clocks. A linear response is observed since the frequency difference is constant.

The accumulated time error will show a different curvature depending on the type of frequency drift. In the case of a linear aging effect, the time error shows a quadratic form. Using the same number of Soundings and a clock drift from $\Delta f/f = 0$ to $\Delta f/f = 1 \times 10^{-9}$ for the duration of the 7 hours, the expected accumulated time error is of -1.249×10^{-5} . This value is obtained by the integration of the clock drift over time. Notice that in this case, the accumulated time error exhibits a curvature (Figure 26).

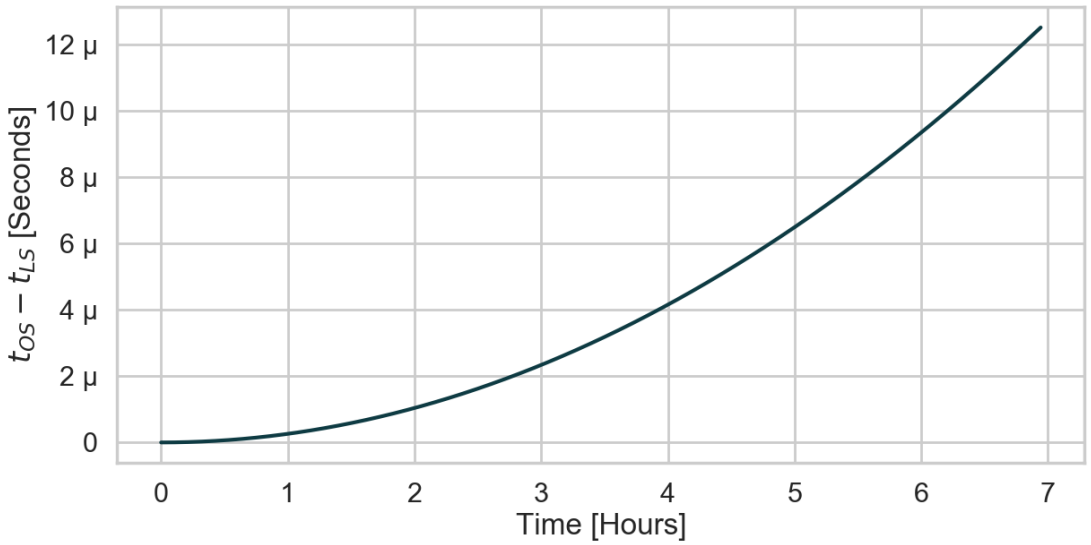

Figure 26. Accumulated time error. Difference between clock drift of Lander and Orbiter start time events, using a time-variant frequency difference between clocks. A quadratic response is observed since the frequency difference varies linearly during time.

4.3.2. Expected behavior of Lander peak detection

In Figure 27 we can appreciate the effects considered in points a), b) and c) for the Lander, described at the beginning of this section. The peak position measured in the Lander must be contained in the range of one code length (0 to 254 symbols). This is a result of the modulo operation with the length of the code. The sampling error limits the possible values at the peak position in the Lander to discrete values, with a minimum step of the sampling time equal to 6 steps per symbol. Figure 27 shows a close-up for the first 0.12 hours of the peak detection measured in the Lander. It is possible to see the 6 steps for each Symbol as indicated by the green dotted line. Because the system is asynchronous and the clock frequency difference is small the distribution of the sampling error should have a uniform distribution over one sampling step after several Soundings.

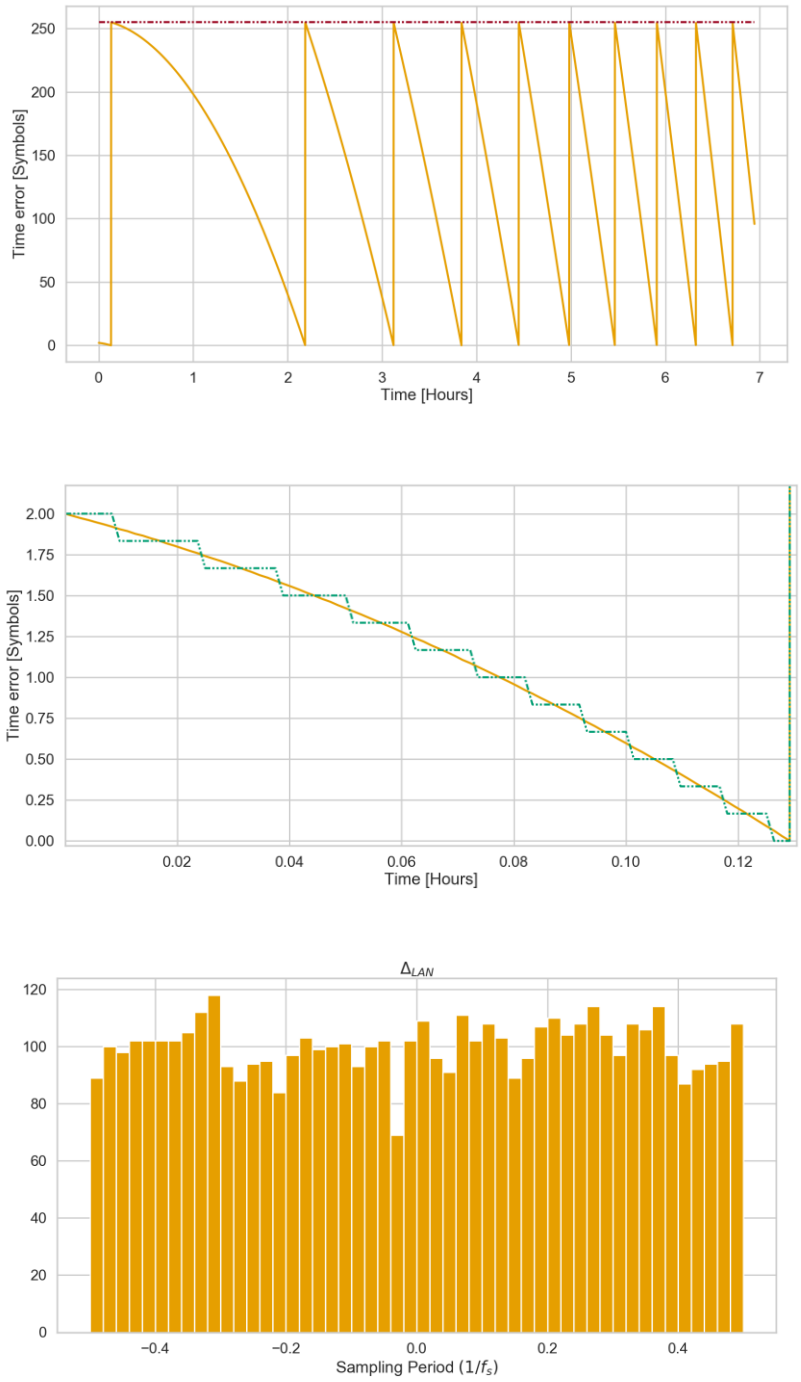

Figure 27. Simulation results for the Lander peak position measurement. Top: A) Peak position measured in the Lander bound to one code time length. Middle: B) Quantized steps in the peak position measured in Lander. Bottom: C) Sampling error shows a uniform distribution over one sampling period after several Soundings.

Comparison between CONSERT and simulator Lander peak position

In this section, we will perform simulations using the CONSERT parameters and compare these results with calibration measurements done for the CONSERT instrument. CONSERT used a carrier frequency of 90 MHz, a sampling frequency of 10 MHz and a symbol time of 100 ns. The calibration measurements were performed on ground before the launch of the spacecraft. For these tests the Orbiter and the Lander were connected with a 15 m coaxial cable. Therefore, the propagation delay is constant ($\tau_0 = cte$). From these calibration measurements we obtain the IQ signals of the Orbiter and Lander, the peak detected in the Orbiter in IQ channels, a complete peak detected signal in the Lander very 10 transmissions and lastly for each transmission 21 points, 10 before and 10 after the peak detected of the Lander. The file used from the calibration measurements is for a long term of time, from 12/04/2001 @ 18H to 13/04/2001 @ 9H11. This test was carried out with a temperature change from -20° to 0° C. And the time between Soundings was of 10 seconds. This gives a total of approximately 5000 Soundings.

Introducing the CONSERT values in the simulator we can compare the Lander peak detections τ_{LAN} distribution against the calibration data of CONSERT of the peak position measured. The distribution we know should be from 0 to 254 symbols of the code. As we explained before in the parameters used in CONSERT we only have a complete peak position detection every 25 Soundings. So we take the same number of peak position data from the simulation. We can see in Figure 28 that both distributions are fairly similar. Both of them covering the complete range of Symbols from the code.

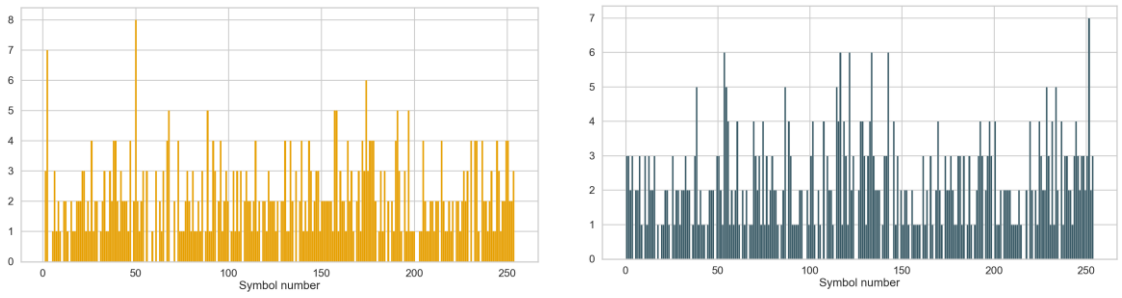

Figure 28. Peak position measured in Lander. Left: distribution of the peak position measured in the Lander τ_{LAN} for the simulator using CONSERT parameters. Right: the peak position measured in the Lander with the calibration data of CONSERT.

4.3.3. Expected behavior of Orbiter propagation delay

From the initial list of expected behaviors, d) speaks of the Orbiter peak position which states that propagation delay measured in the Orbiter will be divided by two to obtain the real propagation delay, we observe that the time model of the LFR for the propagation delay in the Orbiter τ_{ORB} should have the form

$$\tau_{ORB} = 2\tau_0 + \Delta Pong \frac{\Delta f}{f} + \Delta\tau_{LAN}$$

Where $\Delta\tau_{LAN}$ is the sampling error and that it is distributed over one sampling step, so we should expect that the propagation in the Orbiter is bounded over one sampling step variations following the main clock drift variability. For the LFR parameters, the value of the propagation delay is bounded by 0.08 Symbols, as the sampling step is 1/6 Symbols (0.1666) divided by two. In Figure 29 we observe how the sampling error of the Lander gives the range of possible values for τ_{ORB}. In this case we will show here and the next plots the τ_{ORB} divided by 2 which is the propagation delay. For a constant frequency difference between clocks, we expect that the propagation delay is moved by a specific amount of $\frac{\Delta Pong}{2}\frac{\Delta f}{f}$.

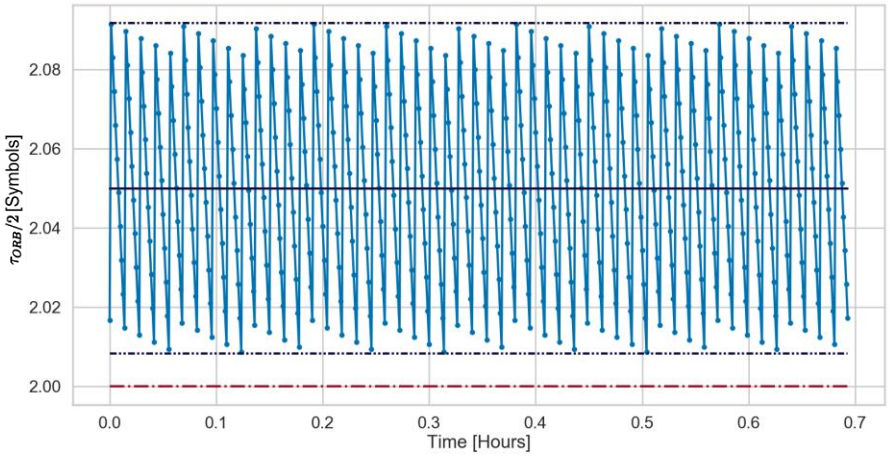

Figure 29. Measured propagation delay. A movement from the true value of 2 Symbols due to the constant clock drift used in the simulation is shown. The red dotted line shows the true propagation delay, the black line shows the calculated error from the time model using the clock drift.

As shown above the possible values of the propagation delay measured in the Orbiter are bounded by the sampling error, if we convert this propagation time to the

phase of the carrier signal, the range of values possible for the Propagation delay in the Orbiter spans almost ¼ of cycle of the 60 MHz carrier signal (see Figure 30). This is because the sampling frequency is 120MHz (two times the carrier frequency) which is then divided by 2 during the propagation delay calculation. To obtain the phase from the arrival time is just needed to apply the modulo operator of the period of the 60 MHz signal to the Orbiter propagation delay measured.

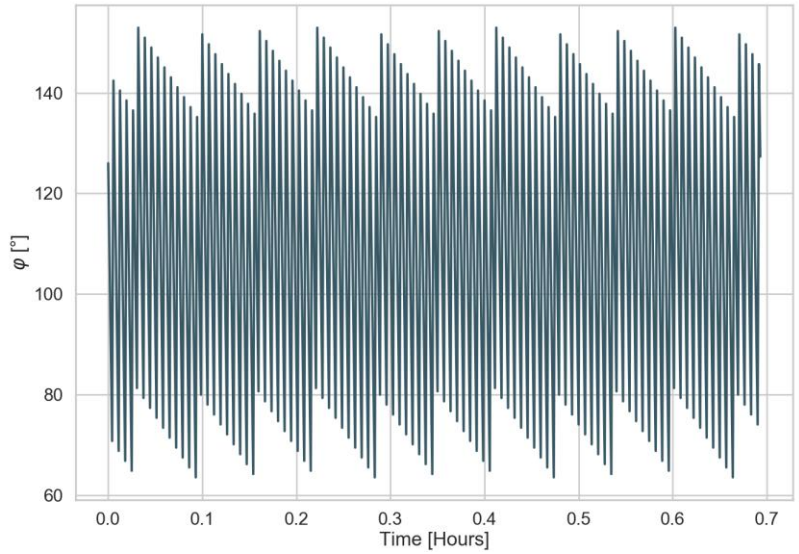

Figure 30. Propagation delay in terms of phase. The propagation delay measurement can be expressed as a phase of the 60 MHz carrier using the modulo operator.

4.3.4. Clock characteristics effects

Now we will look at the effects on the measurement of the propagation delay for each type of frequency drift characteristic in more detail.

Initial frequency offset

This clock error will be represented by a linear change in phase and will directly affect the propagation delay measurement by a constant value, making it easy to spot and compensate for. From

$$\tau_{ORB} = 2\tau_0 + \Delta Pong\frac{\Delta f}{f}$$

We see that the real propagation delay will be changed by a factor of $\frac{\Delta Pong}{2}\frac{\Delta f}{f}$. If the clock drift is constant the error in the measured propagation delay will also be constant and proportional to the time between reception and transmission in the Lander divided by 2. To verify the simulation, we can propose a change in the propagation delay measured in the Orbiter and calculate the clock drift needed to produce such change. In Figure 29 we can see that the true propagation delay is 2 Symbols — but due to the constant clock drift, the value is shifted by 0.1 Symbols. The distribution around these 2.1 Symbols comes from the sampling error in the Lander. This means that a constant frequency offset in the frequency of the clocks will introduce a constant movement in the expected propagation delay as well as a linear phase change that we can see in the straight line measured in the propagation delay.

Aging

The aging effect can be modeled as a linear or logarithmic effect, depending on the time scale used. The aging makes the propagation delay measured in the Orbiter to follow the same function as the clock drift (see Figure 31), making the propagation delay vary over time, even though the real propagation delay is constant. The values used for the model are the ones provided by Rakon for their clocks.

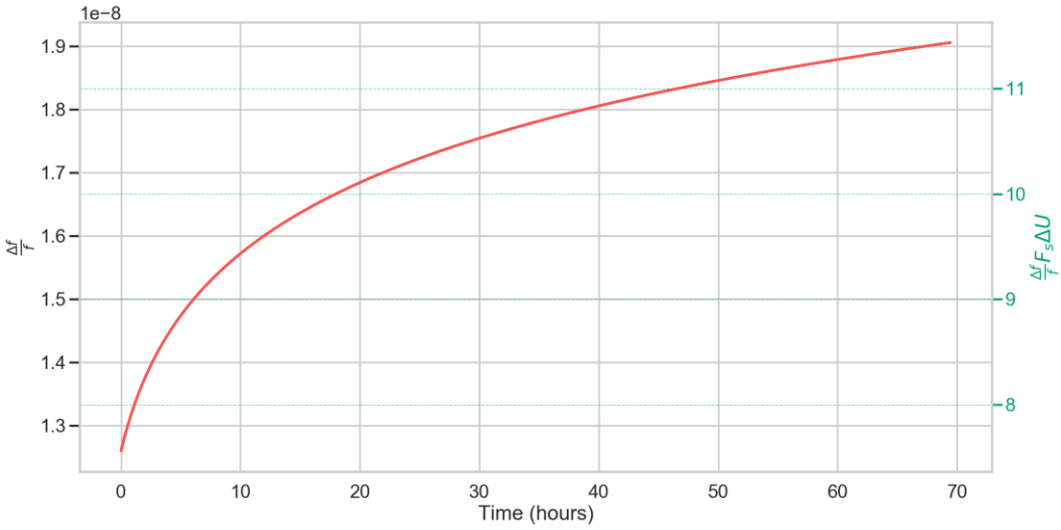

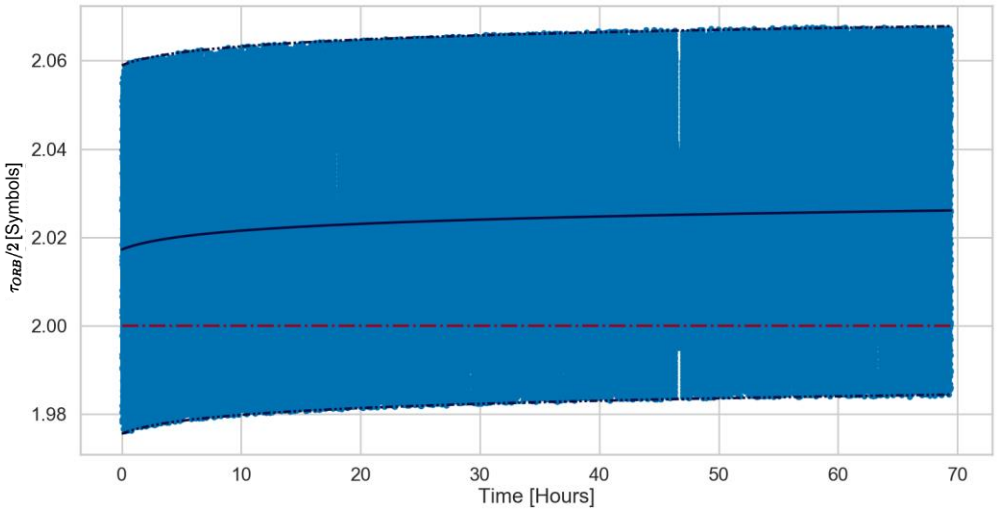

Figure 31. Aging effect on the propagation delay measurement. The logarithmic aging model for 70 hours, shows that the propagation delay measured follows the same function as the clock drift and the sampling error around the expected value with a range of 0.08 Symbols. The red line represents the true propagation delay value, the black solid line represents the expected propagation delay due to the clock drift, and the black dotted lines show the range of values caused by the sampling error.

Temperature

Temperature is a slow-changing effect, and we are interested in the temperature difference between both electronics. The temperature changes are expected to be cyclical during one asteroid day, having direct sunlight and shadow at the surface every several hours. In Figure 32 we show the expected temperature for the electronic box in the Lander (from the DLR technical temperature analysis for the Lander), considering that the Orbiter will remain at a fixed temperature close to 20° C., in this case, the temperature of the Orbiter is not relevant, as the interesting point is the dynamic movement, and a different temperature of the Orbiter will only introduce a different constant value in the function, which yields a frequency offset value. The temperature of the Orbiter solely becomes interesting if the temperature difference between both electronics reaches 100°C. In this case for both selected clocks (Rakon, Syrlinks) will drive the transponder out of the absolute frequency requirements. In this case, we use a sinusoidal function to represent the temperature of the Lander, which is very close to the actual expected temperature. Notice that in Figure 32 the time simulated is bigger than the temperature function so we just repeat the same function for bigger times.

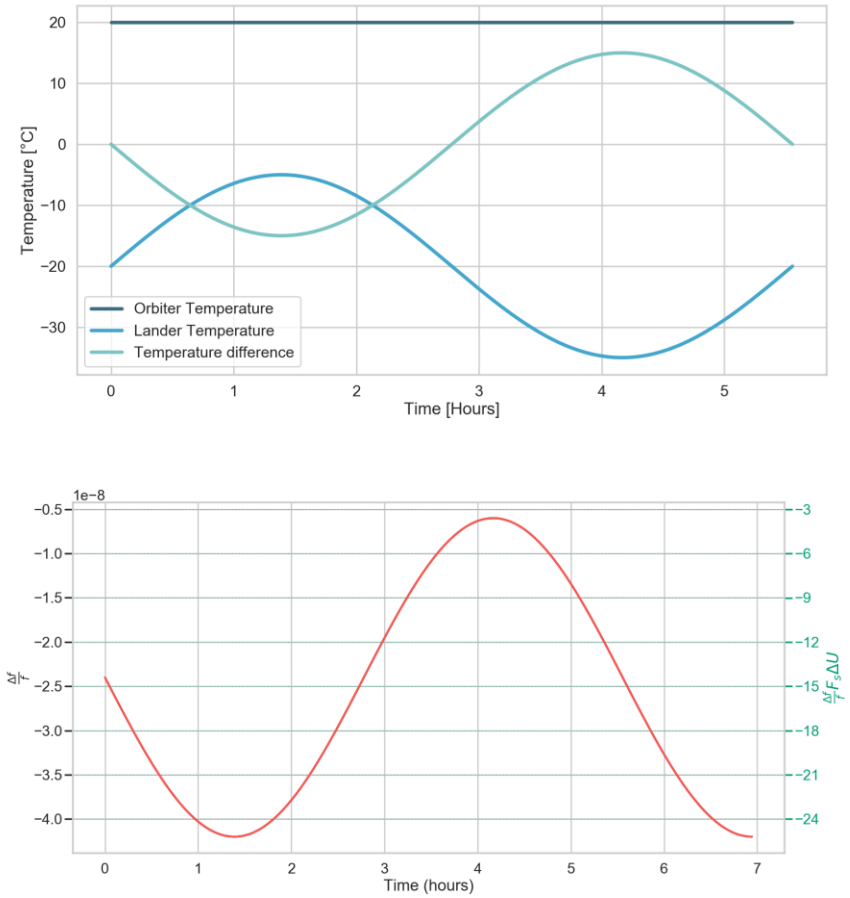

Figure 32. Temperature conversion to the frequency difference. Top: varying temperature for the Lander, constant temperature for the Orbiter and the difference between these two. Bottom: the conversion of the temperature difference to frequency difference using a linear model.

The propagation delay measured by the Orbiter shows a movement of the from the true propagation delay (red dotted line) by an offset produced by the root mean square value part of the frequency stability function (see Figure 33); it also shows that it follows of the temperature behavior. The black line represents the error $\frac{\Delta Pong}{2}\frac{\Delta f}{f}$ using the stability frequency from temperature, and the external dotted black lines are moved 0.04 symbols up and down to show the limit of the variation coming from the sampling error.

By using only the temperature expected in the Lander scenario in the simulation, it shows that temperature could have little impact on the design — but still, if we are able to measure the clock drift with accuracy, it can be compensated. Furthermore, the measurement is bounded by 0.08 Symbols coming from the sampling error of the

reception in the Lander. As we have seen the processes that affect the frequency stability will have a direct impact on the propagation delay measurement.

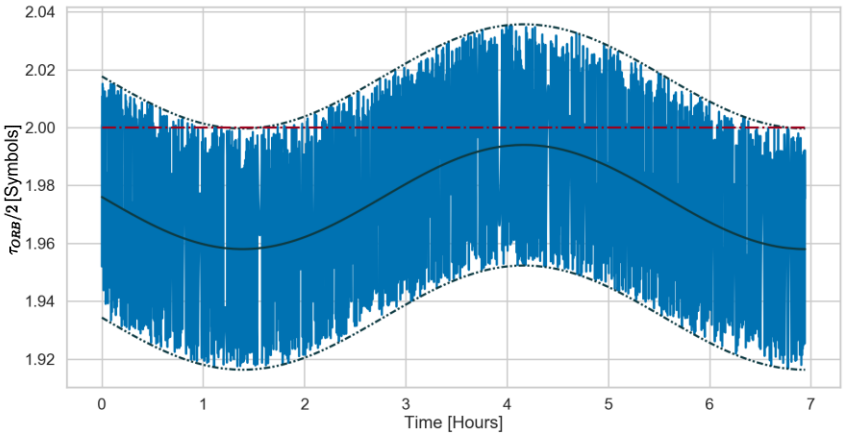

Figure 33. Temperature effect on propagation delay measurement. The propagation delay shows the same function as the temperature. In red the true propagation delay, in solid black the expected propagation delay calculated with the frequency difference. The black dotted lines show the effect of the sampling error.

4.3.5. Phase rotation effect

In Figure 34 we see a close-up of the Orbiter propagation delay for the linear aging effect, and we can notice a strange effect. The Orbiter propagation delay follows a direction and exhibits a jump when reaching the boundaries of the sampling error but at some point (i.e. ~4.6 Hours) it changes direction, as we can see by the small parabola in the plot of the propagation delay in the Orbiter (Figure 34).

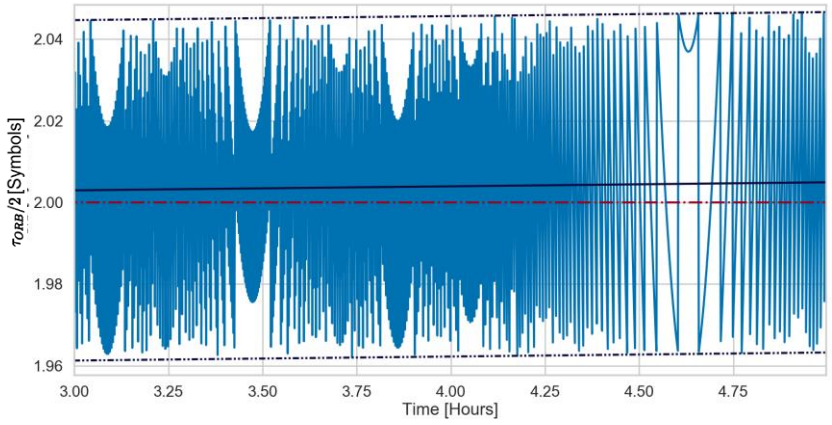

Figure 34. Zoom to the propagation delay measured for the linear aging case.

This effect seen at approximately 4.6 Hours in Figure 34, is that the propagation delay measured is decreasing before 4.6 hours but near to the 4.6 hours it starts to reduce the speed of change until it reaches a point where the value doesn't change and after 4.6 hours the propagation delay changes direction with an increasing value. This means that there is a stroboscopic effect between the frequency drift, the sampling frequency and the time between Soundings. This effect can be explained by the frequency stability definition:

$$\frac{\Delta f}{f} = \frac{\Delta T}{T}$$

Where Δf is the difference between frequencies in the clocks, f is the frequency of the reference clock, ΔT is the change in time in seconds and T is the time-lapse during which this phase or time difference is taking place. From Figure 34 we notice that approaching 4.6 hours the values of the propagation delay each Sounding is a multiple of the sampling period (nT_s) because the values are very close to each other. This means that the time difference ΔT from one sounding to another is equal to a multiple of the sampling frequency nT_s, leading to the boundaries of the measurement. T is equal to the time between Soundings (ΔU). Using the definition of frequency stability:

$$\frac{\Delta T}{T} = \frac{nT_s}{\Delta U}$$

Where n is an integer number, T_s is the sampling period and ΔU is the time between Soundings. For the extreme case $\Delta f / f = 0$, we expect the propagation delay measured in the Orbiter τ_{ORB} to be a straight line. Moreover, we can expect this effect if the clock drift is constant and a multiple of the sampling frequency and time between Soundings.

If we rearrange the equations we arrive to:

$$n = \frac{\Delta f}{f} \Delta U F_s$$

This means that if we multiply the clock drift by the time between Soundings and the Sampling Frequency, we will find the points where this "direction change" effect

happens and it is when this new value is crossing an integer number (see the green y-axis on the right in Figure 35).

This effect is altered by neither the Symbol time nor the signal bandwidth, nor by the used propagation delay. Notice in Figure 35 how every time this new quantity $\frac{\Delta f}{f}\Delta U F_s$ (the green y-axis on the right) crosses an integer value, a change of direction can be observed in the propagation delay τ_{ORB}.

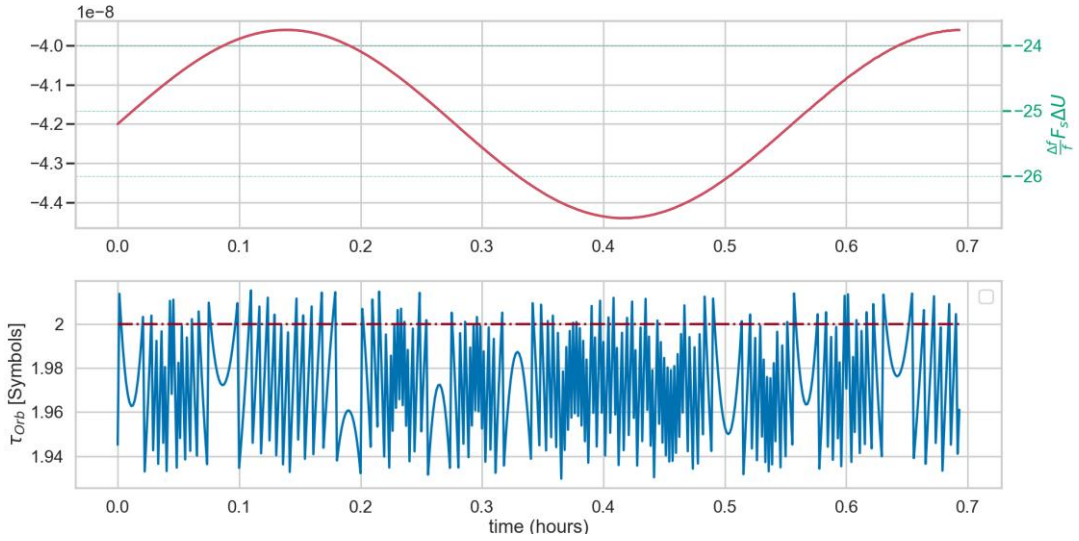

Figure 35. Phase rotation effect. Top: In the left y-axis shows the clock difference used and in the right y-axis in green shows, the same frequency difference multiplied by the sampling frequency and the time between Soundings. Bottom: The propagation delay measured in the Orbiter shows the rotation effect every time the top plot crosses a unit value in the right y-axis.

Phase rotation effect comparison between CONSERT calibration data and Simulator

In terms of phase, the effect mention in the last section could be recognized as a phase rotation. Every Sounding the phase received changes and generates a rotation effect. In CONSERT data a similar effect was observed. By using the IQ pulse compressed signals it is possible to obtain the phase of the received signal.

$$\varphi_{ORB} = arctan\left(\frac{Q_{peak}}{I_{peak}}\right)$$

In Figure 36 we can see the phase obtained from the IQ compressed signals. At ~0.5 hours a similar effect is observed.

Using the values of the CONSERT calibration test in the simulator we obtain similar results for the phase of the peak detection (Figure 37). Recognizing this similar behavior in the ground calibration data and in the simulator results, let us validate the model and simulator implementation.

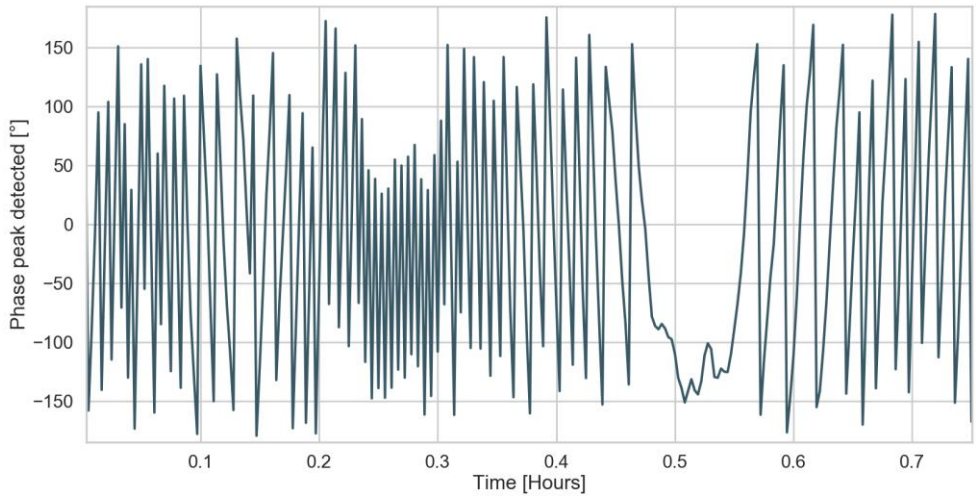

Figure 36. The phase of the peak detection calculated with the IQ data of the compressed signal. This data shows the same behavior of direction change as shown in the simulator.

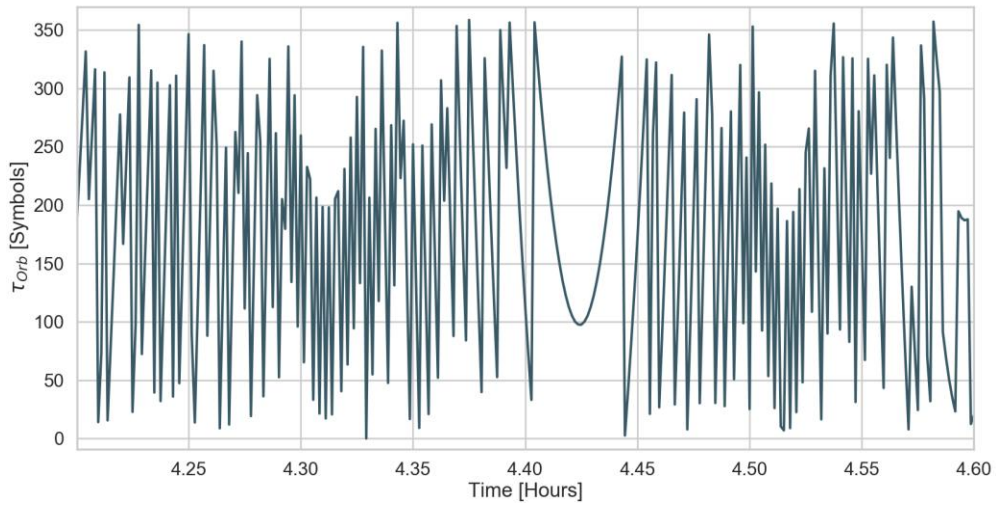

Figure 37. The phase of the peak detection in the simulator, using the values of the CONSERT system and calibration test.

4.3.6. LFR specifications

With the simulator, it is furthermore possible to demonstrate the LFR specifications to show that by selecting a specific frequency difference the simulator generates the correct time error. We can take the values calculated for the clock frequency stability for each time scale and review the phase and time errors produced in each time scale. As we have noted the simulator does not consider the coherent accumulation, therefore, we will not present this time scale in the next analysis.

Ping to Pong

The Ping to Pong requirement limits the clock frequency difference to $\frac{\Delta f}{f} = 2.5 \times 10^{-8}$. This means a time error of one-twentieth of the time symbol in 100 milliseconds, which is a typical duration between reception and transmission. If we introduce a clock drift of 2.5×10^{-8} to the simulator, we expect that the difference between reception and transmission times in the Lander is 1/20 of the time of a symbol. The test of Figure 39 was performed using a frequency difference that varies from $2 \times 10^{-8}\ to\ 3 \times 10^{-8}$. We can see that the time difference between reception and transmission in the Lander is changing (the ripple with very low amplitude, at the top right is coming from a precision effect). This test permits us to see the time error at exactly 2.5×10^{-8} in the middle of the time of the test. From the time model we can calculate that the expected change in the peak position measured in the Orbiter is exactly 2.025 at 7.5 hours. In Figure 39 we show in blue the peak position measured in the Orbiter, and in black is the error in the peak position calculated from the clock drift and the time model.

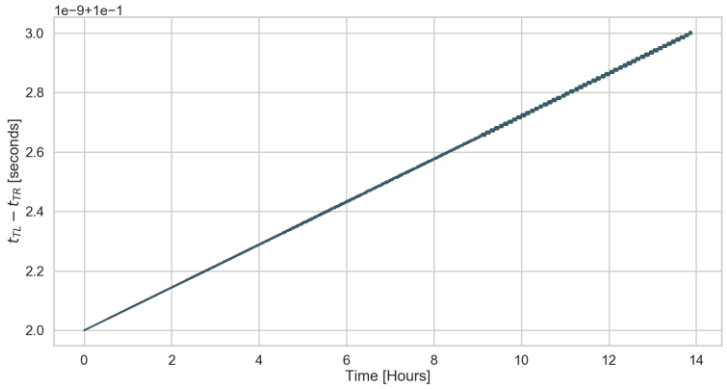

Figure 38. Time difference between Lander Transmission and Lander reception time events.

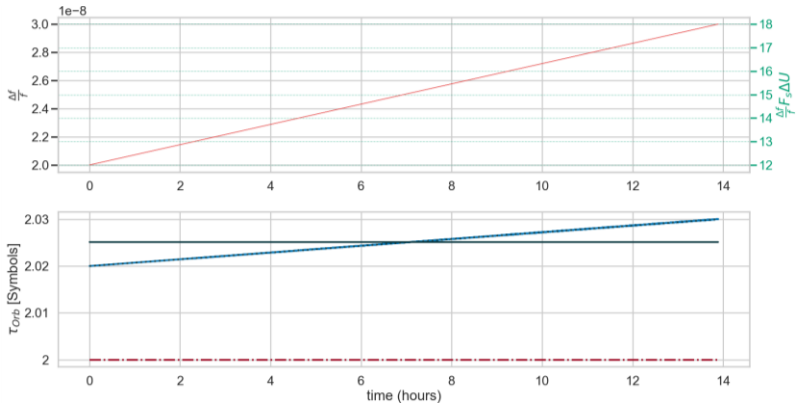

Figure 39. Top: Clock drift used for the test. Bottom: In Blue the propagation delay measured in the Orbiter, in black the expected propagation delay for $\frac{\Delta f}{f} = \mathbf{2.5 \times 10^{-8}}$, In red the true propagation delay ($\mathbf{2\ Symbols}$).

Sounding to Sounding time reference

The time scale from Sounding to Sounding has two different specifications in regard to the reference. First, we will review the time between Soundings. From specifications to be able to compensate a miss-detection of the peak, the time error between Sounding to Sounding should be less than one sampling step (8.33 ns) during 10 minutes of Soundings which means $\Delta f/f = 2.5 \times 10^{-8}$. This means that the difference of the Starting time of the Lander in Orbiter reference with respect to the Orbiter starting time in Orbiter reference is less than 8.33 ns. Thus, by differentiating the Orbiter and Lander times after 10 minutes we notice the 8.33 ns error, as specified in the LFR specifications for this timescale and time reference (Figure 40).

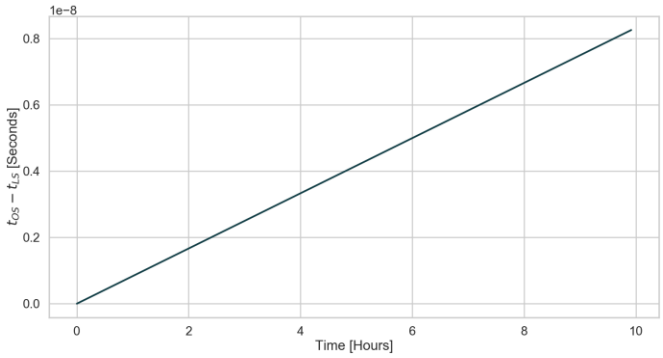

Figure 40. Accumulated time error between Lander and Orbiter for each Sounding. After 10 minutes the time error is of 8.33 ns, as specified in LFR specifications.

Sounding to Sounding phase reference

For the Sounding to Sounding phase we expect that the phase of the signal does not change more than 3 ns which translates to 60° of the carrier signal within the first hour. In this case, we can model the phase for the deterministic part of the model. Furthermore, we can obtain the same graph as for the last time scale to verify the time error of 3 ns after 1 hour ($\Delta f/f = 8.33 \times 10^{-13}$) (Figure 41).

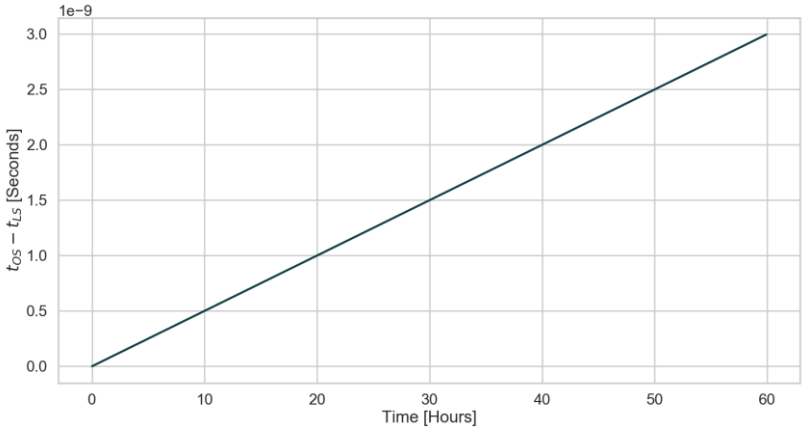

Figure 41. Accumulated time error between Lander and Orbiter for each Sounding. After 1 hour the time error is 3 ns, as specified in LFR specifications.

Tx-Rx windows

As said before the Reception window of one electronic should always be within a transmission window of the other electronic. This will permit to have communication between them and therefore science return. The clock drift will cause a calendar to drift in the windows between Orbiter and Lander. The characterization of the possible time error coming from the clocks will be applied directly in the improvement of the selection of duration of Tx window reducing the margins needed to allow the movement of the reception window inside the transmission one. This means the optimization of the power consumption and time needed for each Sounding in terms of transmission. After 12 hours the Reception window should not move more than 10 ms ($\Delta f/f = 1.388 \times 10^{-11}$) (Figure 42).

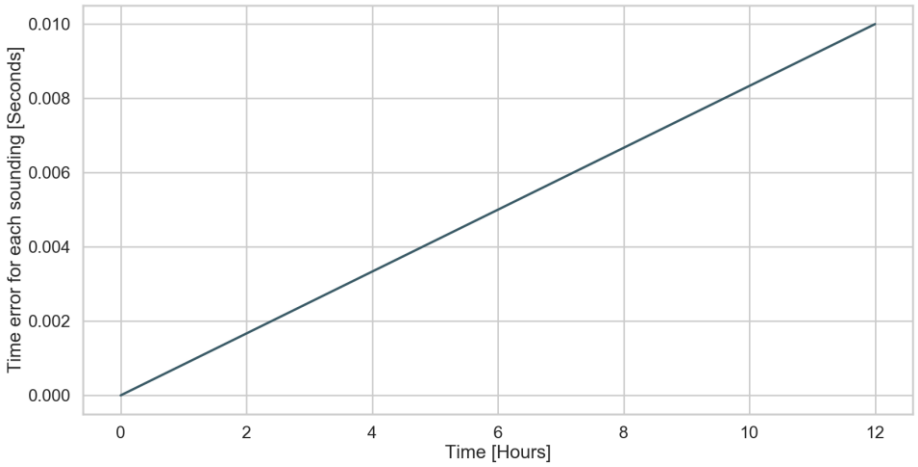

Figure 42. Accumulated time error between Lander and Orbiter for each Sounding. After 12 hours the time error is of 10 ms, as specified in LFR specifications.

Chapter 5. Real clock measurement

5.1. Test bench design

This chapter explains the conception and development of the test bench used to measure phase and the accumulated time error between two clocks. The data from this experiment will be used to validate the models used in the simulator explained in Chapter 4.

The main goal is to use the data from the test bench in the long-term simulator to observe the effect of the drift of a real clock over the measurement of propagation delay. For this, it is necessary to know the phase and time error between both clocks for long time periods. The phase accuracy should be sufficient to observe effects over the 60MHz carrier cycle and should be able to measure the time error between clocks for at least 12 hrs.

The test bench was developed with some design constraints in mind — limited cost, quick assembly, and direct data delivery — and was assembled with the help of the electronic laboratory of IPAG.

5.1.1. Requirements

The accuracy expected for the measurement is less than 10 degrees of the 60 MHz carrier signal. With this accuracy is possible to observe changes at the phase carrier level. This will be useful to verify compensation methods for the absolute phase in the mission, like those in the time and phase Sounding to Sounding frequency stability requirements mentioned before.

The time between acquisitions of the time difference between clocks should be at least the same as the shortest time between two time events, or if possible shorter. This allows for the knowledge of the phase between time events. For example, the time between Ping and Pong is approximately 100 ms. Therefore, it is necessary to measure the time difference between clocks at least every 100 ms.

The desired data output is done through serial communication via USB to a computer.

5.1.2. Time and phase measurement techniques

Different phase and time measurement techniques were explored to find the best option for the test bench. The options analyzed for this project were selected according to the needs of the simulator, in this case, to measure phase difference and accumulated time error between the clocks. Measuring time error and not frequency stability was preferred due to the fact that the simulator works with time events. Furthermore, it is easier to adapt the data directly to the simulator in this way. The building constraints, such as limited cost, quick assembly, and easy data delivery, were also considered. With this in mind, we came up with different measurement methods.

Most clocks that are available for this project are 10 MHz clocks, so we will consider a nominal frequency of 10 MHz for all the test bench techniques analysis.

ADC

The first option we studied was an ADC and two clocks (Figure 43). One clock was used as the sampling signal of the ADC and the other as the input. This means one digital clock and another sinusoidal clock, which leads to a beat signal at the output of the ADC with a frequency equal to the difference between both original clocks. This method was fast to implement using an ADC test board, and only two clocks.

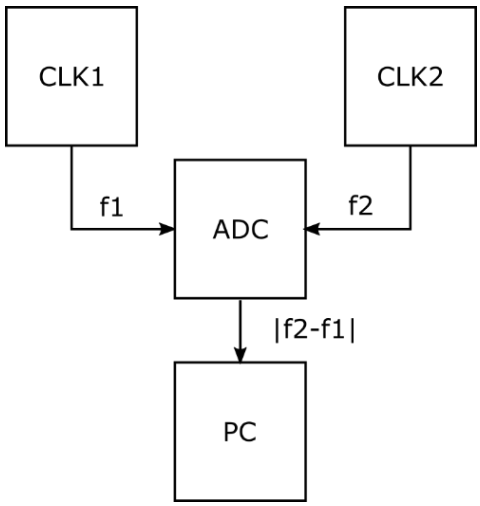

Figure 43. ADC technique to measure time error between two clocks.

In this method, we can express one of our signals as a cosine signal

$$x(t) = \cos(\omega_1 t)$$

While the other can be expressed as an impulse train as it will be used to sample the other signal

$$p(t) = \sum_{n=-\infty}^{\infty} \delta(t - nT_2)$$

Where $T_2 = 2\pi/\omega_2$ and where ω_2 is slightly different than $\omega_1$therefore $\omega_2 = \omega_1 + \Delta\omega$.

So at the output of the ADC, we have the multiplication of both signals $x_p(t) = x(t)p(t)$. If we calculate the Fourier transform of the output

$$X_p(\omega) = X(\omega) * P(\omega)$$

$$X_p(\omega) = \pi[\delta(\omega - \omega_1) + \delta(\omega + \omega_1)] * \omega_2 \sum_{k=-\infty}^{\infty} \delta(\omega - k\omega_2)$$

$$X_p(\omega) = \pi\omega_2 \left[\sum_{k=-\infty}^{\infty} \delta(\omega - \omega_1 - k\omega_2) + \delta(\omega + \omega_1 - k\omega_2)\right]$$

Only the parts of the components $k = -1$ and $k = 1$ will remain inside the bandwidth of the ADC.

$$X_p(\omega, k = 1) = \pi\omega_2[\delta(\omega - 2\omega_1 - \Delta\omega) + \delta(\omega - \Delta\omega)]$$

$$X_p(\omega, k = -1) = \pi\omega_2[\delta(\omega + 2\omega_1 + \Delta\omega) + \delta(\omega + \Delta\omega)]$$

$$X_p(\omega) = \pi\omega_2[\delta(\omega - \Delta\omega) + \delta(\omega + \Delta\omega)]$$

$$x_p(t) = \omega_2 \cos(\Delta\omega t)$$

So at the output of the ADC, the signal is a beat frequency representing the difference between the two frequencies of the clocks.

In this system configuration, the beat frequency will be very small, making it hard to follow the period in order to know the phase measured. To solve this complication, it is

possible to propose frequency dividers for one or both clocks to achieve a faster beat frequency or to achieve an IQ sampling to obtain the phase directly. This means having at least 4 times the frequency of the sampled clock in the ADC clock, to ensure the IQ configuration has samples that are separated 90° from each other.

It was not possible to find an ADC at 40 MHz, to fulfill the IQ sampling for a 10 MHz clock, and the development board to deliver the data. Therefore the use of dividers for the clocks to reduce the frequency was the next option. Each clock should be divided by a different number to generate a frequency difference between them. This division imposes a restriction: the higher the number to divide, the more accuracy in terms of the amplitude of the ADC is needed to follow the phase changes at the carrier level. For example, if we use a division by 40 of the 10MHz signal we need an ADC with better amplitude accuracy to obtain this phase than if we divide by a smaller number the 10 MHz clock. This is illustrated in Figure 44 where we can see that by dividing by a large number (green-solid line) the ADC needs more amplitude accuracy to solve the accuracy needed than when we divide by a smaller number (blue-dotted line).

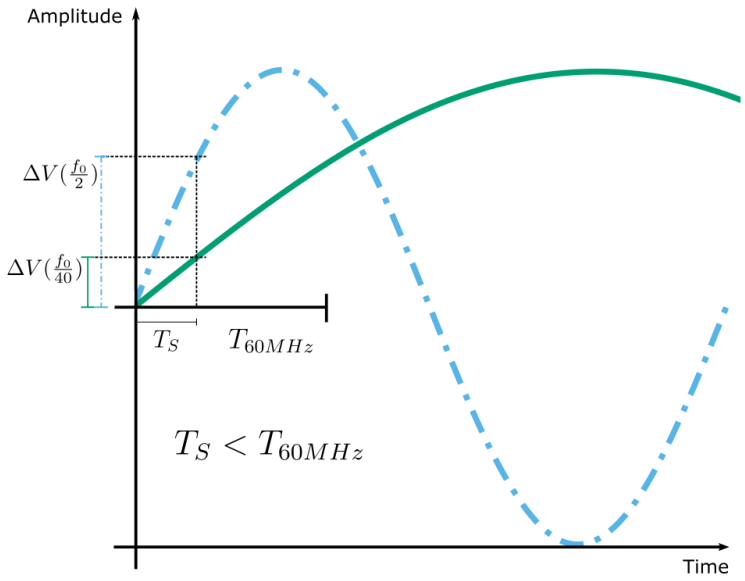

Figure 44. The amplitude accuracy needed to measure changes at below the carrier period is increased by higher divisions. Drawing not to scale.

To verify the system it was simulated using the same clock model as in the simulator. These simulations showed that the accuracy in amplitude required was difficult to obtain using this system. Also, the frequency dividers needed to be of high quality to reduce jitter introduction, increasing the price of the system. Therefore we decided to explore other options.

DMTD

Before the Dual Mixer Time Difference (DMTD) system was proposed we considered two other options: a high-speed acquisition board and a Time Interval Counter (TIC). The acquisition board was rejected due to the high price and the TIC was halted due to the DMTD containing a TIC inside the design.

The DMTD system used is based on the design originally presented in (Allan & Daams, 1975). This system was proposed to characterize very stable clocks by measuring the time difference between two clocks. This system is completely analog, which involves the use of discrete components (see Figure 45). In the European Organization for Nuclear Research (CERN), a fully digital DMTD system (DDMTD) was developed. This modification reduces the electronics needed to only two digital clocks and an FPGA (Moreira, Alvarez, Serrano, & Darwazeh, 2012; Moreira, Alvarez, Serrano, Darwezeh, & Wlostowski, 2010).

One interesting point of the DMTD system is the ability to measure time fluctuations. This is an advantage due to the fact that we can convert these time fluctuations into frequency fluctuations if needed in order to know the clock stability directly. It also responds to the measurement needs of phase and time error accumulation used in the simulator developed.

5.2. DMTD analysis

The operation principle of the system is to shift the phase difference from a high-frequency domain to a low-frequency domain. Figure 45 shows the block diagram of the original analog DMTD. CLK 1 will be considered the reference clock and CLK 2 the device under test (DUT). A third clock, called common clock, with a frequency close to that of the other two clocks is used to mix both clocks to generate slower beat frequencies with a frequency equal to the difference between the frequencies of CLK 1

with common clock and CLK 2 with common clock, like and stroboscopic effect. These two beat signals have a time difference proportional to the time difference between CLK 1 and CLK 2. A Time Interval Counter is used to measure the time difference between these beat signals (using the rising edges as the start and stop times) — but what is really measured is the time difference between the original clocks, but with resolution amplified by a factor of the ratio of the carrier frequency to the beat frequency.

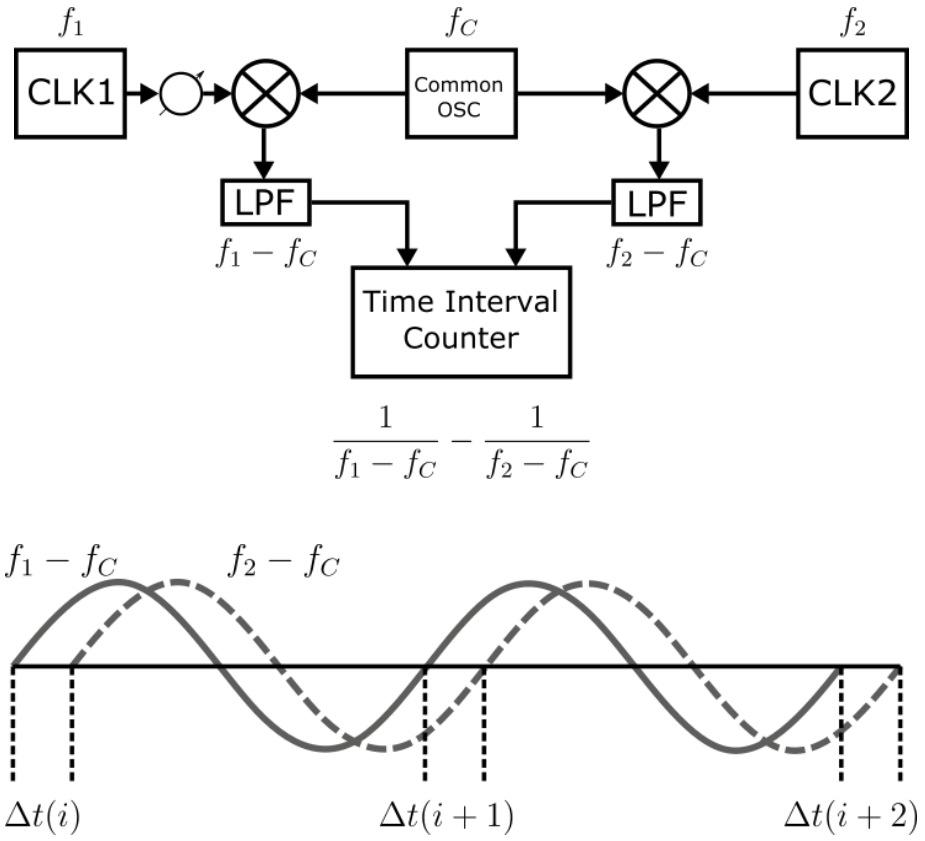

Figure 45. DMTD block diagram presented in (Allan & Daams, 1975) and time diagram showing the time difference measured between beat signals.

(Moreira et al., 2010) proposed a fully digital version of the DMTD. The system is the same but all the electronics are substituted by digital versions inside an FPGA (Figure 46). Both clocks are digital and are connected to D flip flops. A D flip flop has two inputs, one named D where we introduce a logic signal and one clock input. The flip flop will read the input value every rising edge of the clock signal and show it at the output until a next rising edge of the clock is detected and the new logic input value is read.

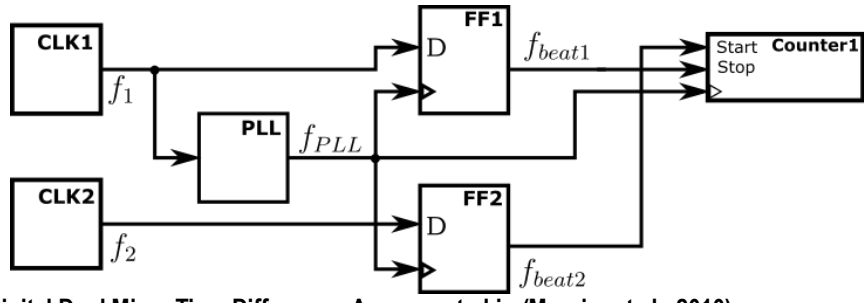

Figure 46. Digital Dual Mixer Time Difference. As presented in (Moreira et al., 2010)

CLK 1 is used as the reference for a PLL, internal or external to the FPGA, to synthesize the common clock signal with a frequency close to those of the original clocks (i.e. 1 kHz difference between the 10 MHz CLK 1 and the output of the PLL). This synthesized signal will be used as the driver clock of the two D Flip Flops. Therefore the Flip Flops will act as a mixer, but as a result of the digital nature of the system, there is no need for filters at the output. These two new beat frequencies have a time difference proportional to the time difference between the original clocks. With a counter or a rising edge tagged time it is possible to measure the time difference between beat signals (Figure 47).

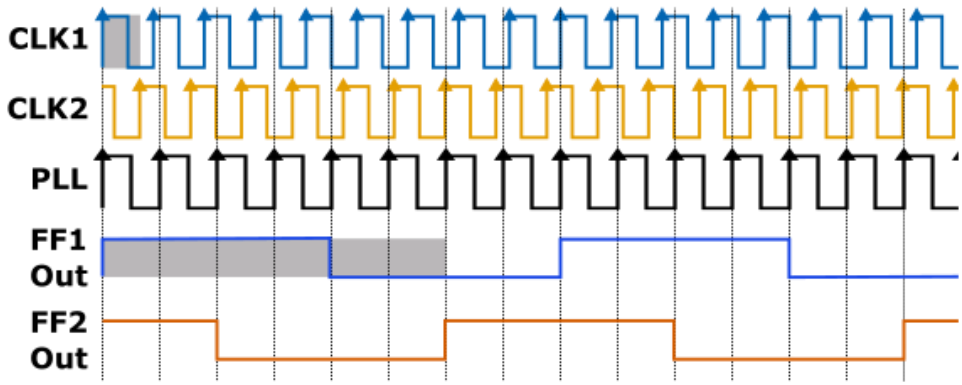

Figure 47. The time diagram shows how the DDMTD generates the "zooming" effect in the time difference between the original clocks. The beat frequency and the original frequency in this drawing are not at the correct scale. We expect that the beat frequency is ten thousand times smaller than the original clock frequency.

In Figure 47 we can observe how if the initial time difference between both clocks (light blue and light orange) is ¾ of a cycle, the beat signals (dark blue and dark orange) have also ¾ of a cycle of time difference. Thus, measuring this time difference between the beat signals signifies to measure the original time difference but amplified by the ratio of the beat frequency to the original clock frequency. The time difference between the original clocks is expressed as follows:

$$x(i) = \frac{\Delta t(i) f_{beat1}}{f_{CLK1}}$$

Where $\Delta t(i)$ is the *ith* time difference measured by the time interval counter in seconds, f_{CLK1} is the frequency of the oscillator reference and f_{beat1} is the beat frequency which is the difference between the clock reference and the PLL output frequencies, and where the ratio of f_{beat1}/f_{CLK1} is the zooming effect done by the DMTD. As shown in Figure 47 the original time difference of the clocks is too small on time for a Time Interval Counter to give a good resolution without using another stable high-frequency clock. However, by using the DDMTD technique the output of the Flip Flops of the beat signals allow this original time difference can be measured with a better resolution using the same TIC. From this measurement, it is possible to obtain the fractional frequency as the difference of the actual time difference to the last measurement over the time between measurements.

$$y(i, \tau) = \frac{x(i+1) - x(i)}{\tau_{beat1}} = (\Delta t(i+1) - \Delta t(i)) \frac{{f_{beat1}}^2}{f_{CLK1}}$$

Where $f_{beat1} = 1/\tau_{beat1}$ and τ_{beat1} is the time between both measurements which in our case is equal to the period of the clock 1 beat signal. The resolution or the minimum time difference (Δt_{DMTD}) achievable with this design is expressed as:

$$\Delta t_{DMTD} = \frac{f_{beat1}}{f_{PLL} \cdot f_{CLK1}}$$

Where f_{PLL} is the output frequency of the PLL used as the clock input of the Counter. This means that the clock used by the counter is the smallest possible time difference step measured by the test bench and that it will be amplified by the zooming effect of the DMTD. For example, if the original clocks are 10 MHz and the PLL synthesize a 9.999 MHz, 1 kHz below the clock frequency, the minimum time difference that the test bench can measure is $\sim 1 \times 10^{-11}$ seconds. This means that the zooming factor is of 10000. This system is limited in accuracy by the noise generated by the PLL and FPGA board.

The time diagram in Figure 47 shows the “zoom” effect on the phase measurement between the original clocks. The smaller the beat frequency, the better the time difference can be measured since we have more clock counts for this measurement

— but lower beat frequencies mean that the time between time difference measurements are larger, meaning that to obtain a time difference measurement we need to wait a longer time. Therefore, there is a trade-off between the time between available measurements and the resolution of the system.

5.3. Implementation of DMTD

The Test Bench implementation was originally planned to be totally digital and enclosed in the FPGA board. First tests showed that the accuracy for short times (< 1 s) could be improved using an Ultra-Low-Jitter external PLL. Therefore, we will present both techniques as well as their advantages and disadvantages in the following.

The implementation was performed on an FPGA board with two digital clocks, and two options for the PLL: the internal PLL provided in the FPGA or an external Ultra-Low Jitter board.

The test bench electronic boards, for the clocks and to interface with the FPGA, and as well the FPGA VHDL description was done by the electronics lab at the IPAG.

N.B. During the first tests with the bench, we realized that the design could be improved in hardware and digital design. We decided to pursue this new improved version, however, the execution of these improvements exceeded the time frame of this work. Therefore, we will only show the results and conclusions of the first version of the test bench leaving the results of the second version, for a future article.

5.3.1. Hardware Board

The FPGA board used was a XILINX Virtex Cyclon 5 Figure 48. It was able to receive the two clock inputs and had the option of using the internal or external PLL signal as the common clock. The evaluation board used a serial channel to send the data to the computer via a USB port.

The FPGA provided an Inter-Integrated Circuit (I^2C) communication protocol bus to read several sensors like temperature, voltage, and current. This helps with the characterization of the clocks and the improvement of the compensation techniques.

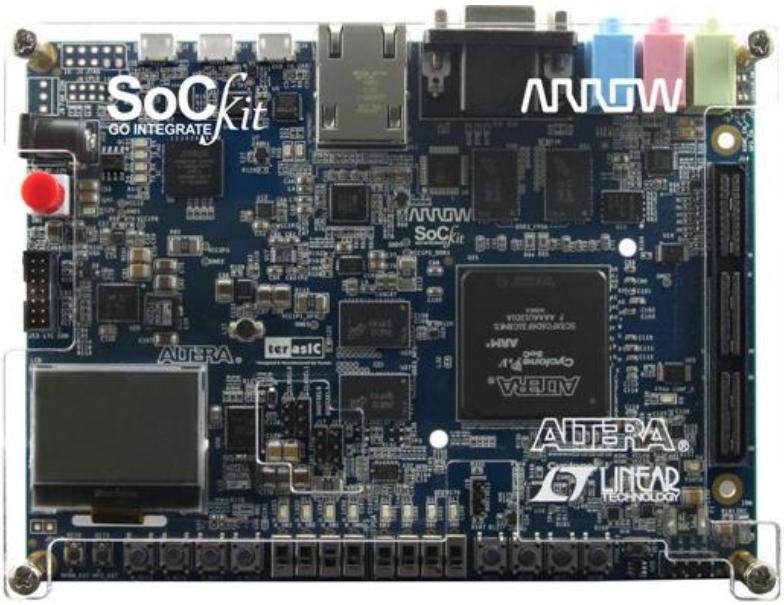

Figure 48. Development board for the FPGA. Sockit from Arrow, with a Cyclon V FPGA.

The sensor used is the MCP9804, with a resolution of 0.5°C and the possibility to measure from -40°C to 125°C. This sensor communicates with the FPGA board via I²C channel and will help characterize the frequency drift against temperature. Every clock box contains a temperature sensor, this means that we can measure independently the temperature of both clocks.

A pair of clocks of each brand (Syrlinks and Rakon) were purchased for the experiment with the test bench. In Table 8 we have a more complete table than the one presented in Clock Introduction. All values are taken from the datasheet provided by the manufacturer.

Table 8. Rakon and Syrlinks clocks characteristics.

	Rakon	Syrlinks
NAME	RK 408	EWOS 0830
F(MHz)	10	10
Freq init (ppb)	±100	-
Allan Variance for 1 sec	5E-12	4.1E-11
LongTerm Stability		
per day (ppb)	-	±0.5
per year (ppb)	100	±100
over life (ppb)	300	
Temp stability (ppb)	±60	±20

Temp range (°C)		-40 to 75		-30 to 70
Voltage stability (ppb) 5%		±1		4
V supply (V)		5		7
Phase noise (dBc/Hz)	1Hz	-100	1Hz	-
	10Hz	-130	10Hz	-125
	100Hz	-150	100Hz	-135
	1kHz	-160	1kHz	-145
	10kHz	-165	10kHz	-
Warm Up (W)		5		2.8
Power (W)		3		1.12
Mass (g)		70		15
Dimensions (mm)		40x50x20		<10cm^3
Signal		Sine		Sine/HCMOS
Price Flight Mode €		l 16.5k + 6.6k tests		2.5k+2.5k screening
Price Engineering Mode €		8.5k		1.8k

These two models were selected by a trade-off between the principal characteristics of low price, low power consumption and small size and weight. Both clocks show similar stability characteristics, like the frequency stability deviation due to aging, temperature and voltage supply, which are in the same orders of magnitude between each other, but Rakon clock shows better short-term noise as we can compare between the Allan variance and the phase noise profile. The main advantage of the Syrlinks clock over the Rakon one is the price. The EWOS 0830 from Syrlinks, is a device manufactured with components off the shelf. The company offers some screening tests to be validated for space use. On the other hand, Rakon clocks are fully compliant with space qualification. **Note that in this work it was not possible to evaluate both clocks due to a time delay in the Test Bench development. The results presented here are only for the Syrlinks clocks.**

Comparing these values with CONSERT clocks shows that for temperature and aging variations, the stability of the clocks is one order of magnitude better, and the voltage variation stability is 3 orders of magnitude better. The size and power consumption for the Syrlinks clock remains of the same order but the Rakon clock consumes more power and it is heavier and bigger. However, in overall stability performance, both clocks are better than the CONSERT clocks.

As mentioned before to reduce noise introduced by the internal PLL of the FPGA board we used an external PLL. This PLL is contained in its own development board. The board is from Silicon Labs and the model is Si-5342 (Figure 49). This board permits to synthesize any output frequency from 0.1 Hz to 250MHz with any input frequency

from 8 kHz to 250 MHz. The datasheet states that for any type of synthesis, fractional or integer, the RMS jitter remains below 120 femtoseconds. This jitter noise is lower than the resolution of the DDMTD.

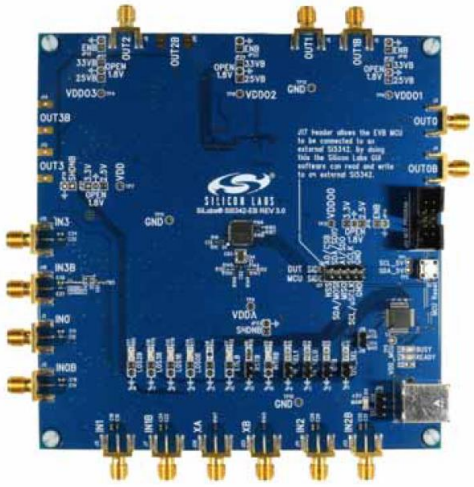

Figure 49. External PLL development board. SI5342 Silicon Labs. (Photo: from datasheet)

The test bench measures the time difference between a pair of clocks. Each clock is contained in its own box and enclosed with a temperature sensor. This temperature sensor will be used to characterize the stability of the clocks against temperature changes. The clocks are connected directly to the FPGA board and/or the external PLL board, depending on whether the external PLL is used or not (Figure 50).

The communication is performed via USB serial port from the FPGA board to the computer. The incoming data is read with a Python script and the raw data is stored without any treatment in binary format. The beat frequency is close to 1 kHz, so a transmission containing all the values is received every millisecond.

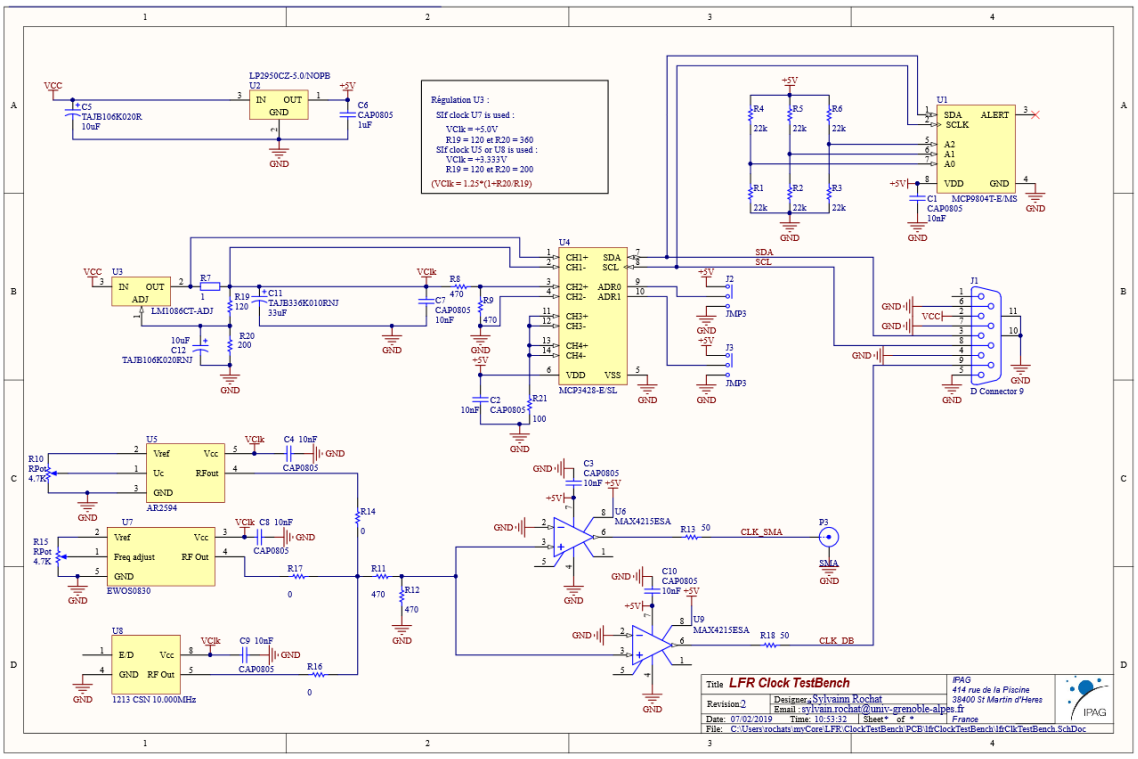

Figure 50. Schematic of the clock boxes.

5.3.2. Digital Design

Besides measuring the time difference between the clocks, the first test bench was also designed to measure other variables. In Figure 51 we can observe the block diagram of the digital design and we can observe that there are 7 different counters. Furthermore, it is shown that each Start, Stop and clock input of each counter is connected to different signals. Counter 1 and 2 both measure the time difference between clocks, however, the Start and Stop signals are interchanged for each counter. This means that Counter 1 measures the time difference starting with a rising edge of the Beat2 signal and Stops with the rising edge of the Beat1 signal, while for Counter 2 it is inversed. This provides the complementary cycle measurement seen in the time diagram in green and yellow (Figure 51). For these two counters, we expect that the counter register has an overflow and restart again every time there is a clock cycle lost or gained in the accumulated time error.

Counter 3 and 4 measure the period of each beat signal. This value will be used to unfold the accumulated time error. Thus these two Counters use one of the beat signals as the Start and Stop. Their expected behavior is to measure the same value for the whole test. We expect that the Period of the beat frequencies is not changed, at least not for the beat signal of the reference clock.

Counter 5 and 6 only measure if there is a cycle overflow, meaning if the time difference goes beyond one cycle and starts again. These values will be used to help the unfolding of the accumulated error as a corroboration. The only values that these counters can measure are 0, 1, and 2. The expected value is 1 the other two values represent the gain or loss of a complete cycle in the accumulated time error. In the time diagram, we can see that the Counter 1 is approaching a time difference of 0 and the next value measures a complete cycle. In this case there is one cycle error and therefore Counter 5 changes its expected value from 1 to 2.

Counter 7 counts the number of rising edges of the beat frequency from the reference clock. This rising edge is also responsible for the transmission of the data. Every time there is a rising edge of this signal the counters are read and transmitted to the PC. Therefore this counter gives the number of transmissions making it easy to visualize transmission errors and missing data. The expected behavior is an increment of 1 every transmission, if there is another increment there is a loss of data.

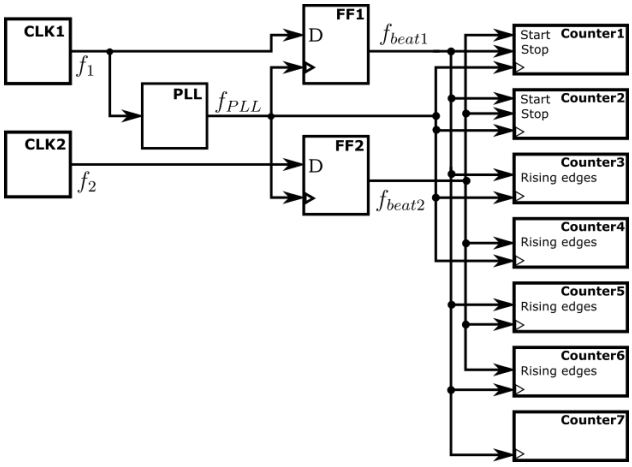

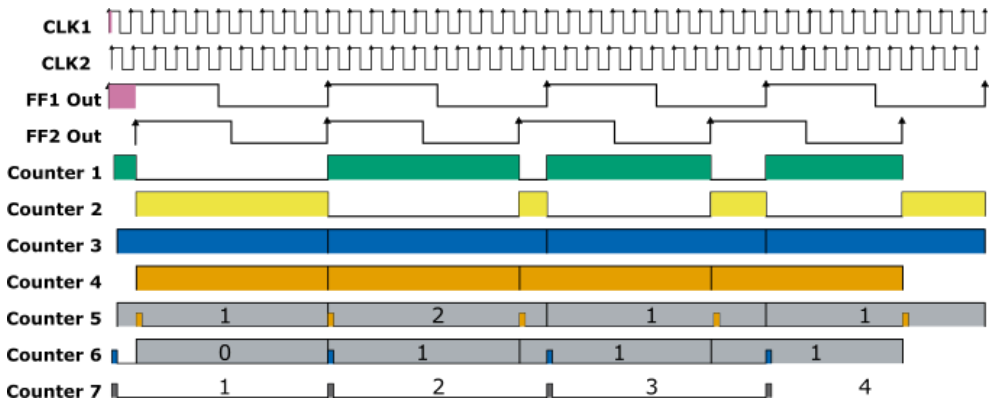

Figure 51. Test bench digital design block diagram as well as the time diagram representing each of the values measured by the test bench.

In this design, we consider Clock 1 as the reference clock. This clock will drive the PLL to synthesize the frequency which is used as the clock input of the Flip Flops. In Table 9 we see a résumé of the variables measured by each Counter.

Table 9 Variables measured in each counter. Start, stop and counter signals are explained.

Counter	Start	Stop	Clock	Measurement
1	Beat1	Beat2	PLL	Time difference between Clock 1 and clock 2
2	Beat2	Beat1	PLL	Time difference between Clock 2 and Clock 1
3	Beat1	Beat1 next edge	PLL	Period of the beat 1 signal
4	Beat2	Beat2 next edge	PLL	Period of the beat 2 signal
5	Beat1	Beat1 next edge	Beat2	Lost/gain of 1 cycle in the accumulated error
6	Beat2	Beat2 next edge	Beat1	Lost/gain of 1 cycle in the accumulated error
7	N/A	N/A	Beat1	Number of transmitted packets

Glitch effect in the FPGA

A glitch effect can be observed in the FPGA system when mixing the two signals coming from the clocks and the PLL in the Flip Flops. When there is a change of the logic level of the signal in the output of the Flip Flop, it generates a random change in the output level for a small amount of time before remaining in the correct state. This glitching effect will introduce an error in the measurement. To reduce this effect, a deglitching subsystem was implemented in the FPGA that takes only the first change in level as the real state.

The glitch effect shows a variation of 200 to 700 ns, which corresponds to 2 to 7 counter counts (Figure 52). This error, while small in comparison to the accuracy needed for the phase could represent a limitation for the Pong-Pong technique as we will explain in the next sections. The deglitching technique could be improved in several ways, but we concluded that the first transition is sufficient for our purposes.

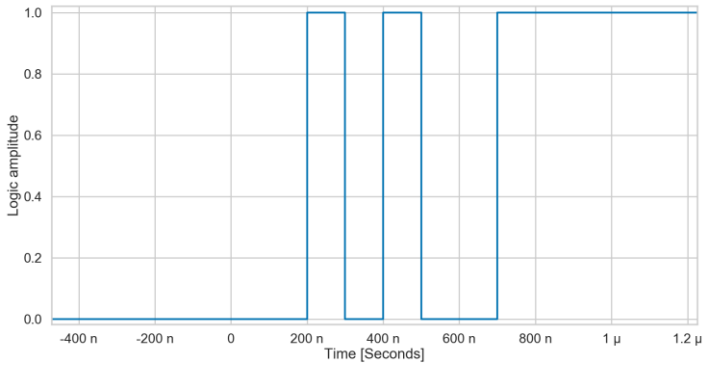

Figure 52. Glitch effect. Three different level changes are shown before remaining at the correct level. Recreated from the timestamps of rising edges.

5.3.3. Fridge

The fridge used (Figure 53) can generate temperatures from -30° (lowest allowed by the clocks) to 0°C shown in. It provides the means needed to perform temperature tests with the Test Bench and characterize the clocks against temperature variations.

Figure 53. Test Bench. The gray boxes contain a clock and a temperature sensor. The white box in the background is the fridge.

5.4. Data Preprocessing

Data is saved directly in a binary file from the FPGA; therefore, before any type of analysis, the data must be processed, given the correct format and verified. This process is explained in detail in Annex A.

The data is saved in binary format, therefore, can be read and create groups of four bits to generate ASCII characters. The data saved is the one coming from the 7 different counters. When used the data is converted into decimal number format and arranged into different variables for each counter. The available data after preprocessing, is the time error accumulation, the period of the signal and temperature.

5.5. Test bench verification

To evaluate the noise floor, or the noise introduced to the measurement by the test bench we connect only one clock to both inputs of the test bench. This way the drift coming from the clock is canceled during the data analysis and the only noise measured is the one coming from the test bench itself.

The noise floor test was conducted with one clock connected to both inputs of the test bench. The clock and the system were at room temperature, the data acquisition was performed for approximately 27 hours, and 100 M samples per Counter were received by the computer. This 27-hour test was repeated approximately in the same hours of the day for 3 different days. Note that 27 hours is more than the expected duration of a Scan (~12 hours). This is because the test was performed for the two available PLL possibilities to measure the noise floor of each technique. In Figure 54 we have the period of the beat signal and the time difference measured with the Test bench using the internal FPGA. These plots only show 12 hours of the test. As we expect, Period and Time difference remain stable for the complete test. The red line above the Period plot shows the mean value for the 12 hours.

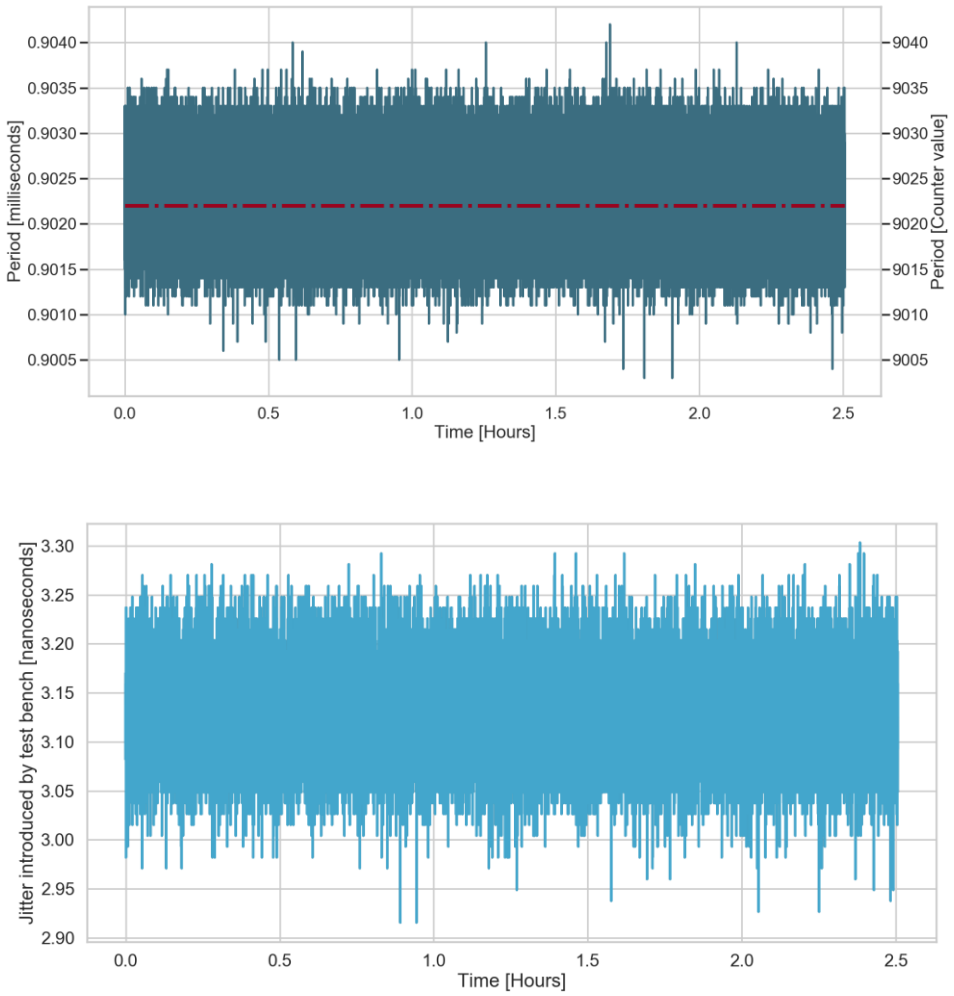

Figure 54. Top: Period of the beat signal from the reference clock measured by the test bench. In red the mean value for a set of 12 Hours is shown. Bottom: Jitter inserted by the test bench. Since the test is done with only one clock there is no drift. This test was performed using the internal PLL. Data showed for a reduced time.

For the internal FPGA, the Period for different files and different days shows a constant value around 0.000902 seconds. The difference between the measured beat period and the expected 1 millisecond period is due to the capacity of the internal PLL of the FPGA to generate frequencies using integer values for the dividers. The fractional divider synthesis in the internal PLL generates significant noise to be considered useful for the test.

In contrast, the external PLL generates a beat period of 0.000999 seconds. Even though it uses a fractional frequency divider to perform the synthesis, this board delivers a low-jitter signal.

The phase measured between both inputs remains constant for the full time of measurement displaying some noise. The noise in this measurement represents the noise introduced by the system.

The phase data collected was analyzed using the Modified Allan Deviation (MAD) analysis. In Figure 55 the MAD for the external PLL (dark blue) shows that up to 0.1 seconds the noise is white phase noise. We can recognize the white phase noise since it shows a slope of $\tau^{-3/2}$ as was shown in Figure 17 for the Modified Allan Deviation. After 0.1 seconds we can see a periodic component. This periodic instability comes from the use of fractional dividers in the synthesis of the external PLL. In light blue, the MAD of the internal PLL is one order of magnitude higher for the times before 0.1 seconds. However, after the periodic noise starts in the external PLL, the internal PLL exhibits the same floor noise as the external PLL but without any periodic disturbance.

We can conclude that for an analysis of the time scale between Ping to Pong it is better to use the external PLL as we have a better noise floor, but for time scales above the Ping to Pong, it is better to use the internal PLL to avoid the periodic noise. Also, by looking at the slope of the MAD plot, we can conclude that besides the periodic disturbance, the noise is white phase noise, allowing averaging to reduce the noise in the data.

In Figure 56 there are 3 different tests for each type of PLL. For the internal PLL, these 3 tests only differ in the day of measurement. While for the external PLL there is a change in the frequency dividers used. Notice that not all the tests were performed for the same amount of time and that the data was decimated. The analysis shows that all the tests perform similarly for the internal PLL. For the external PLL, all tests show the periodic noise and a lower noise floor. The reduced effect in the periodic noise in the external PLL tests compared to the last plot is due to the decimation of the data used for Figure 56. The difference in the periodic noise for the external PLL tests is coming from the selection of different values for the dividers for the fractional frequency synthesis.

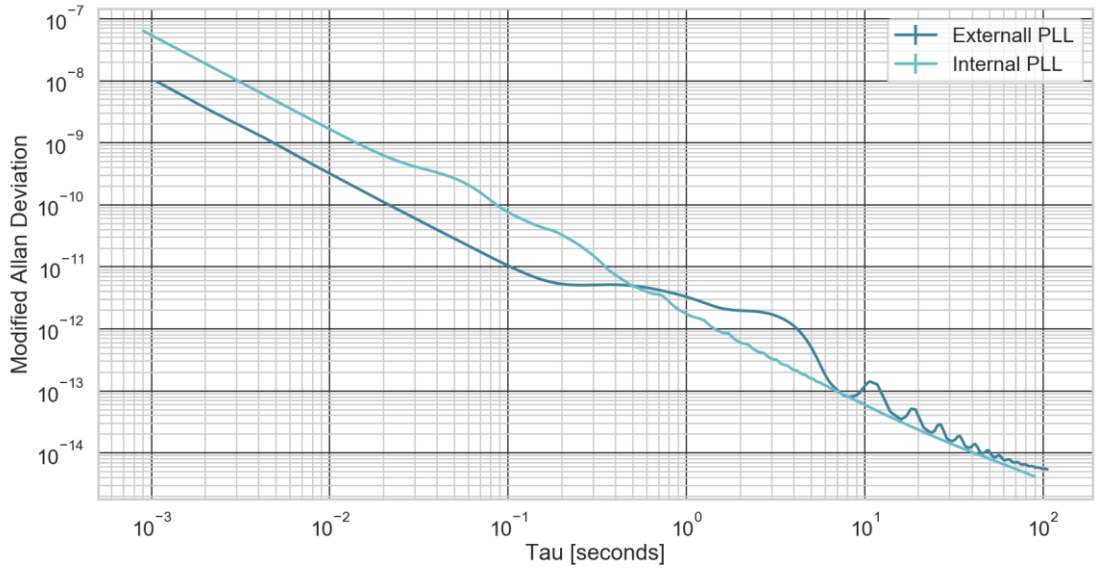

Figure 55. Modified Allan Deviation for one clock test. In dark blue external PLL and in light blue internal PLL.

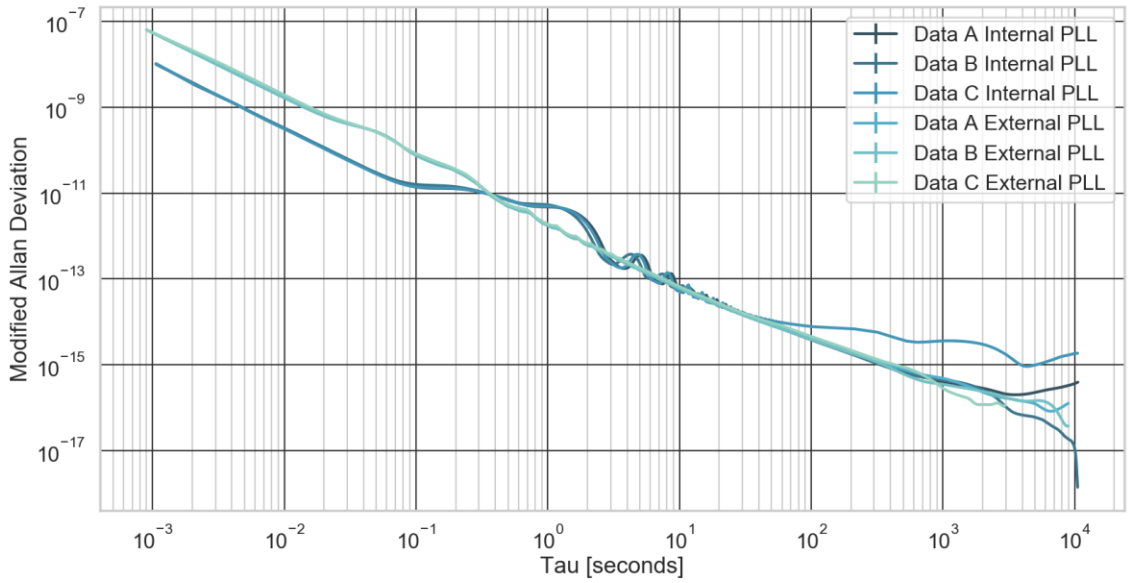

Figure 56. Three different tests for internal and external PLL of the noise floor of the test bench.

5.6. Test bench performances

The test bench was designed to deliver the time difference between two digital clocks for long periods of time. The fully digital conception makes it easy to implement

and limits the number of analog electronics involved. The type of test bench (DDMTD) was selected based on the needs of the simulator based on time events. The unfolded time difference delivers the accumulated time error giving direct access to the time error of time events between both electronics. Also, the time difference can be converted to frequency stability data to do noise analysis using the Allan Variance analysis.

The board time difference resolution is $\sim 1 \times 10^{-11}$ seconds which comes from the zooming effect of 10000 of the ~10 MHz clock used for the counters. The noise floor reached for the Test Bench depends on the time scale and the PLL used for the test. For the internal PLL, the noise floor is ranging from 10^{-7} to 10^{-14} using the internal PLL for 1 ms to hundreds of seconds, and for the external PLL the range is 10^{-8} to 10^{-14} for the same amount of time. The selection of the PLL for the test will depend on the time scale we are interested in the analysis, i.e. for Pong-Pong with a possible duration between 100 ms and over 1 s it is better to use the external PLL as the noise floor is better at this time scale. For longer times the internal PLL offers the same floor noise as the external PLL but without the periodic noise. Therefore, the test bench at a scale of 100 ms using the external PLL can measure with an accuracy of 2×10^{-10} seconds, which is in the range of 10 degrees of the carrier frequency which was the proposed resolution for the phase measurement.

The incoming data has a frequency of 1 ms, which is faster than the time between the time events of interest. With this is possible to average data to improve the accuracy of the measurement. This acquisition time could be easily modified by changing the frequency output of the PLL. Which complies with the requirement of measuring the time difference between clocks faster than the time events.

The temperature sensor provides the possibility to characterize the clocks during temperature variations. This gives the possibility to implement methods that could use this information to improve the science return.

The necessary preprocessing of the data is fully detailed in Annex A, which contains the translation from the stored hexadecimal file stored to the respective time values for each of the measured values. As brief description this process was fairly simple making the test bench a useful tool for the time analysis of the transponder

concept. The most complex and time-consuming part of the test bench development was the electronic digital description for the FPGA.

At the time of writing the Thesis, a new version of the Test Bench was under development. We decided that to improve the data gathering in the FPGA the digital design could be reworked. These modifications impulse the redesign of the electronic boards and the sensors we can use to characterize the clocks. Therefore a sensor of voltage and current were added to each clock board, enabling the characterization of power consumption during temperature variations. We will give a better insight into this topic in the last chapter in the perspectives of the work. Nevertheless, the results presented in this work will refer only to the first version of the Test bench exposed in this section.

The first version of the test bench used a 16-bit register for each counter output and transmitted each 16-bit register as 4 ASCII characters. Therefore 9 registers are used for the Counters each one of 16 bits which are 36 ASCII characters. The delimiter between counter values is a semicolon (;) which counts as another ASCII value. There are 8 delimiters in each line. Each line also needs a line terminator which is a carriage return and a new line, which is 2 more ASCII characters. Each ASCII character needs a start and a stop bit. In total, each transmitted line is composed of 460 bits.

The beat frequency is the rate of data transmission. Ideally, it is1000 Hz, but for the internal PLL, it is 1108 Hz that means 1108 data packets per second. The Baud Rate should be higher than 509680 bits per second.

The External PLL is closer to the 1000 Hz transmission frequency, so the baud rate used for the internal PLL is also useful. The communication is done via USB to the computer which stores the data received directly in a file without any processing. A brief description of the dataset coming from the first test bench version is provided in Annex D.

5.7. Integration of data Test Bench to Simulator

The Test Bench measures the time difference between clocks. If this time difference is unfolded, we can retrieve the time-accumulate

d error. These time differences can be used to characterize the stability of the clocks against environmental changes, and also to introduce them in the long term simulator, to evaluate the Pong-Pong technique as a clock drift measurement and the phase and time compensation techniques.

The values received from the test bench include the time difference between clocks and the period of the Beat signals. From this, we can estimate the mean value of the period which we will use as a reference value for the beat frequency. Using the beat frequency the time differences can be unfolded, generating the accumulated time error during the whole test. The accumulated time error measured by the DDMTD can be considered in our Time model as the difference between Orbiter times and Lander times. This time difference Δt is measured in seconds.

$$\Delta t = t_{ORB} - t_{LAN}$$

For example, for the time events proposed in the time model:

$$\Delta t_S = t_{OS} - t_{LS}$$

$$\Delta t_T = t_{OT} - t_{LR}$$

$$\Delta t_R = t_{OR} - t_{LT}$$

Where $\Delta t_S, \Delta t_T, \Delta t_R$ are the time difference between Orbiter and Lander Times at different time events (Orbiter start, Orbiter transmission, and Orbiter reception) measured by the test bench. In Figure 57 we see a representation of the data obtained from the Test Bench. In green, we observe the data received by the Counter 1 (time difference between beat signals) and in orange the data received by the Counter 3 (period of the reference beat signal).

To simplify the insertion of the data from the Test Bench into the simulator, we consider that the time intervals between time events, ($\Delta Ping,\ \Delta Pong,\ \Delta PP, \Delta S$), are all multiples of the beat frequency, which is the frequency of the measurement of time differences (See Figure 58).

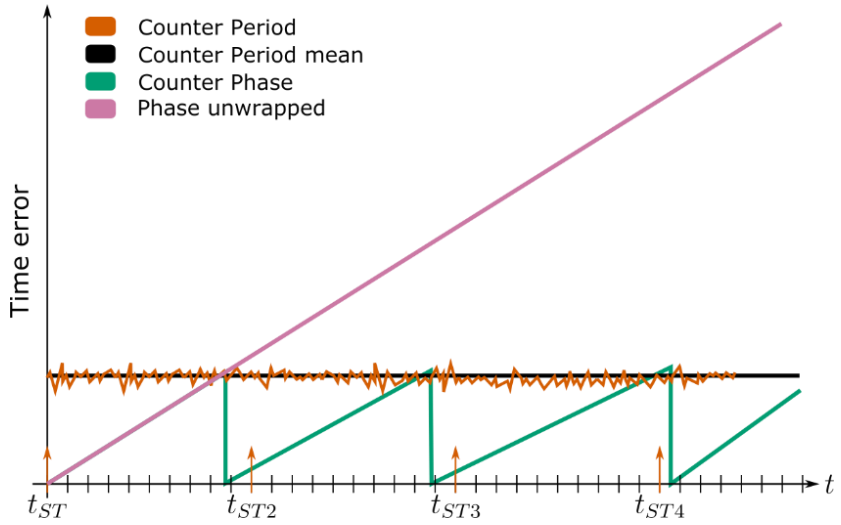

Figure 57. Graphical representation of the data obtained from the test bench.

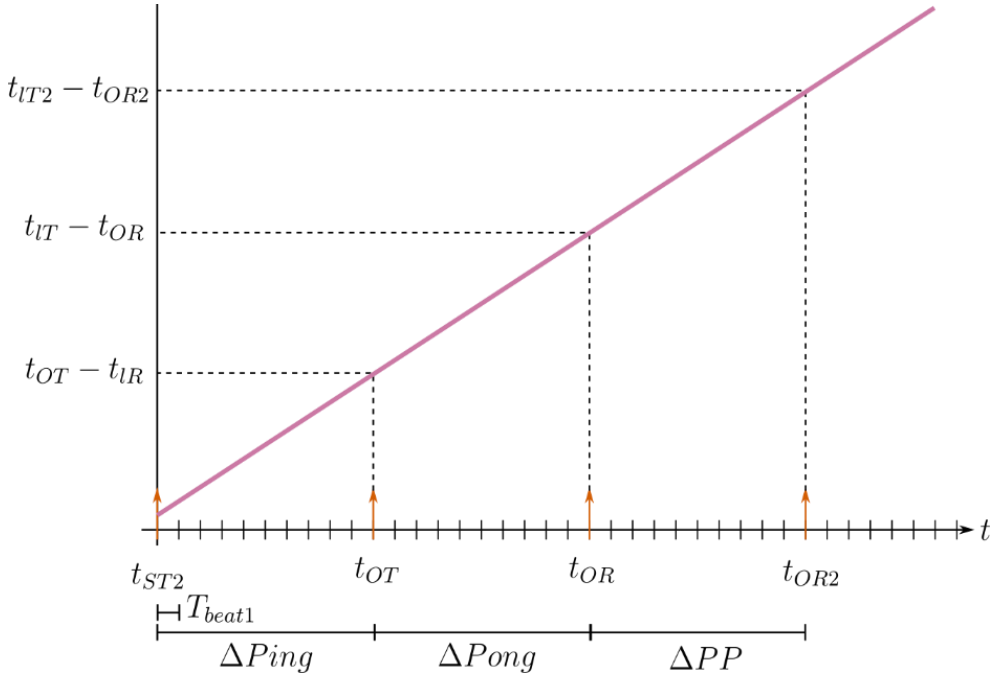

Figure 58. Integration of the data from test bench into the simulator. The times between time events are multiples of the beat Period

The calculation of the propagation delay measured in the Lander developed in the time analysis chapter (shown below again):

$$\tau_{LAN} = [(t_{OT} + \tau_0) - t_{lR}]$$

Can be substituted by:

$$\tau_{LAN} = \Delta t(t_{OT}) + \tau_0$$

Where $t_{OT} = nT_{beat1}$ and $\Delta t(t_{OT})$ is the value of the time difference measured at the time of the time event of Orbiter transmission. Similarly for the other time events.

$$\tau_{ORB} = \Delta t(t_{OR}) + \tau_0 + \tau_{LAN}$$

$$\tau_{ORB2} = \Delta t(t_{OR2}) + \tau_0 + \tau_{LAN}$$

From the accumulated time error data, it is then possible to create three sets of values, each one representing one Orbiter time event for all Soundings in the Scan (Figure 59).

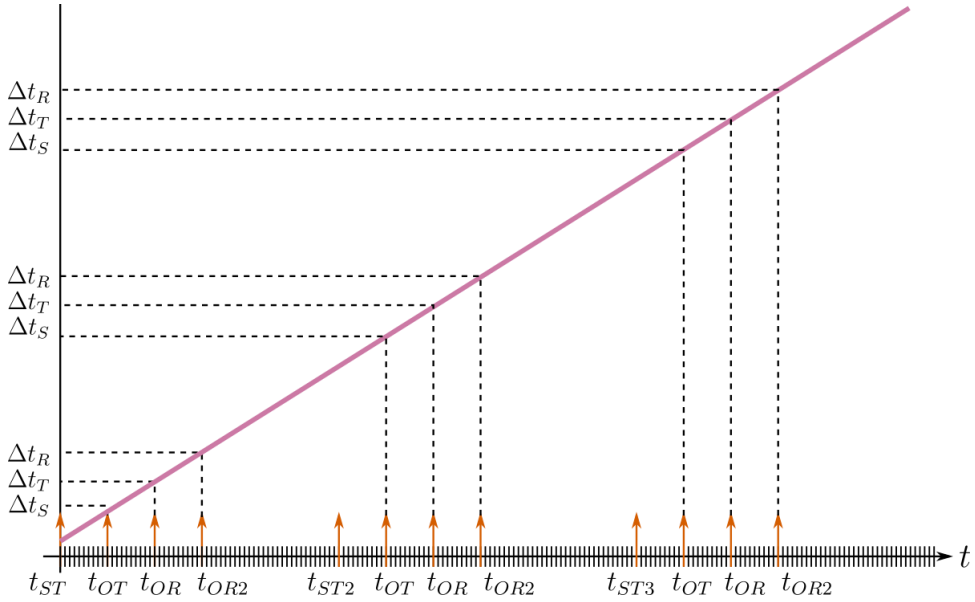

Figure 59. Creation of the data collections from the test bench data for each time event in the time model.

These collections of values are then used to calculate the propagation delay measured in the Lander and in the Orbiter in the same way as it is done in the simulator. We can include system errors as the sampling error and environmental errors as the SNR of the received signal after going through the asteroid.

As said before, the data from the test bench is the time difference between both clocks. In Figure 60 we can see the time difference between clocks for the start time

event ($\Delta t_S = t_{OS} - t_{LS}$) shows a linear behavior. This means that the clock drift for this range of time (2.5 hours) behaves as a constant parameter and there is no sign of aging

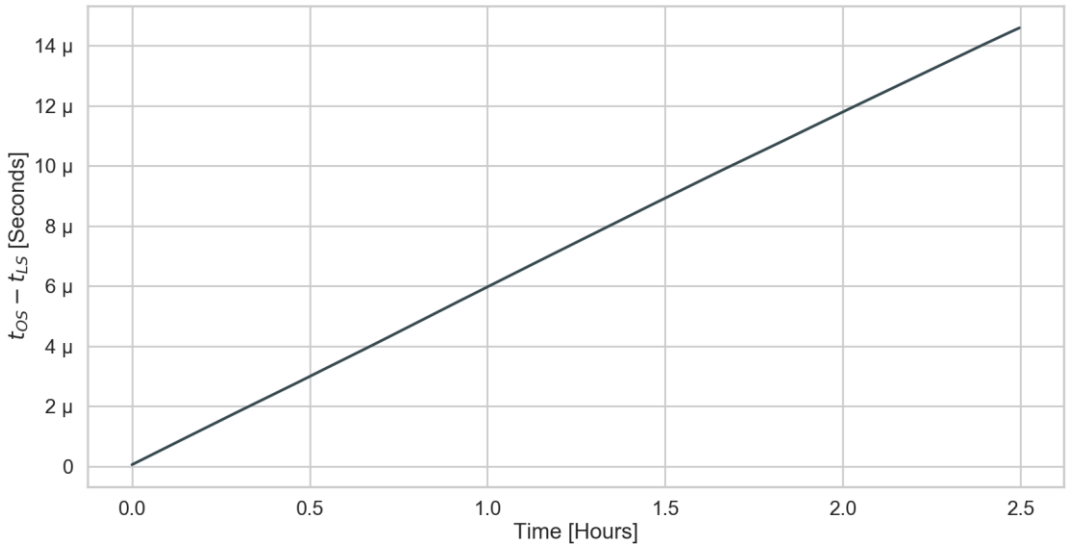

Figure 60. Accumulated time error for start events from the data of the test bench. The test included 2 Syrlinks clocks measured for 2.5 hours.

or any variation from another parameter in the frequency stability.

For validation and comparison purposes, we will estimate the clock drift using the clock drift follow technique which uses both Pong transmissions. Having the two Pong propagations the next step is to calculate the frequency drift between both clocks by using the clock drift follow technique explained in the Time analysis section. In Figure 61 we observe the clock drift $\Delta f/f$ measured by the test bench in red, and the clock drift $\widehat{\Delta f}/f$ estimated with the clock drift follow technique with a time between Pong transmissions of 0.5 seconds in pink. As expected from the linear time error accumulation, the clock drift is almost constant with some variation over time.

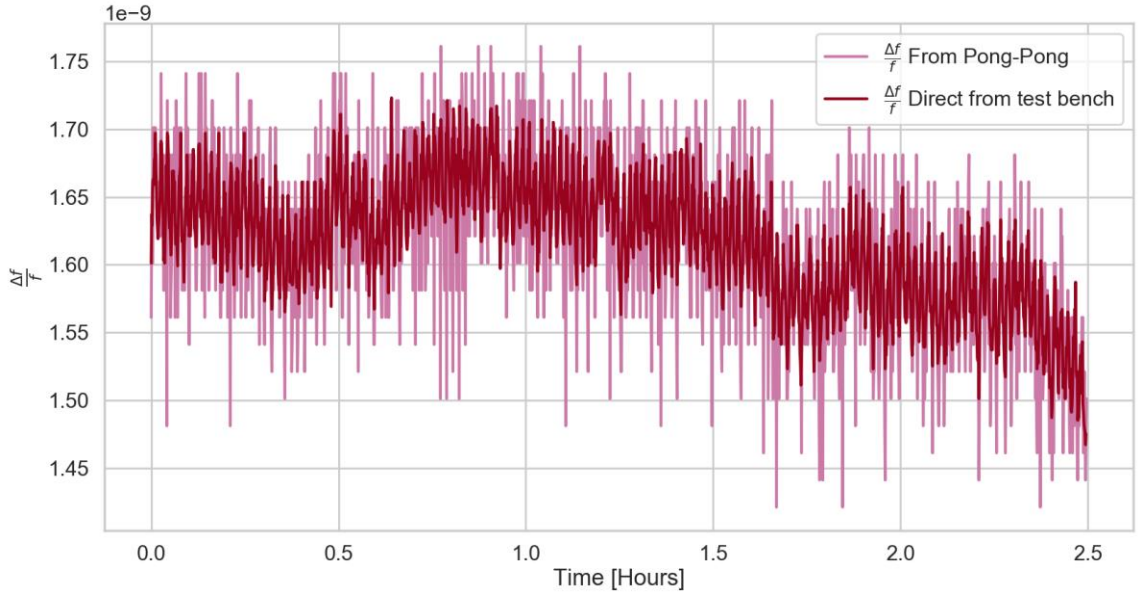

Figure 61. Clock drift measured from the data of the test bench using the Pong-Pong technique.

Chapter 6. Clock validation and compensation methods

First, we will start by validating the clocks selected for the mission. This validation will be exeuted by comparing the measured data with the requirements which were established for each of the time scales mentioned in the LFR Time Analysis section. Subsequently, we will use the data from the test bench with the simulator to evaluate the clock drift measurement technique, as well as the reconstruction and compensation methods in time and phase.

6.1. Clock validation for frequency requirements

First, we did the MAD analysis of the data of the time drift between two clocks. This test uses the datasets that include temperature variations, from -30° to -10° C for only one clock, to observe how temperature affects the short term stability. As shown in Figure 62 the short-term noise is close to 10^{-9} at the scale of Coherent Accumulation (13 ms). In fact, at this time scale, the noise measured in these tests is the noise produced by the test bench and not by the clocks. As Figure 62 shows, the noise floor of the test with one clock is exactly the same as the noise measured between two clocks for different tests. This result is almost two orders of magnitude better than the 10^{-7} specified for this time scale in the requirement analysis. The analysis was performed on data using the internal PLL and the fridge to have temperature variations.

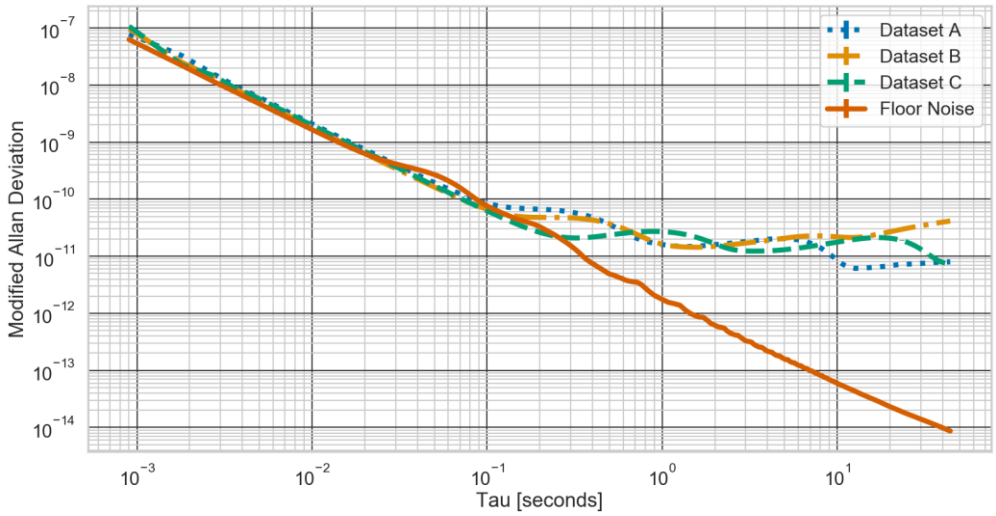

Figure 62. The MAD plot for three different data sets using internal PLL and the fridge. As well as a one clock test with internal PLL to compare to the floor noise.

To validate the time scale of Tx-Rx windows we plot the time-accumulated error over 12 hours. It shows that the accumulated time error is less than a millisecond and therefore lower than the requirement for the movement of the Tx-Rx windows of tens of milliseconds (Figure 63).

We can expect the same results from the Rakon clock as its specifications are similar to the Syrlinks clocks. As stated before, the Syrlink clocks are cheaper than the Rakon clocks but as they are constructed using COTS, the quality remains uncertain even after screening tests. This could put a margin of the danger of component damage due to the harsh environment of a planetary mission. The Rakon clock, although more expensive, are completely space-qualified, giving the margins needed for the planetary mission.

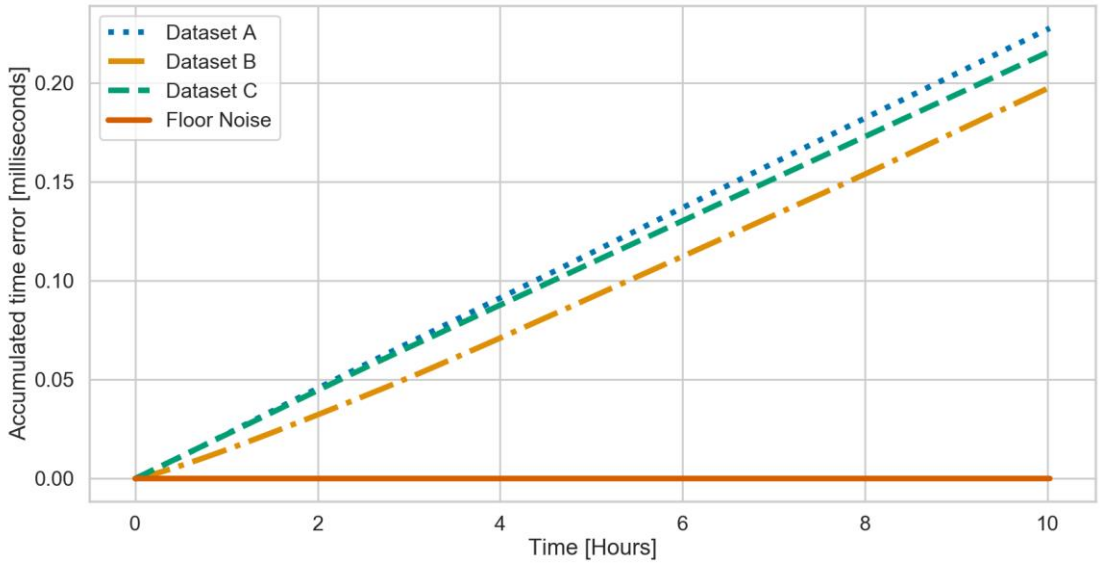

Figure 63. Accumulated time error for three different tests using the same parameters. Variations in temperature were applied during the tests to one of the clocks. The only difference between tests is each test was performed on a different day.

The time scale of Ping to Pong, or from reception to transmission in the Lander, can be validated by taking the difference between the Lander time events of transmission and reception

$$t_{L(T-R)} = t_{LT} - t_{LR}$$

To verify this requirement we set the value between Ping and Pong as 100 ms which is equivalent to 100 samples from the test bench as every sample is received every 1 millisecond. The difference between Lander transmission and reception times must be always below 2 nanoseconds plus the time between Ping and Pong which is 100 ms.

In Figure 64 we can observe the difference between Lander transmission and reception times. This value is always below the required value for the frequency requirement. The value in the plot is differentiated with 100 ms to just leave the error to be compared with the 2 ns of the requirements.

The other two time scales will be analyzed in more detail in the next sections, after introducing the compensation methods that will be used for both of these time scales.

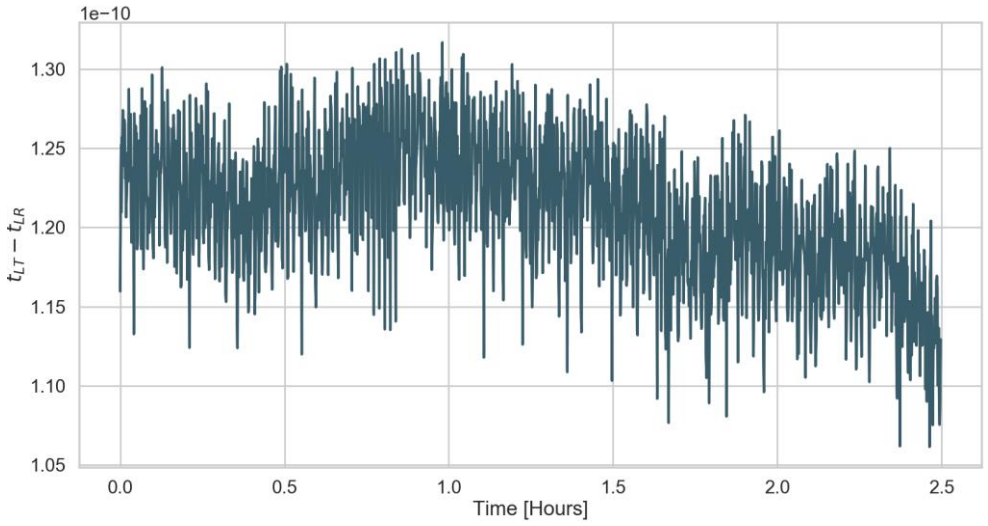

Figure 64. Difference between Lander reception and transmission times for 2.5 hours.

6.2. Phase and time reconstruction

6.2.1. Clock drift estimation

From the expression obtained for the clock drift of the Pong-Pong (shown again below), we can observe that the accuracy can be improved by increasing the time between Pongs and by changing the minimum possible difference between both propagations. The model shows that both values are linked. If we increase the time between transmissions the minimum value difference between propagations increases as well because there will be an increase in the time error due to the clock drift. We can know the accuracy of the clock drift measurement by knowing the accuracy of the propagation delay measurement and the accuracy of the time between propagations. The error in the propagation delay measurement is coming from the noise of the test bench and the time error introduced by the SNR. The time between both transmissions ΔPP is measured in the reference clock, so the only possible error in this time comes from the digital delay between the command of starting the reception and the actual system starting the reception, so we can consider it negligible. It, thus; follows for the estimation of the frequency stability:

$$\frac{\widehat{\Delta f}}{f} = \frac{(\tau_{ORB2} + \sigma_{ORB2}) - (\tau_{ORB} + \sigma_{ORB1})}{\Delta PP}$$

where the σ_{ORB2} and σ_{ORB1} includes the noise from the SNR and the error introduced by the test bench. From the floor noise analysis, we can see that the external PLL test bench is better for testing the Pong-Pong technique as it has a lower noise floor in the possible ranges of time between Pong and Pong transmission (0.2 to ~1 second). In our system, we are also limited in the time between transmissions due to the movement of the relative positions of the two electronics to guarantee that the signal travels on the same path for both transmissions. The next analysis was done using the two Syrlinks clocks and the external PLL.

For the first tests, we did not consider the time error coming from the SNR to be able to see the limits of the technique under "ideal" conditions in the test bench. In Figure 65 we see the clock drift estimated by the Pong-Pong measurement of 25 and 500 milliseconds respectively. By increasing the time between transmissions from 25 to 500 ms we observe an improvement of the accuracy. This is because the noise introduced by the test bench is reduced by the division of a greater time. For a time of 25 milliseconds, we can observe that the accuracy reached is 4×10^{-10} which is exactly the resolution expected for the minimum time difference that can be measured by the test bench of 1×10^{-11} divided by 25 milliseconds. As we increase the time between transmissions to 500 milliseconds the accuracy of the measurement increases but never reaches the ideal resolution. Nevertheless, the accuracy to measure the clock drift improves (Figure 65).

Adding the time error coming from the SNR shows that the noise from the SNR will be the predominant limitation for the frequency stability measurement accuracy. We used the same data as the example before and added the time error coming from the SNR model using 40 dB in power for both Pong receptions in the Orbiter. The SNR in the reception will degrade the accuracy of the estimated clock drift between clocks. The 40 dB in the SNR model represents a deviation of $\sigma = 3.83 \times 10^{-11}$ in time error of the peak detection which is in the order of the phase resolution of the Test Bench. In any case, we think that the deviation obtained by the model is very optimistic.

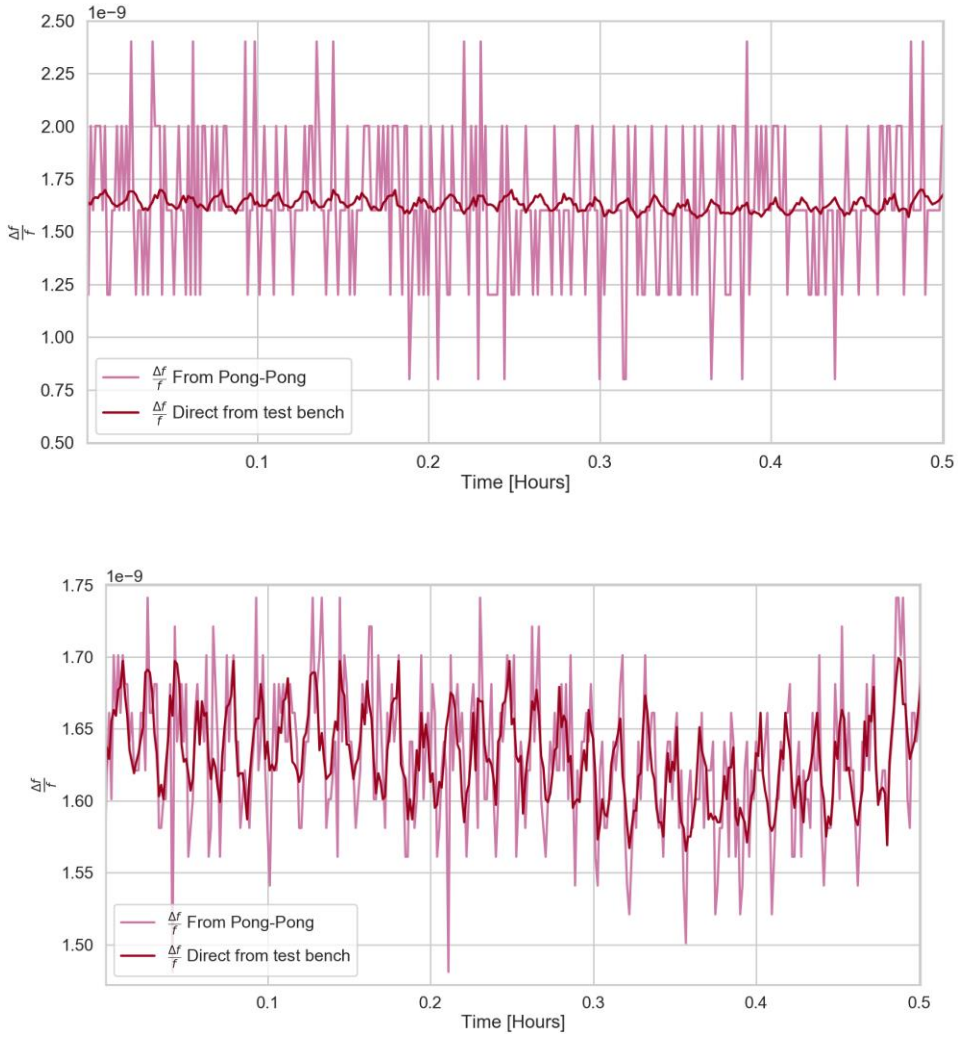

Figure 65. In pink, clock drift measured by the Pong-Pong technique and in red, real clock drift measured from the test bench. Top: Pong-Pong time of 25 ms, Bottom: Pong-Pong time of 500 ms.

To try to improve the estimation of the clock drift we applied a moving average filter to the data. Using 500 ms between Pong transmissions and 40 dB of SNR, the estimated clock drift in pink (Figure 66) shows that the noise introduced with the SNR model is the one leading the inaccuracy of the measurement. In green, we can see the moving average filtered signal which doesn't exactly fit the real value of the clock drift. This means that we cannot retrieve exactly the same profile of the $\Delta f / f$ measured in the test bench.

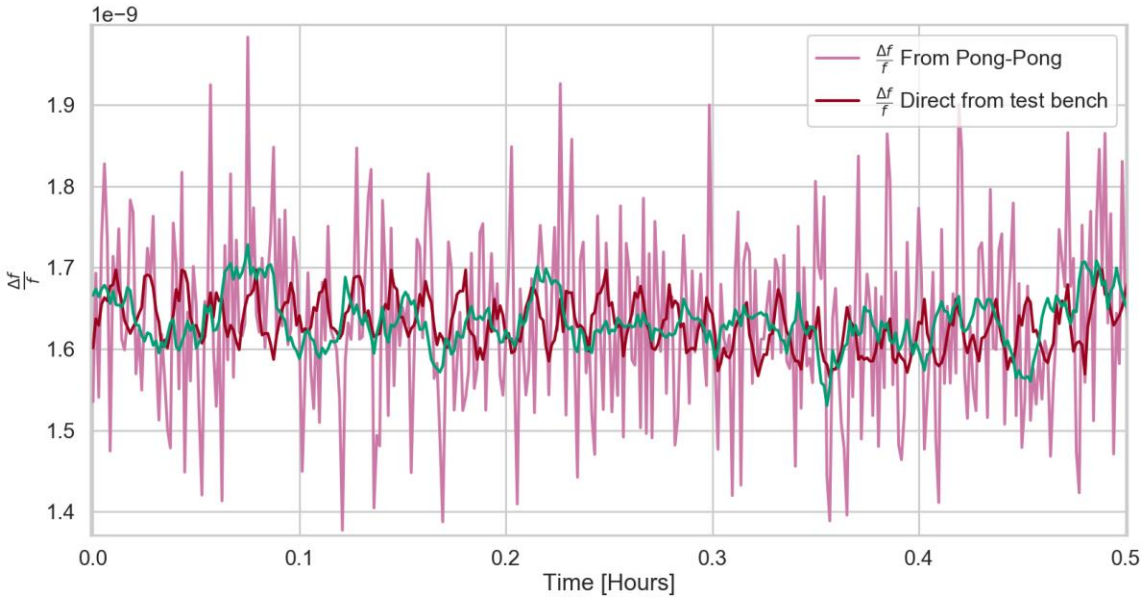

Figure 66. Clock drift measurement applying the SNR time error to the two Pong transmissions. In green the moving average of the clock drift measurement. Test: Pong-Pong time of 500 ms.

Another parameter to define for the Pong-Pong technique is the number of Pong-Pongs needed during a Scan. If the main contributors to the frequency stability change are slow in time (i.e. temperature and aging), there is no need to have a Pong-Pong transmission every Sounding. By just using some Pong-Pong transmissions over the Scan, we reduce the power and transmitted data consumption (Figure 67).

The best way to test the impact of less Pong-Pong transmissions is by reconstructing the time and phase of the Lander times in Orbiter reference and comparing them to the real deviation measured by the Test Bench. This will be done in the next section.

N.B. The data from the external PLL shows a periodic variation in the frequency stability, this is the result of the fractional divisions used by the PLL to generate the output signal.

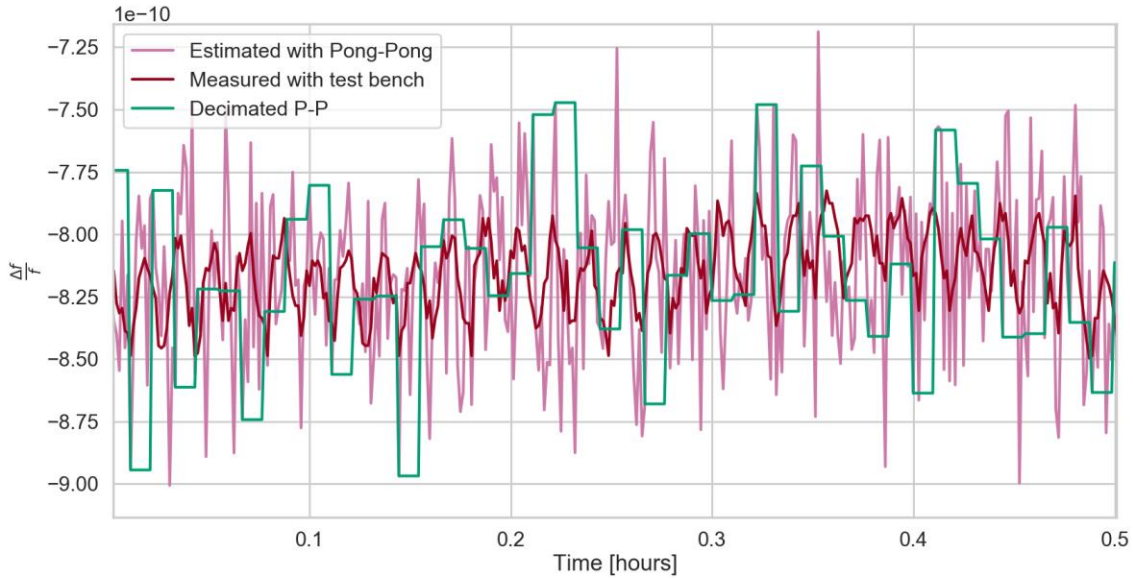

Figure 67. Decimated Pong-Pong transmissions. In pink: estimated clock drift with Pong-Pong technique, in red: clock drift measured with the test bench and in green: decimated Pong-Pong transmissions every 8 Soundings.

6.2.2. Time reconstruction

The data obtained from the test bench can be introduced in the simulator to estimate the clock drift $\widehat{\Delta f}/f$. The estimated clock drift is used to reconstruct the Lander times $\hat{t}_{LAN}$, and with this time reconstruction obtain the absolute time error for the whole Scan. In Table 10 we have the lander time reconstruction model, in this case, we only show the reconstruction of the starting times of the Sounding but it is straightforward to reconstruct every single time event inside each Sounding as the clock drift is considered constant during one Sounding.

Table 10. Lander time reconstruction using the clock drift estimated from the Pong-Pong technique.

Orbiter t_{ORB}	**Lander $\hat{t}_{LAN}$**
$\boldsymbol{t_{OS_1} = 0}$	$\hat{t}_{LS_1} = \hat{t}_{OS_1} + T_{ON}$

$\boldsymbol{t_{OS_2}} = \boldsymbol{t_{OS_1}} + \Delta U$	$\hat{t}_{LS_2} = \hat{t}_{LS_1} + \Delta U + \Delta U \left(\frac{\widehat{\Delta f_1}}{f}\right)$
$\boldsymbol{t_{OS_3}} = \boldsymbol{t_{OS_2}} + \Delta U = \boldsymbol{t_{OS_1}} + 2\Delta U$	$\hat{t}_{LS_3} = \hat{t}_{LS_2} + \Delta U + \Delta U \left(\frac{\widehat{\Delta f_2}}{f}\right)$ $= \hat{t}_{OS_1} + T_{ON} + 2\Delta U + \Delta U \left(\frac{\widehat{\Delta f_1}}{f} + \frac{\widehat{\Delta f_2}}{f}\right)$
$\boldsymbol{t_{OS_4}} = \boldsymbol{t_{OS_3}} + \Delta U = \boldsymbol{t_{OS_1}} + 3\Delta U$	$\hat{t}_{LS_4} = \hat{t}_{LS_3} + \Delta U + \Delta U \left(\frac{\widehat{\Delta f_3}}{f}\right)$ $= \hat{t}_{OS_1} + T_{ON} + 3\Delta U + \Delta U \left(\frac{\widehat{\Delta f_1}}{f} + \frac{\widehat{\Delta f_2}}{f} + \frac{\widehat{\Delta f_3}}{f}\right)$
$\boldsymbol{t_{OS_N}} = \boldsymbol{t_{OS_{N-1}}} + \Delta U = \boldsymbol{t_{OS_1}} + (N-1)\Delta U$	$\hat{t}_{st_N} = \hat{t}_{st_{N-1}} + \Delta U + \Delta U \left(\frac{\widehat{\Delta f_{N-1}}}{f}\right) =$ $\hat{t}_{OS_1} + T_{ON} + (N-1)\Delta U + \Delta U \left(\sum_{n=1}^{N-1} \frac{\widehat{\Delta f_n}}{f}\right)$

Reminder: ΔU is the time between Soundings. The Orbiter times are considered the reference. The drift between Soundings is included in its totality in the $\Delta f / f$ terms.

The difference between Orbiter times $\boldsymbol{t_{ORB}}$ and the reconstructed Lander times $\hat{t}_{LAN}$ gives the time error between them $\widehat{\Delta t}$. The value $\widehat{\Delta t}$ is the estimated time difference between Orbiter and Lander times that can be compared to the value measured by the test bench, the time difference between both real clocks Δt. Therefore, by comparing these two time differences, we can determine the error between the true-time difference and the one estimated using the Pong-Pong technique.

$$\Delta t_e = \Delta t - \widehat{\Delta t}$$

This difference Δt_e between the real and estimated Lander clock drift will be useful to verify the frequency requirements of Sounding to Sounding after compensation. The reconstruction(Figure 68) was done with a time between Pongs of 0.5 seconds. We can see the error between the time difference measured by the test bench and the time difference between the Orbiter times and the estimated Lander times. The left *y*-axis shows the time error in seconds and the right y-axis shows radians. In fact, what we are looking at in this plot is the accuracy of the reconstruction of the time.

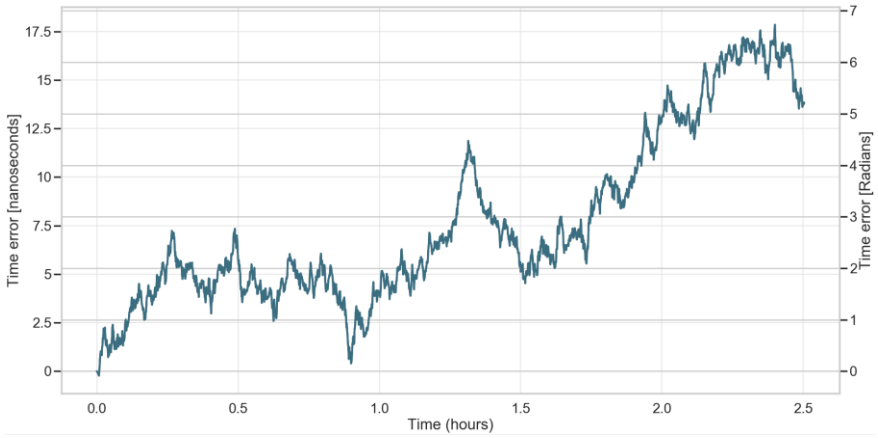

Figure 68. The error of the reconstructed Lander time. Difference between the measured Lander clock drift by the test bench and the reconstructed Lander clock drift using the estimated frequency difference by the Pong-Pong technique.

In Figure 69, we present the time error between reconstructed times and the time difference measured by the test bench for different times between Pong transmissions. This exercise can give us a first approximation of the time needed between transmissions to guarantee the compliance of the requirement with the time reconstructions. Nevertheless, several executions with the same time are needed to obtain a sufficient probability for the reconstruction since the noise is random in nature. From Figure 69 we can see that 0.5 seconds could be sufficiently accurate to solve the time compensation.

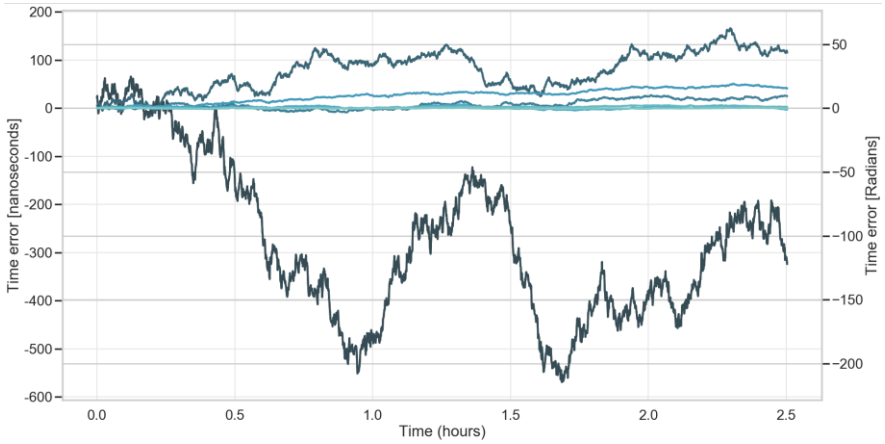

Figure 69. The error of the reconstructed Lander time for different times between Pong transmissions.

6.2.3. Phase reconstruction

From Sounding to Sounding, the phase coherence is lost due to the clock drift. By using the estimation of the clock drift from the Pong-Pong technique it is possible to reconstruct the time difference between Orbiter and Lander times and, therefore, obtain the absolute phase difference between electronics.

Using the estimated clock drift, it is possible to reconstruct the time of the Lander for each Sounding as follows:

$$t_{ST_N} = t_{ST_{N-1}} + \Delta U = t_{ST_1} + (N-1)\Delta U$$

$$\hat{t}_{st_N} = \hat{t}_{st_{N-1}} + \Delta U + \Delta U\left(\frac{\widehat{\Delta f_{N-1}}}{f}\right) = t_{ST_1} + (N-1)\Delta U + T_{ON} + \Delta U\left(\sum_{n=1}^{N-1}\frac{\widehat{\Delta f_n}}{f}\right)$$

We can rewrite the last term of the second equation as an average value of the clock drift

$$\sum_{n=1}^{N-1}\frac{\Delta f_n}{f} = (N-1)\frac{\widehat{\overline{\Delta f}}}{f}$$

And, therefore, we can rewrite the value of $\hat{t}_{st_N}$

$$\hat{t}_{st_N} = t_{ST_1} + T_{ON} + (N-1)\Delta U\left(1 + \frac{\widehat{\overline{\Delta f}}}{f}\right)$$

The term $(N-1)\Delta U\left(\frac{\widehat{\overline{\Delta f}}}{f}\right)$ refers to the time difference between both clocks, which is also the value measured by the Test Bench. By comparing these two values, we can determine the error between the reconstructed and the true-time difference and then convert this time into the phase of the carrier signal to recover the absolute phase difference between clocks.

For the clock drift estimation, it is important to note that the preferred data set is the one coming from the test using the external PLL. This is due to the fact that for short times (<1 s) the external PLL system shows lower noise.

In Figure 70 we show 1000 realizations to compare the time difference estimated by the Pong-Pong technique and the time difference measured by the Test Bench. In Figures 71, 72 and 73, we can see the distribution of this result for different times of the experiment: 10 min, 1 hour and 2.5 hours. In this case, the dirstibution after 10 minutes can be used as a comparison with the frequency requirement of the time reconstruction from Sounding to Sounding, the distribution after 1 hour as a comparison with the frequency requirement of the phase from Sounding to Sounding and the distribution after 2.5 hours to see the long-term outcome. We did this exercise for two different times between Pongs (0.5 and 1 second) and with a SNR of the power of 40 dB. The colors of the lines in Figure 70 are just to distinguish between realizations.

For all the distributions showen in Figures 71 to 77 we applied a normal Gaussian fit and showed the 1σ and 2σ values in green and pink dotted lines respectively.

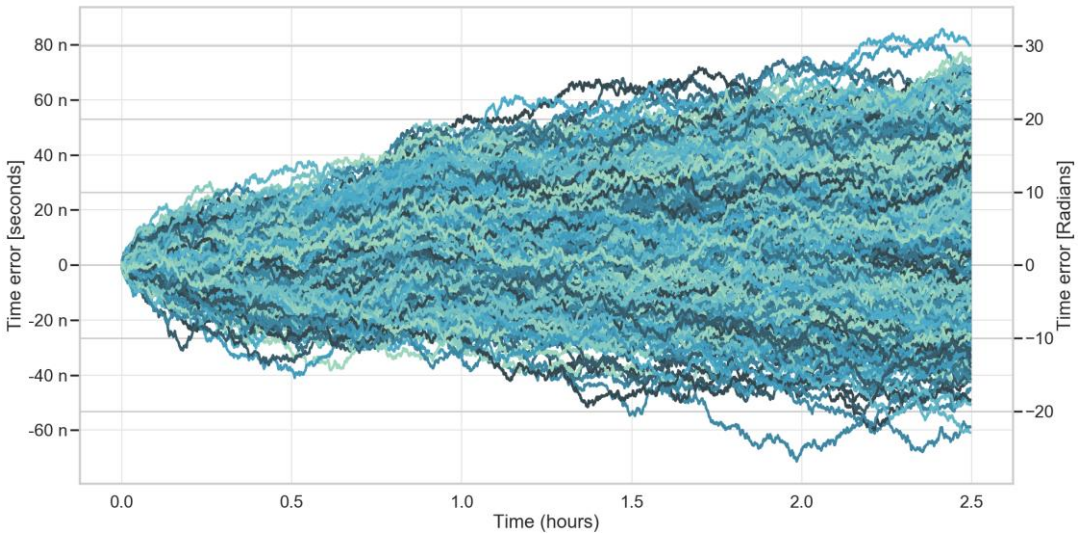

Figure 70. Accuracy of the reconstructed Lander time using 0.5 s between Pong transmissions and 1000 realizations.

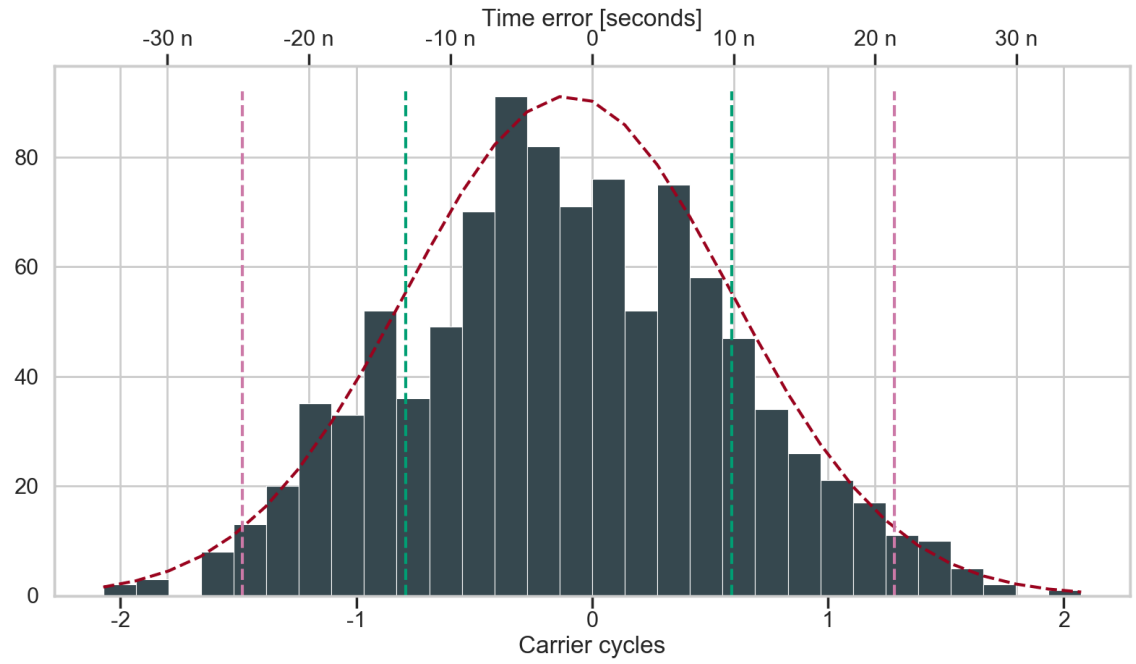

Figure 71. Distribution after 10 minutes for 1000 realizations with the time between Pongs being 0.5 seconds. $\sigma = 1.15 \times 10^{-8}, \mu = -1.66 \times 10^{-9}$ in seconds.

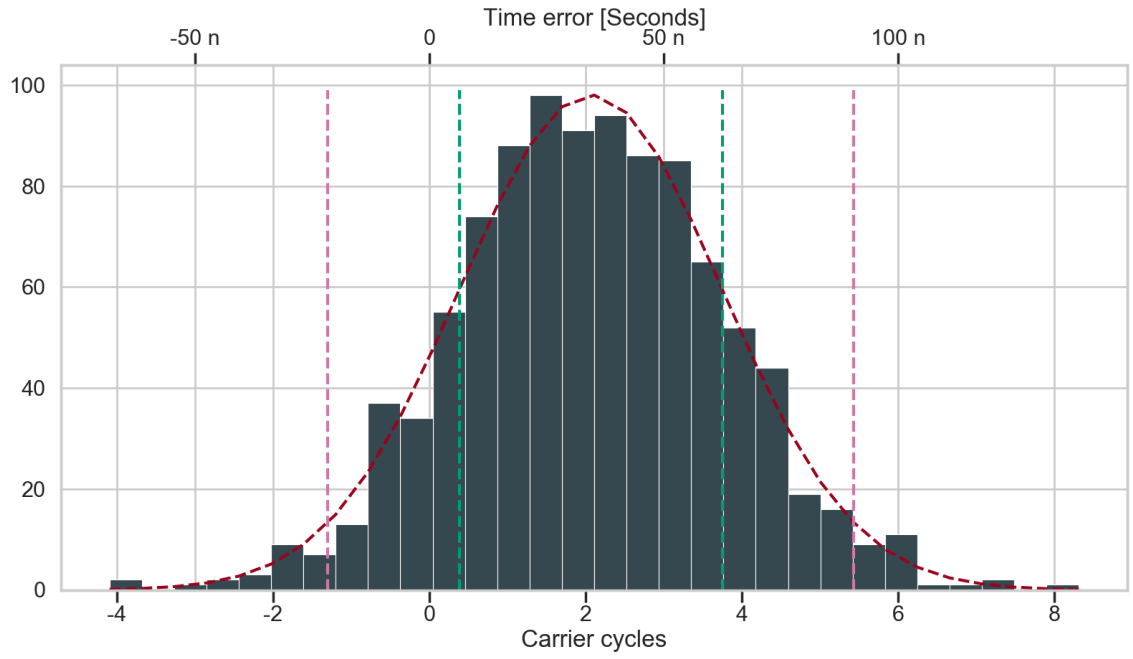

Figure 72. Distribution after 1 hour for 1000 realizations with the time between Pongs being 0.5 seconds. $\sigma = 2.8 \times 10^{-8}, \mu = 3.44 \times 10^{-8}$ in seconds.

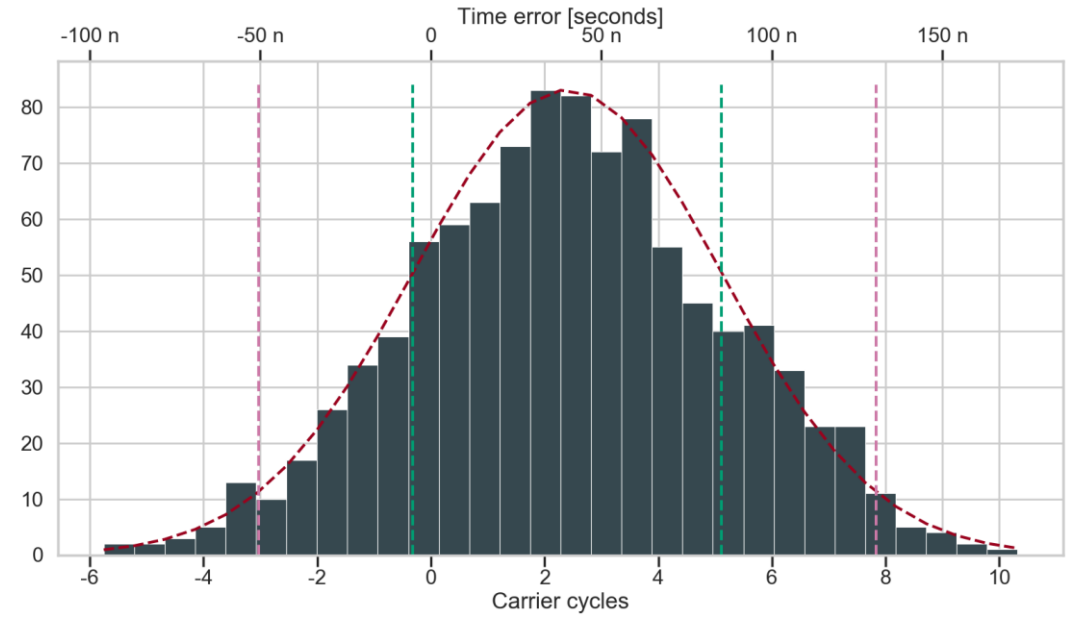

Figure 73. Distribution after 2.5 Hours for 1000 realizations with the time between Pongs being 0.5 seconds. $\sigma = 4.52 \times 10^{-8}, \mu = 4 \times 10^{-8}$

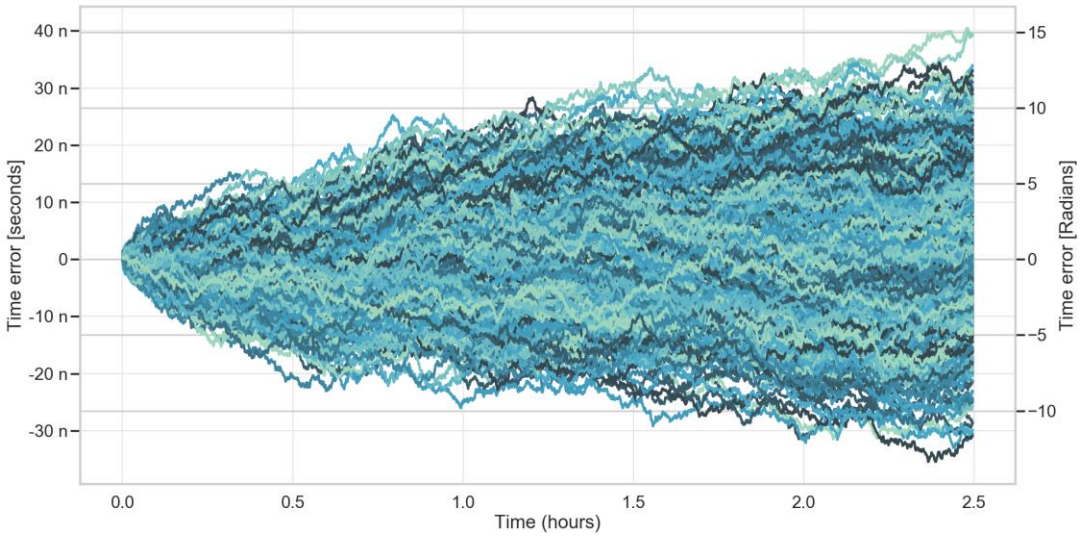

Figure 74. Accuracy of the reconstructed Lander time using 1 s between Pong transmissions and 1000 realizations.

In Figure 74 to 77 we show the test for the same parameters as the last analysis but incrementing the time between Pong-Pong to 1 second.

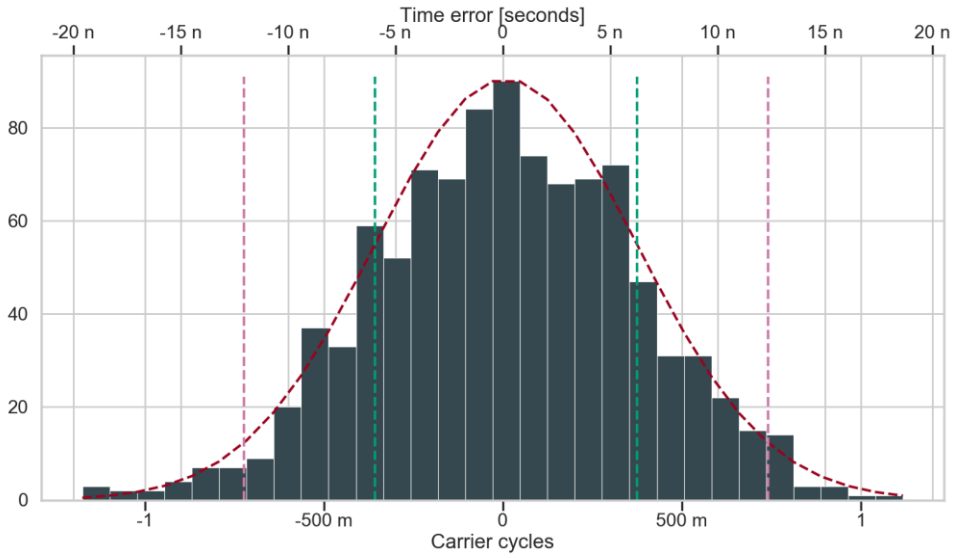

Figure 75. Distribution after 10 minutes for 1000 realizations with the time between Pongs being 1 second. $\sigma = 6.1 \times 10^{-9}, \mu = 1.47 \times 10^{-10}$ in seconds.

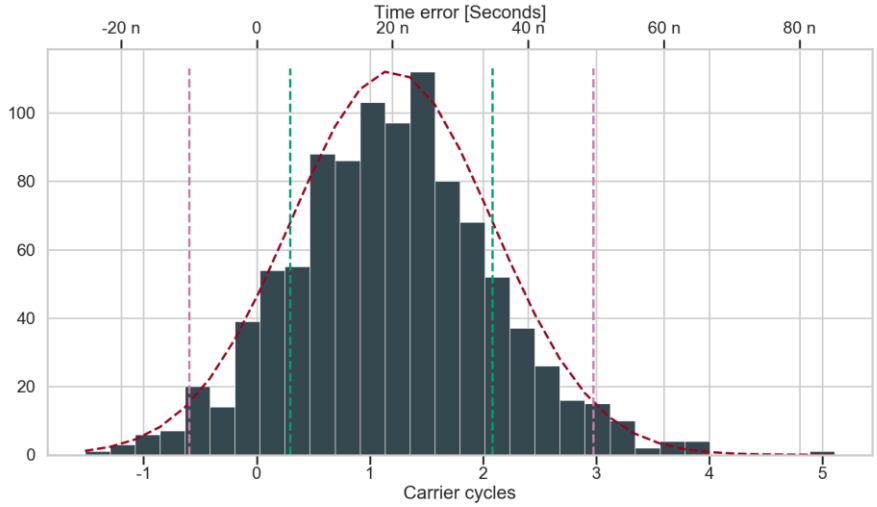

Figure 76. Distribution after 1 hour for 1000 realizations with the time between Pongs being 1 second. $\sigma = 1.48 \times 10^{-8}, \mu = 1.98 \times 10^{-8}$ in carrier cycles.

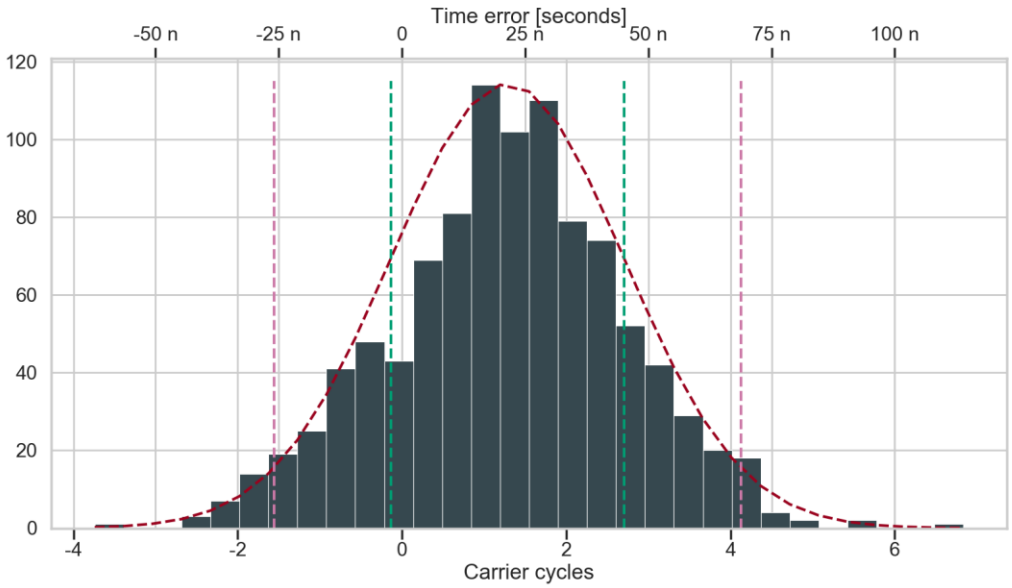

Figure 77. Distribution after 2.5 hours for 1000 realizations with the time between Pongs being 1 second. $\boldsymbol{\sigma = 2.36 \times 10^{-8}, \mu = 2.13 \times 10^{-8}}$

As we can see from the distributions, 0.5 seconds between Pong transmissions can hardly deliver the accuracy expected for the phase reconstruction. When using 1 second between Pong-Pong transmissions, the requirement of the time compensation between Soundings can be achieved with a 1σ probability. However, for 80° of the carrier andafter 1 hour, it is not possible unless the SNR could be improved. Nevertheless, the upper limit of the time between Pong transmissions has to be chosen with the actual relative speed between both electronics.

In Table 11 we list the standard distributions and mean values obtained by fitting a Gaussian function to the time errors after different times (10 min, 1hour and 2.5 hours) identical to the last plots, but in this case, allowing more times between Pong transmissions. This test was also performed for 1000 realizations for different ΔPP values.

We can observe that the mean value is very close to 0,tending to fluctuate slightly for different ΔPP of realization. The clear tendency of the distribution value is to get smaller as the time between Pong transmissions increases. This means that the accuracy of the estimation of the absolute time increases as the time between transmissions increases. With a time between transmissions of 4 seconds an accuracy to reconstruct the phase to 80° with 1 sigma could be reached. Nevertheless, as we

explained before the time between Pong transmissions will be limited directly by the relative movement between electronics. Therefore, a time between transmissions of 4 seconds is outside the possible values for times between transmissions. N.B. We included values above 1 second for clarity, even though these values are not expected to be possible because of the relative movement of the electronics.

Table 11. Standard deviation and mean values for different times between Pong transmissions using 40 dB of SNR and 1 second between Pong transmissions for 10 minutes, 1 hour and 2.5 h hours. Values in seconds.

ΔPP	$\sigma(t = 10\ min)$	$\mu(t = 10\ min)$	$\sigma(t = 1\ h)$	$\mu(t = 1\ h)$	$\sigma(t = 2.5\ h)$	$\mu(t = 2.5h)$
0.025	2.43×10^{-7}	-1.38×10^{-9}	5.68×10^{-7}	6.67×10^{-8}	9.4×10^{-7}	9.03×10^{-8}
0.10	5.93×10^{-8}	-2.63×10^{-9}	1.43×10^{-7}	4.15×10^{-8}	2.31×10^{-7}	4.88×10^{-8}
0.30	1.95×10^{-8}	-1.43×10^{-9}	4.73×10^{-8}	4.25×10^{-8}	7.75×10^{-8}	4.41×10^{-8}
0.50	1.15×10^{-8}	-1.66×10^{-9}	2.8×10^{-8}	3.44×10^{-8}	4.52×10^{-8}	4×10^{-8}
0.70	8.59×10^{-9}	-7.17×10^{-10}	2.09×10^{-8}	2.56×10^{-8}	3.22×10^{-8}	2.89×10^{-8}
1.0	6.1×10^{-9}	1.47×10^{-10}	1.48×10^{-8}	1.98×10^{-8}	2.36×10^{-8}	2.13×10^{-8}
2.0	2.86×10^{-9}	8.94×10^{-10}	7.06×10^{-9}	1.06×10^{-9}	1.18×10^{-8}	3.99×10^{-9}
4.0	1.54×10^{-9}	-9.2×10^{-10}	3.58×10^{-9}	7.33×10^{-9}	5.76×10^{-9}	5.1×10^{-9}

For clarity, the Figures 78 to 81 present the standard deviation of the accuracy of the reconstruction as a function of time of reconstruction. The standard deviation is obtained from 1000 realizations and for 4 different 1 hours lengths of the dataset. In Figure 78 and 80 we vary the time between Pong transmissions with a realistic SNR of 20 dB. In Figure 79 and 81 we vary the SNR with a realistic time between Pong transmissions of 1 second.

In Figure 78 is easy to see that the accuracy needed of approximately 3.7 ns is impossible to achieve for 1 hour even using a time between transmissions of 4 seconds. And in Figure 79 we can see that even with a very good SNR of 25 dB is also impossible for a 1 second between transmission to comply with the constraints.

In Figure 80 for times between transmissions greater than 1 second, it is possible to reconstruct time with an accuracy higher than the 8 nanoseconds for the 10 minutes requirement. For a 1 second time between transmissions, it is possible to reconstruct time for about 5 minutes (300 seconds) with an accuracy of 8.3 nanoseconds. It is impossible to reconstruct the phase with the accuracy needed by the requirement with a SNR of 20 dB.

In Figure 81 we can observe that for a 1 second transmission between Pong transmissions, we need a better SNR than 20 dB to reconstruct time of the requirements. A SNR of 20 dB can solely reconstruct the time for a period of 5 minutes as mentioned above. The phase reconstruction is impossible.

In conclusion, the accuracy of reconstruction is be heavily affected by the SNR of the received signal and by the possible times between transmissions. Depending on the relative speed between electronics we should choose the maximum time when considereing that the signal travels the same path. The SNR of the received signal will give us information about the accuracy of the possible reconstructions. The phase reconstruction seems to be impossible with the actual clock drift measurement and reconstruction model.

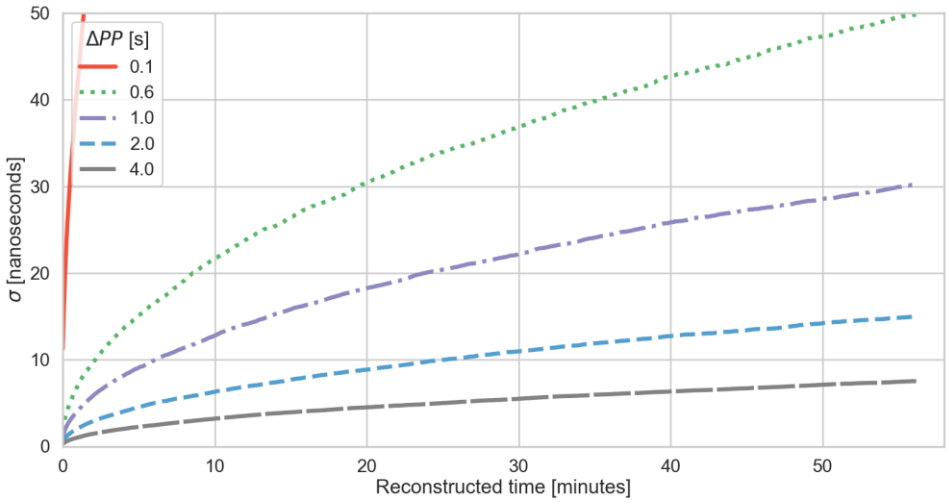

Figure 78. The standard deviation of the accuracy of the time reconstruction as a function of time for a SNR of 20 dB, varying the time between Pong transmissions for 1 hour.

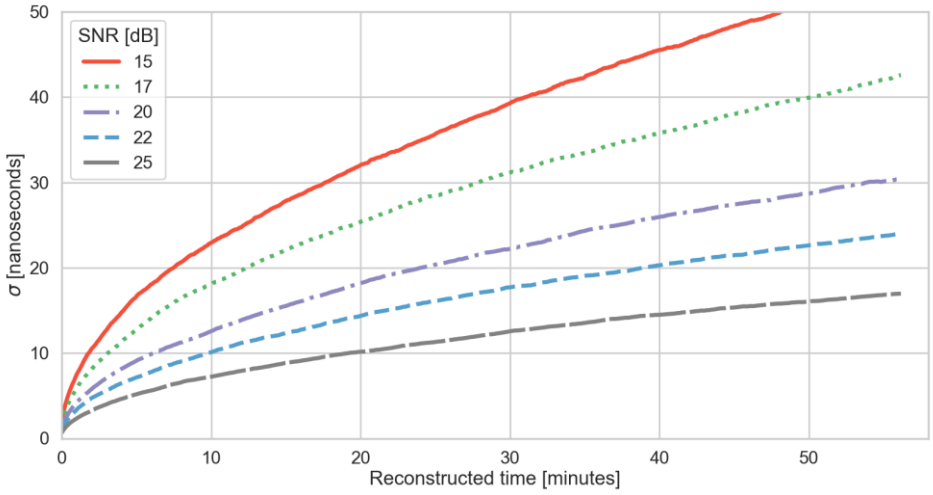

Figure 79. The standard deviation of the accuracy of time reconstruction for different SNR with 1 second between transmissions for 1 hour.

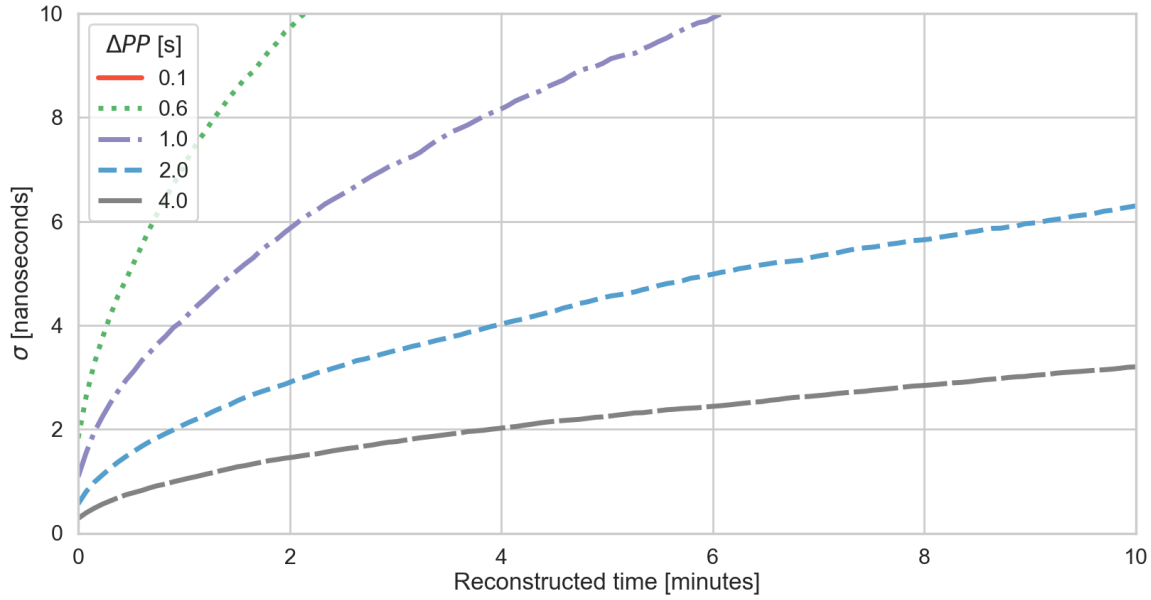

Figure 80. The standard deviation of the accuracy of the time reconstruction as a function of time for a SNR of 20 dB, varying the time between Pong transmissions for 10 minutes.

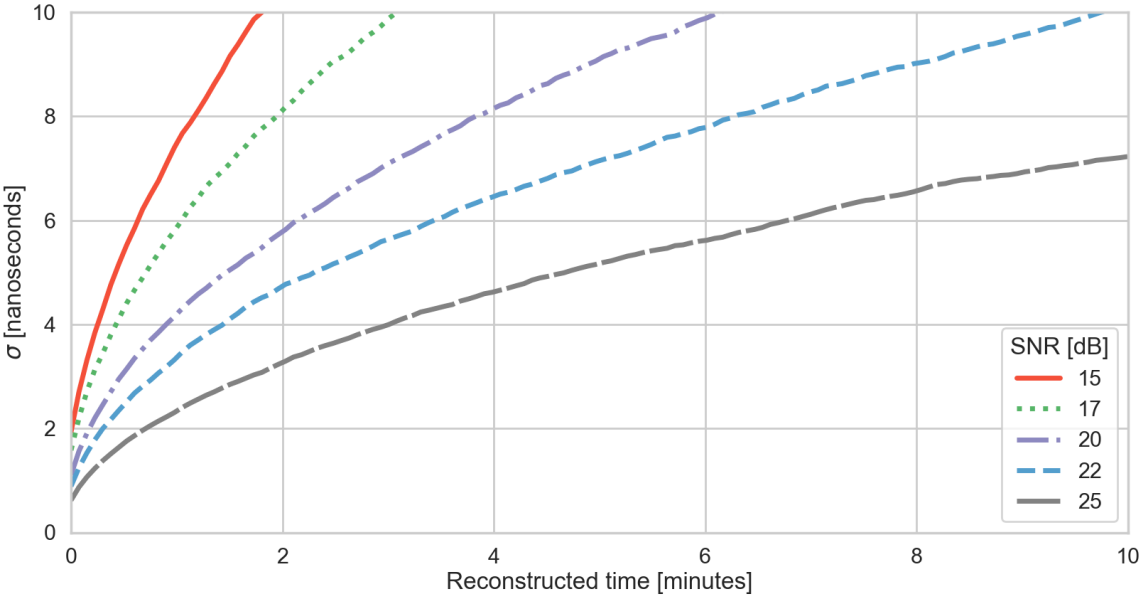

Figure 81. The standard deviation of the accuracy of time reconstruction for different SNR with 1 second between transmissions for 10 minutes.

Table 12. Standard deviation and mean values for different times between Pong transmissions using 1second between Pong transmissions for 10 minutes, 1 hour and 2.5 h hours. Values in seconds.

SNR	$\sigma(t = 10\ min)$	$\mu(t = 10\ min)$	$\sigma(t = 1\ h)$	$\mu(t = 1\ h)$	$\sigma(t = 2.5\ h)$	$\mu(t = 2.5h)$
0	6.28×10^{-7}	-1.39×10^{-8}	$1..5 \times 10^{-6}$	8.4×10^{-8}	2.3×10^{-6}	3.31×10^{-8}
5	1.9×10^{-7}	-7.66×10^{-9}	4.71×10^{-7}	3.55×10^{-9}	7.44×10^{-7}	-2.19×10^{-8}
10	5.89×10^{-8}	7.84×10^{-10}	1.47×10^{-7}	1×10^{-8}	2.35×10^{-7}	1.55×10^{-8}
15	1.86×10^{-8}	9.34×10^{-9}	4.5×10^{-8}	2.09×10^{-8}	7.17×10^{-8}	4×10^{-8}
20	5.78×10^{-9}	1.04×10^{-10}	1.49×10^{-8}	2.03×10^{-8}	2.42×10^{-8}	2.37×10^{-8}
25	1.84×10^{-9}	1.41×10^{-10}	4.68×10^{-9}	1.98×10^{-8}	7.01×10^{-9}	2.21×10^{-8}

6.2.4. Number of Pong-Pong transmissions

For the last test, we use less numbers of Pong-Pong transmissions. This means that the same value of the estimated clock drift value will be used for more Soundings, to reconstruct the time deviation between clocks.

In Figure 82 we can see that even a Pong-Pong transmission every 2 Soundings is not sufficient to maintain the same level of compensation as we have with a Pong-Pong transmission each Sounding.

N.B. This test was performed using the same random noise values for each number of Pong-Pong transmissions.

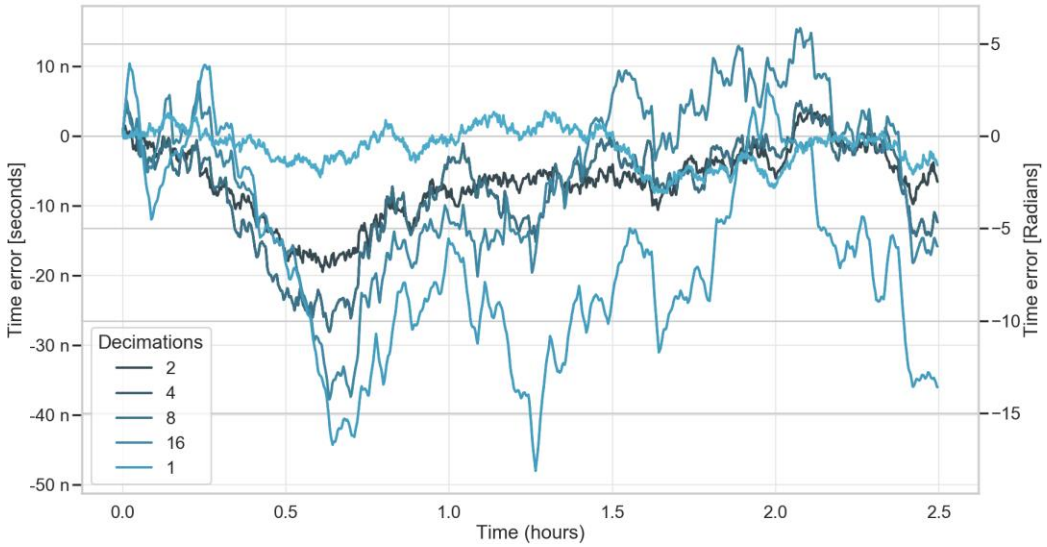

Figure 82. The error of the reconstructed Lander for different numbers of Pong-Pong transmissions during the Scan.

Chapter 7. Conclusions and perspectives

7.1. Time analysis advantages

The time analysis of the LFR instrument led to diverse knowledge for improvements for science return, electronic design and operation design. It, furthermore, brought us a better understanding of clocks and signal generation and, in particular, showed how the clock drift will affect the transponder operation and measurement.

The first step of the time analysis included an extensive review of the clock signal generation, as this component will be in charge of the main operation of the instrument timing. The understanding of the different types of parameters that could affect the signal generation was an important step towards the instrument improvement and validated the signal quality. This review provided a clock model that can be used to synthesize the time error between clocks by introducing possible parameters that will affect the frequency generated such as temperature, voltage supply, aging, short term stability, etc.

In the next step, we developed a time analysis of the transponder concept for long periods of time. This means that the shortest time scale (Coherent Accumulation) was not considered. This time model was based on time events, and it modeled the way the transponder concept operates. It was used to develop a simulator to synthesize the clock drift of the Lander clock against the Orbiter clock. This synthetic data helped us understand how errors will affect the transponder measurement. The time errors have different effects at each time scale but they are correlated. We recognized the specific effect of each process affecting the clock generation and their impact on the propagation delay measurement. Additionally, we were able to recreate the same phase rotation effect that was observed in the CONSERT calibration data, to which we compared the results when using the parameters of CONSERT in the simulator. This demonstrated that if the clock drift is a multiple of the sampling frequency and the time between Soundings the phase rotation is visible in the propagation delay measured in the Orbiter, which can be understood as a stroboscopic effect. Furthermore, for the comparison with the CONSERT calibration data we were able to observe the same type of distributions for the peak position measured in the Lander and the Orbiter. This comparision with real

data from the CONSERT calibration data validates the simulator implementation, as well as the model of the radar.

Using the time analysisa clock drift technique named Pong-Pong from the two propagations back to the Orbiter from the Lander was proposed. These two transmissions are constrained by the need to travel the same path. This technique will deliver the average clock drift between clocks during the time between transmissions. The simulator was also used to test the clock-drift-follow technique. This clock drift follow was used later to implement the compensation to the timing errors coming from the clocks.

As the simulator was used to understand different effects of the clock drift, the next step was the recollection of real data coming from the clocks to confirm all the conclusions obtained from the simulator. For this, a test bench was designed and developed. Extensive research of time measurement methods was performed for the selection of the test bench and a DMTD system was chosen as the most adequate system. The Test Bench opened the possibility not only to verify the models used in the simulator, but also to characterize the clocks and validate them for the mission.

The clocks were validated by comparing the requirements needed in terms of stability to achive the absolute requirements, Coherent Accumulation and Tx-Rx windows movement, as described in the time analysis section. In this case, the MAD analysis between both clocks was used to show that the noise is of the order of 10^{-9}, which is lower than the requirement of 10^{-7} for the Coherent Accumulation time scale. Nontheless, we think the phase noise measured at this time scale is the one coming from the test bench and not from the clocks. The accumulated time error measured by the Test Bench showed that after 17 hours the clock deviation for the three different tests with temperature movement is not larger than 1 millisecond. As a reminder, the time drift from the requirement was 10’s of milliseconds for 12 hours. We can, therefore, conclude that the absolute requirements are complied with, including a security margin and the clocks are suitable to be used for the project. In this case, we were only able to validate the Syrlinks clocks, however, we expectthe Rakon clock to show the same behavior.

For the validation of the three stability requirements we did further testings. For the Ping to Pong time scale we showed that the time between Ping and Pong for a typical 100 milliseconds time between reception and transmission in the Lander is no larger than 1.3×10^{-10}. The requirement described in the time analysis demanded a drift of less than 10^{-8}, so there will be no significant error introduced directly in the propagation delay.

For the other two stability requirements in the time scale of Sounding to Sounding, we first described the compensation methods for time and phase. For this, we first demonstrated the integration of the data collected by the test bench into the simulator and evaluated the possibility to measure the clock drift using the Pong-Pong technique. To test the clock drift estimation $\widehat{\Delta f}/f$ technique, the data coming from the test bench in form of time differences and accumulated time errors were introduced into the simulator. With this estimated clock drift $\widehat{\Delta f}/f$ it was possible to reconstruct the Lander times and, therefore, to reconstruct the absolute phase between clocks considering a deterministic model of the phase. The accuracy of the time reconstruction was directly linked to the time between Pong transmissions. The greater the time between transmissions the better the accuracy. This time between transmissions is limited by the relative movement between Orbiter and Lander, as we need to ensure that both transmissions use the same path. Additionally, the accuracy of the estimated clock drift was limited by the accuracy of the peak position measured in the Orbiter/Earth. One direct limitation of the Pong-Pong technique is the noise introduced by the SNR of the received signal. The time error that will be introduced in the peak position will directly affect the accuracy of the clock drift estimation. In this case, for the model proposed and for the time error introduced by the SNR of the received signal, it indicated a value of $\sigma = 3.83 \times 10^{-11}$ for a SNR of 40 dB. This value is an ideal SNR. In reality we will expect a 10 to 20 dB SNR which translates to $\sigma = 1.21 \times 10^{-9}\ to\ 3.83 \times 10^{-10}$. This means that the accuracy of the difference of the peak detection will be affected by the sum of these two peak position errors. If we consider a 1 second time between transmissions, which is the largest possible value of time between Pong transmissions, we resume that the accuracy of the clock drift is limited to an order of 10^{-10} to 10^{-9}.

The time and phase reconstruction models were tested by using the estimation of the clock drift and the simulator. In this case, we reconstructed the Lander drift against

the Orbiter reference. This tests showed that by increasing the time between the Pong transmissions, indeed, improved the accuracy of the reconstruction. Nevertheless, the accuracy of the clock drift estimation was not sufficient to reconstruct phase within the requirements established in the time analysis section. A moving average filter was used to improve the clock drift estimation but it was also not possible to achieve any significant compensation for SNR under 40 dB. For the time reconstruction we showed that it is possible for a SNR of 20 dB to reconstruct time for 5 minutes within the requirements established. With a better signal to noise ratio it is possible to reconstruct the time for 10 minutes. As stated in the requirements, during the direct sight of the instruments the SNR improves and, therefore, this technique could be used on-board to do an initial calibration as we will explain in the next section.

Another parameter that we explored was the reduction of Pong-Pong transmissions instead of sending a Pong-Pong every Sounding. We could expect that the physical variables affecting the clock drift could be considered constant for short terms of time, typically 10 Soundings. Therefore, we could only calculate the clock drift for some Soundings to save power and processing. The results showed that the accuracy of the time reconstruction was heavily affected if we did not measure the clock drift each Sounding.

New methods for the improvement of the clock drift estimation can be proposed such as the use of a Kalman filter to use information coming from the housekeeping, like temperature, or a different progression of transmissions, for example 3 Pong transmissions.

In the following we will review specific points that were improved from the CONSERT design and from the original design of LFR.

7.2. Instrument improvements (CONSERT - LFR)

7.2.1. Power consumption by Tx window

One of the time scales studied was the movement of the reception window inside of the transmission window. To allow communication, it was mandatory for the reception window to remain inside the transmission window. From the results of the accumulated time error it was possible to determine an interval of possible movements for the

reception window which was less than 1 millisecond for 17 hours. This means that we have one of the parameters for the selection of the transmission window length. The other parameter needed is the initial time synchronization between calendars. With these two values it is possible to establish the minimum window required. Nevertheless, some margins will be considered.

The importance of the optimization of the transmission window leys in its direct impact on the power consumption. The operation driving the power needed for the instrument is the transmission of the signal. Therefore, the optimization of the transmission window length will help reduce the power consumption budget.

7.2.2. ADC sampling frequency

The time analysis was useful for the realization that the 100 MHz sampling frequency for the incoming signal directlyintroduces a jitter error in the propagation delay measurement and in the phase. This is a result of the non synchronization of the reception and transmission paths. This problem was solved by selecting a 120 MHz sampling frequency.

7.2.3. Second version Test Bench

After the first tests with the test bench, we decided to improve the capacity and digital design of the bench to allow the characterization of 3 pairs of clocks at the same time. The digital design was, furthermore,modified so that instead of using specific counters for each measurement, a unique real-time clock driven by the reference clock signal would give the time stamps for every rising edge of the beat frequency of all beat signals generated. With this, it was possible to measure period and phase just by subtracting different timestamps. This also avoided the error of resetting the counters, and the change of string data transmission format allowed for more values to be transmitted without changing the baud rate.

Digital design

The digital design was modified in order to avoid the use of individual counters and use a unique real clock driven by the reference clock instead. The FPGA

timestamped the rising and descending edges for every Beat frequency. This value was then sent to the computer attaching a marker to sign the clock and the type of edge.

This design avoids any delay in resetting counters and uses only one reference for all the variables.

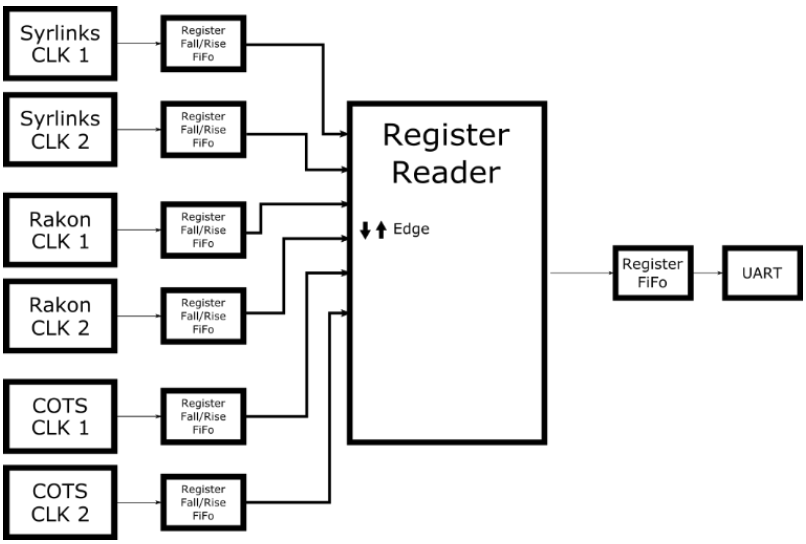

Figure 83. Block diagram for the Second version of the Test Bench. Each pair of clocks uses one clock as the reference for the master clock.

Hardware

The hardware now permits to connect 6 clocks at the same time in this case with 3 pairs of clocks: one pair from Rakon, one from Syrlinks and one commercial clock for comparison. The FPGA board counts with an interface board to connect all clocks and select between the internal and external PLL for the measurement. The first tests for the validation of the digital design implementation are already done. They were performed using only two frequency generatorsand showed fewer values missing in the file. In the next step, the technical team needs to finish the digital description to allow several clocks at the same time to start the characterization tests for both pairs of selected clocks (Rakon and Syrlinks).

During the writing ofthis thesis report, the second version of the test bench was almost finished for testing. Each clock box includes temperature, voltage, and current sensors, which will allow for characterizing the clock in all the parameters described in

the next section. Additionally, it will allow for the selection between the internal or external PLL with a simple switch selection. The clock boxes have been tested including the 3 types of sensors, and the test bench has already done preliminary tests using frequency generators as the inputs. The data presents few errors and is promising to enable the possibility of characterizing 3 pairs of clocks at the same time.

7.3. Perspectives

7.3.1. Clock characterization

The Test Bench data can be used directly for characterizing the clocks. By using the phase data and converting it to fractional frequency, it can be analyzed with the Allan Variance analysis to characterize the variation with temperature and the aging dependence. These are the parameters driving the stability in the long term.

For this, we propose a test in which both clocks are under the same temperature conditions during the same amount of time to characterize aging. A second test where one clock is subject to a steady temperature while the other is subject to drastic temperature changes by using a freezer device is also proposed. By subtracting the aging effect calculated in the first test from that in the second test, it is possible to retain only the temperature variations.

This tests will permit the characterization of the clock against the temperature and aging parameters, which are the ones imposing the principal variations on the frequency.

Another important parameter to characterize from the clock behavior is the retrace of the clocks. As the clocks can be turned off and on during the mission between Scans, this can change their frequency every time the clocks are turned on again. Characterizing this behavior can give insight into the differences between Scans that are not related to the other parameters. We propose to add the retrace effect by turning on and off the clocks while performing exactly the same tests explained above.

Characterizing the warm-up time is fundamental to provide the minimum time needed by the clocks to reach the specified stability. This characterization includes power in terms of voltage and current consumption, and the stabilization time. This

information is vital for the calibration methods as we have to turn on clocks before science is started to be sure that the clocks have reached the stability needed by the requirements.

For this, we have to take into account that the test bench could have some failures in the data transmission to the PC. As the transmission rate is linked to the frequency of the clocks, if they suffer a fast change at the beginning of the operationthe data transmission could be affected.

By including voltage and current sensors for each clock in the second version of Test Bench, we can characterize how the power consumption varies with the time and temperature variations. This will be a way to validate the power budget used for the clocks, and to characterize Pong-Pong techniques in terms of power needed.

7.4. Calibration

Before separation, a frequency calibration should be performed to compensate for any aging effect during the trip. From the datasheet for the Rakon clock, we can expect a lifetime change of 300 ppb or a 3×10^{-7} change in the frequency. The Rakon clock has the possibility to readjust the frequency with a variation of 400 ppb which is sufficient to compensate for the deviation acquired during travel time.

For the Syrlinks clock, we expect a 100 ppb change per year and a possible correction of 600 ppb.

It is important to remember the possibility that both clocks undergo a similar aging process and don't deviate one from another as much as they possibly could in the worst-case scenario.

The calibration process to be used to readjust the frequency before separation is a subject of current studies. We gave first insights in the analysis in the perspectives section, where we talked about the use of the Pong-Pong and a filter scheme to improve the clock drift measurement and use it on-board for calibration purposes.

During the mission there is no plan to do frequency calibrations for each Scan as proposed for CONSERT. After the initial calibration, and depending on the duration of

the mission, the clock datasheet values allow us to be relatively certain that aging will not take the frequency stability beyond its constraints. Nevertheless, aging and temperature parameters can be characterized by using the Test Bench to guarantee the compliance of the requirements. This characterization of the clock will be explained in the next section.

The knowledge acquired from the CONSERT calibration is that it is difficult to guarantee a high SNR to lock the PLL to the pure sine signal to match the frequencies during the mission. The PLL depends completely on a good SNR to be able to lock, and if that is not the case, it is possible for this type of calibration to have a negative effect.

For LFR, it is possible to use the Pong-Pong technique and a filter to improve the clock drift measurement. The method used in direct line-of-sight offers a better response to the SNR than the PLL lock mode.

During the phase mission in the asteroid, if there is no need for calibration every single Scan, there is room to extend the data science time, which will offer some calibration measurements before and after the occultation by the asteroid. This calibration measurement helps to improve the knowledge of the Lander delay between reception and transmission in case of any eventuality.

7.4.1. Calibration and onboard correction

One possible scenario to reduce costs and power consumption could be the use of smaller and cheaper clocks that could be compensated on board in real-time. This compensation can also be used as the frequency calibration method. By using the Pong-Pong technique and a filtering scheme, it is possible to readjust the frequency of one of the clocks to match the other during the whole mission.

For this, we can propose a Kalman filtering scheme, which could also use data from the housekeeping such as the temperature to help improve the estimation, considering that frequency stability varies linearly with the temperature.

A Kalman filter is optimal for calibration on board, as it uses just one prior calculated value and the actual input from the variables, meaning there is no need of storing huge amounts of data or big calculation resources.

Beside Kalman filtering, other methods of estimation to improve the measurement of the clock drift exist. These methods are usually used in data science, and specifically in machine learning applied to estimation and prediction of highly unstable variables as in meteorological models: Lasso Regression, Tree regression, Sine model.

It is possible to think of other types of sequences to help improve the clock drift estimation, e.g. repeating consecutive 3 Pong transmissions — in this case, we can have 3 different time differences between all the transmissions to help improve the clock drift estimation.

7.4.2. New clock technologies

The appearance of new types of clocks could converge in a better stability clock. The new Space micro atomic clock could comply with the constraints of planetary mission and offer good long term frequency stability. Even though the short term stability and phase noise is larger in the atomic reference clocks, these noise levels are below the constraints posed by the planetary mission.

One example of these new clocks is the Microsemi, Chip-Scale Atomic Clock (CSAC). By the specifications it is one or two orders of magnitude better in frequency stability +/-0.5 ppb, change for temperature and aging of 10ppb per year than the clocks selected for this project However, it exhibits a lower phase noise profile starting with -50 dBc/Hz at 1 Hz and reaching a noise floor of -140 dBc/Hz at 100 kHz. The only constraint for this clock could be the temperature range of operation since its lowest working temperature is -10 °C. The temperature expected for the electronic box on the Lander will reach -20 °C, which could put the clock out of the operational temperatures. Lastly, the price is attractive to the project being of the order of 5k euros.

References

Allan, D. W. (1966). Statistics of atomic frequency standards. *Proceedings of the IEEE*, *54*(2), 221–230. https://doi.org/10.1109/PROC.1966.4634

Allan, D. W., & Daams, H. (1975). Picosecond Time Difference Measurement System. *29th Annual Symposium on Frequency Control*, 404–411. https://doi.org/10.1109/FREQ.1975.200112

Allan, D. W., Howe, D. A., Walls, F. L., & Sullivan, D. B. (1990). *Characterization of clocks and oscillators* (No. NBS TN 1337). https://doi.org/10.6028/NIST.TN.1337

Ballato, A., & Vig, J. R. (1978). Static and Dynamic Frequency-Temperature Behavior of Singly and Doubly Rotated, Oven-Controlled Quartz Resonators. *32nd Annual Symposium on Frequency Control*, 180–188. https://doi.org/10.1109/FREQ.1978.200236

Barbin, Y., Kofman, W., Nielsen, E., Hagfors, T., Seu, R., Picardi, G., & Svedhem, H. (1999). The CONSERT instrument for the ROSETTA mission. *Advances in Space Research*, *24*(9), 1115–1126. https://doi.org/10.1016/S0273-1177(99)80205-1

Barucci, M. A., & Fulchignoni, M. (2017). Major achievements of the Rosetta mission in connection with the origin of the solar system. *The Astronomy and Astrophysics Review*, *25*(1), 3. https://doi.org/10.1007/s00159-017-0103-8

Biele, J., & Ulamec, S. (2008). Capabilities of Philae, the Rosetta Lander. In H. Balsiger, K. Altwegg, W. Huebner, T. Owen, & R. Schulz (Eds.), *Origin and Early Evolution of Comet Nuclei: Workshop honouring Johannes Geiss on the occasion of his 80th birthday* (pp. 275–289). https://doi.org/10.1007/978-0-387-85455-7_18

Biele, Jens, Ulamec, S., Maibaum, M., Roll, R., Witte, L., Jurado, E., … Spohn, T. (2015). The landing(s) of Philae and inferences about comet surface mechanical

properties. *Science*, *349*(6247), aaa9816. https://doi.org/10.1126/science.aaa9816

BIPM - revision of the SI. (n.d.). Retrieved January 14, 2019, from https://www.bipm.org/en/measurement-units/rev-si/#communication

Boden, R. C., Hein, A. M., & Kawaguchi, J. (2015). Target selection and mass estimation for manned NEO exploration using a baseline mission design. *Acta Astronautica*, *111*, 198–221. https://doi.org/10.1016/j.actaastro.2015.02.018

Britt, D. T., & Consolmagno, G. J. S. J. (2003). Stony meteorite porosities and densities: A review of the data through 2001. *Meteoritics & Planetary Science*, *38*(8), 1161–1180. https://doi.org/10.1111/j.1945-5100.2003.tb00305.x

Brown, P. G., Assink, J. D., Astiz, L., Blaauw, R., Boslough, M. B., Borovička, J., … Krzeminski, Z. (2013). A 500-kiloton airburst over Chelyabinsk and an enhanced hazard from small impactors. *Nature*, *503*(7475), 238–241. https://doi.org/10.1038/nature12741

Campo Bagatin, A., Alemañ, R. A., Benavidez, P. G., & Richardson, D. C. (2018). Internal structure of asteroid gravitational aggregates. *Icarus*, *302*, 343–359. https://doi.org/10.1016/j.icarus.2017.11.024

Carter, G. C. (1987). Coherence and time delay estimation. *Proceedings of the IEEE*, *75*(2), 236–255. https://doi.org/10.1109/PROC.1987.13723

Chapman, C. R. (2004). The hazard of near-Earth asteroid impacts on earth. *Earth and Planetary Science Letters*, *222*(1), 1–15. https://doi.org/10.1016/j.epsl.2004.03.004

Cheng, A. F., Santo, A. G., Heeres, K. J., Landshof, J. A., Farquhar, R. W., Gold, R. E., & Lee, S. C. (1997). Near-Earth Asteroid Rendezvous: Mission overview. *Journal of Geophysical Research: Planets*, *102*(E10), 23695–23708. https://doi.org/10.1029/96JE03364

Ciarletti, V., Herique, A., Lasue, J., Levasseur-Regourd, A.-C., Plettemeier, D., Lemmonier, F., … Kofman, W. (2017). CONSERT constrains the internal structure of 67P at a few metres size scale. *Monthly Notices of the Royal Astronomical Society*, *469*(Suppl_2), S805–S817. https://doi.org/10.1093/mnras/stx3132

Davis, J. L., & Annan, A. P. (1989). Ground-Penetrating Radar for High-Resolution Mapping of Soil and Rock Stratigraphy1. *Geophysical Prospecting*, *37*(5), 531–551. https://doi.org/10.1111/j.1365-2478.1989.tb02221.x

Ferri, P., Accomazzo, A., Hubault, A., Lodiot, S., Pellon-Bailon, J.-L., & Porta, R. (2012). Rosetta enters hibernation. *Acta Astronautica*, *79*, 124–130. https://doi.org/10.1016/j.actaastro.2012.04.045

Gehrels, T. (1971). *Physical studies of minor planets*. Retrieved from https://ntrs.nasa.gov/search.jsp?R=19720018103

Glassmeier, K.-H., Boehnhardt, H., Koschny, D., Kührt, E., & Richter, I. (2007). The Rosetta Mission: Flying Towards the Origin of the Solar System. *Space Science Reviews*, *128*(1–4), 1–21. https://doi.org/10.1007/s11214-006-9140-8

Heggy, E., Palmer, E. M., Kofman, W., Clifford, S. M., Righter, K., & Hérique, A. (2012). Radar properties of comets: Parametric dielectric modeling of Comet 67P/Churyumov–Gerasimenko. *Icarus*, *221*(2), 925–939. https://doi.org/10.1016/j.icarus.2012.09.023

Hellwig, H. (1977). *Frequency standards and clocks: A tutorial introduction*. Retrieved from http://adsabs.harvard.edu/abs/1977fsct.book.....H

Herique, A., Agnus, B., Asphaug, E., Barucci, A., Beck, P., Bellerose, J., … Zine, S. (2017). Direct observations of asteroid interior and regolith structure: Science measurement requirements. *Advances in Space Research*. https://doi.org/10.1016/j.asr.2017.10.020

Herique, A., Agnus, B., Asphaug, E., Barucci, A., Beck, P., Bellerose, J., … Zine, S. (2018). Direct observations of asteroid interior and regolith structure: Science measurement requirements. *Advances in Space Research*, *62*(8), 2141–2162. https://doi.org/10.1016/j.asr.2017.10.020

Herique, A., Kofman, W., Beck, P., Bonal, L., Buttarazzi, I., Heggy, E., … Zine, S. (2016). Cosmochemical implications of CONSERT permittivity characterization of 67P/CG. *Monthly Notices of the Royal Astronomical Society*, *462*(Suppl_1), S516–S532. https://doi.org/10.1093/mnras/stx040

Herique, Alain, Plettemeier, D., Lange, C., Grundmann, J. T., Ciarletti, V., Ho, T.-M., … Ulamec, S. (2019). A radar package for asteroid subsurface investigations: Implications of implementing and integration into the MASCOT nanoscale landing platform from science requirements to baseline design. *Acta Astronautica*, *156*, 317–329. https://doi.org/10.1016/j.actaastro.2018.03.058

Herique, Alain, Rogez, Y., Pasquero, O. P., Zine, S., Puget, P., & Kofman, W. (2015). Philae localization from CONSERT/Rosetta measurement. *Planetary and Space Science*, *117*, 475–484. https://doi.org/10.1016/j.pss.2015.08.020

Ho, T.-M., Baturkin, V., Grimm, C., Grundmann, J. T., Hobbie, C., Ksenik, E., … Okada, T. (2017). MASCOT—The Mobile Asteroid Surface Scout Onboard the Hayabusa2 Mission. *Space Science Reviews*, *208*(1), 339–374. https://doi.org/10.1007/s11214-016-0251-6

Housen, K. (n.d.). *Asteroid Density, Porosity, and Structure*. 16.

Howe, D. A., Allan, D. U., & Barnes, J. A. (1981). Properties of Signal Sources and Measurement Methods. *Thirty Fifth Annual Frequency Control Symposium*, 669–716. https://doi.org/10.1109/FREQ.1981.200541

IEEE Standards Coordinating Committee 27 (SCC27) on Time and Frequency, IEEE-SA Standards Board, & Institute of Electrical and Electronics Engineers. (2009).

IEEE standard definitions of physical quantities for fundamental frequency and time metrology—Random instabilities. Retrieved from http://ieeexplore.ieee.org/servlet/opac?punumber=4797523

Jacobson, S. A., & Scheeres, D. J. (2011). Dynamics of rotationally fissioned asteroids: Source of observed small asteroid systems. *Icarus*, *214*(1), 161–178. https://doi.org/10.1016/j.icarus.2011.04.009

Kay, S. M. (1993). Fundamentals of statistical signal processing. Retrieved March 6, 2019, from CERN Document Server website: https://cds.cern.ch/record/2012069

Kofman, W., Barbin, Y., Klinger, J., Levasseur-Regourd, A.-C., Barriot, J.-P., Herique, A., … Williams, I. P. (1998). Comet nucleus sounding experiment by radiowave transmission. *Advances in Space Research*, *21*(11), 1589–1598. https://doi.org/10.1016/S0273-1177(97)00952-6

Kofman, W., Herique, A., Goutail, J.-P., Hagfors, T., Williams, I. P., Nielsen, E., … Svedhem, V. (2007). The Comet Nucleus Sounding Experiment by Radiowave Transmission (CONSERT): A Short Description of the Instrument and of the Commissioning Stages. *Space Science Reviews*, *128*(1–4), 413–432. https://doi.org/10.1007/s11214-006-9034-9

Kofman, Wlodek, Herique, A., Barbin, Y., Barriot, J.-P., Ciarletti, V., Clifford, S., … Zyl, J. V. (2015). Properties of the 67P/Churyumov-Gerasimenko interior revealed by CONSERT radar. *Science*, *349*(6247), aab0639. https://doi.org/10.1126/science.aab0639

Kraus, J. D. (1986). *Radio Astronomy* (2nd ed.). Powell, Ohio: Cygnus-Quasar.

Lauretta, D. S., Balram-Knutson, S. S., Beshore, E., Boynton, W. V., Drouet d'Aubigny, C., DellaGiustina, D. N., … Sandford, S. A. (2017). OSIRIS-REx: Sample Return from Asteroid (101955) Bennu. *Space Science Reviews*, *212*(1), 925–984. https://doi.org/10.1007/s11214-017-0405-1

Michel, P., Cheng, A., Küppers, M., Pravec, P., Blum, J., Delbo, M., … Yu, Y. (2016). Science case for the Asteroid Impact Mission (AIM): A component of the Asteroid Impact & Deflection Assessment (AIDA) mission. *Advances in Space Research*, *57*(12), 2529–2547. https://doi.org/10.1016/j.asr.2016.03.031

MIL-PRF-55310F. (n.d.).

Missions to asteroids. (n.d.). Retrieved November 14, 2018, from http://sci.esa.int/rosetta/54342-missions-to-asteroids/

Moreira, P., Alvarez, P., Serrano, J., & Darwazeh, I. (2012). Sub-nanosecond digital phase shifter for clock synchronization applications. *2012 IEEE International Frequency Control Symposium Proceedings*, 1–6. https://doi.org/10.1109/FCS.2012.6243715

Moreira, P., Alvarez, P., Serrano, J., Darwezeh, I., & Wlostowski, T. (2010). Digital dual mixer time difference for sub-nanosecond time synchronization in Ethernet. *2010 IEEE International Frequency Control Symposium*, 449–453. https://doi.org/10.1109/FREQ.2010.5556289

Nakamura, T., Noguchi, T., Tanaka, M., Zolensky, M. E., Kimura, M., Tsuchiyama, A., … Kawaguchi, J. (2011). Itokawa Dust Particles: A Direct Link Between S-Type Asteroids and Ordinary Chondrites. *Science*, *333*(6046), 1113–1116. https://doi.org/10.1126/science.1207758

O'Rourke, L., Tubiana, C., Güttler, C., Lodiot, S., Muñoz, P., Herique, A., … Gaudon, P. (2019). The search campaign to identify and image the Philae Lander on the surface of comet 67P/Churyumov-Gerasimenko. *Acta Astronautica*, *157*, 199–214. https://doi.org/10.1016/j.actaastro.2018.12.035

Palmer, E. M., Heggy, E., & Kofman, W. (2017). Orbital bistatic radar observations of asteroid Vesta by the Dawn mission. *Nature Communications*, *8*(1), 409. https://doi.org/10.1038/s41467-017-00434-6

Pasquero, O. P., Hérique, A., & Kofman, W. (2017). Oversampled Pulse Compression Based on Signal Modeling: Application to CONSERT/Rosetta Radar. *IEEE Transactions on Geoscience and Remote Sensing*, *55*(4), 2225–2238. https://doi.org/10.1109/TGRS.2016.2639449

Psyche Mission – A Mission to a Metal World. (n.d.). Retrieved November 15, 2018, from Psyche Mission website: https://psyche.asu.edu/

Reinhard, R. (1986). *The Giotto encounter with comet Halley*. 6.

Richardson, D. C., Leinhardt, Z. M., Melosh, H. J., Jr, W. F. B., & Asphaug, E. (n.d.). *Gravitational Aggregates: Evidence and Evolution*. 15.

Riley, W. J., & Riley, W. J. (2008). *Handbook of frequency stability analysis* (No. NIST SP 1065). https://doi.org/10.6028/NIST.SP.1065

Rogez, Y., Puget, P., Zine, S., Hérique, A., Kofman, W., Altobelli, N., … Vallat, C. (2016). The CONSERT operations planning process for the Rosetta mission. *Acta Astronautica*, *125*, 212–233. https://doi.org/10.1016/j.actaastro.2016.03.010

Rubiola, E. (2008). *Phase Noise and Frequency Stability in Oscillators* (2010th ed.). Cambridge University Press.

Russell, C. T., Raymond, C. A., Ammannito, E., Buczkowski, D. L., Sanctis, M. C. D., Hiesinger, H., … Yamashita, N. (2016). Dawn arrives at Ceres: Exploration of a small, volatile-rich world. *Science*, *353*(6303), 1008–1010. https://doi.org/10.1126/science.aaf4219

Siddiqi, A. A. L. (2002). *Deep Space Chronicle: A Chronology of Deep Space and Planetary Probes 1958-2000*. Retrieved from https://ntrs.nasa.gov/search.jsp?R=20020052429

Skolnik, M. I. (Ed.). (2008). *Radar handbook* (3. [rev.] ed). New York, NY: McGraw Hill.

Taylor, M. G. G. T., Altobelli, N., Buratti, B. J., & Choukroun, M. (2017). The Rosetta mission orbiter science overview: The comet phase. *Philosophical Transactions*

of the Royal Society A: Mathematical, Physical and Engineering Sciences, *375*(2097), 20160262. https://doi.org/10.1098/rsta.2016.0262

Tsuda, Y., Yoshikawa, M., Saiki, T., Nakazawa, S., & Watanabe, S. (2018). Hayabusa2–Sample return and kinetic impact mission to near-earth asteroid Ryugu. *Acta Astronautica*. https://doi.org/10.1016/j.actaastro.2018.01.030

Uesugi, M., Ito, M., Yabuta, H., Naraoka, H., Kitajima, F., Takano, Y., … Karouji, Y. (2019). Further characterization of carbonaceous materials in Hayabusa-returned samples to understand their origin. *Meteoritics & Planetary Science*, *54*(3), 638–666. https://doi.org/10.1111/maps.13236

Ulamec, S., Biele, J., Blazquez, A., Cozzoni, B., Delmas, C., Fantinati, C., … Witte, L. (2015). Rosetta Lander – Philae: Landing preparations. *Acta Astronautica*, *107*, 79–86. https://doi.org/10.1016/j.actaastro.2014.11.019

Veverka, J., Farquhar, B., Robinson, M., Thomas, P., Murchie, S., Harch, A., … Wellnitz, D. (2001). The landing of the NEAR-Shoemaker spacecraft on asteroid 433 Eros. *Nature*, *413*(6854), 390–393. https://doi.org/10.1038/35096507

Vig, J. R., & Meeker, T. R. (1991). The aging of bulk acoustic wave resonators, filters and oscillators. *Proceedings of the 45th Annual Symposium on Frequency Control 1991*, 77–101. https://doi.org/10.1109/FREQ.1991.145888

Walker, J. D., Sagebiel, E. J., & Huebner, W. F. (2006). A preliminary analysis of seismological techniques to study Eros and other asteroids. *Advances in Space Research*, *37*(1), 142–152. https://doi.org/10.1016/j.asr.2005.07.084

Watanabe, S., Tsuda, Y., Yoshikawa, M., Tanaka, S., Saiki, T., & Nakazawa, S. (2017). Hayabusa2 Mission Overview. *Space Science Reviews*, *208*(1), 3–16. https://doi.org/10.1007/s11214-017-0377-1

Appendix A.

Analysis of data from test bench

Data files are read and converted from hexadecimal strings to decimal numbers. If any string fails to convert to decimal due to missing elements in the line or errors, this line is marked as missing. Each line contains one value of each Counter sent every time the Period of the Beat reference clock has a rising edge.

Data file is verified by searching missing lines. This is done with the help of the last value sent by the FPGA that is counter of lines sent by the FPGA. This function only searches for changes more than once in the line number. If the change is larger than one it raises a flag and marks the line number in the file and the last and actual number of the line to know the number of lines missing.

Then the file is separated into 1M lines files for easier access. And separated by countertype: period, phase, etc.

7.5. Processing

7.5.1. Missing Lines

The data transmitted from the FPGA to the computer has the value of a counter that increments every transmission. This means we have the number of the sample transmitted. This value is used to verify the integrity of the data received. We verify the incremental continuity in this value to verify the complete reception of data. If any value of any counters missing, the line is considered lost.

For most of the files, there is a range of 300 to 600 missing samples in each counter in a file of 100M samples. And this happens in groups of 20 to 40 continue samples, this means we lost between 20 to 40 milliseconds of data approximately in a file of 27 hours. To replace the missing lines, an interpolation is performed using 100 values before and after the missing value and all the Counter values in that transmission are calculated. So we consider that the missing values don’t represent any problem to

the analysis as the time elapsed by this missing values is too short and the interpolation can have a good approximation of the missing values.

The discrepancy in the number of missing samples and position over the files is not well-understood, but we concluded that the Baud Rate between computer and Test Bench could vary, causing a mismatch and loss of lines.

7.5.2. Period

The data from the Period counters is multiplied by the inverse of the frequency of the clock used in the counter, in our case the CLK1 to have an exact value of 10 MHz.

$$T_{beat} = T_{counter} \frac{1}{f_{CLK1}}$$

The mean value of this data set is the period that we will consider for the Beat signal. The better the clocks, the system and the synthesis of the PLL the closer it should be to 1 kHz. In this case, the external PLL delivers a frequency almost 1 kHz different from the original clock creating a 1000.3 Hz Beat signal Figure 84.

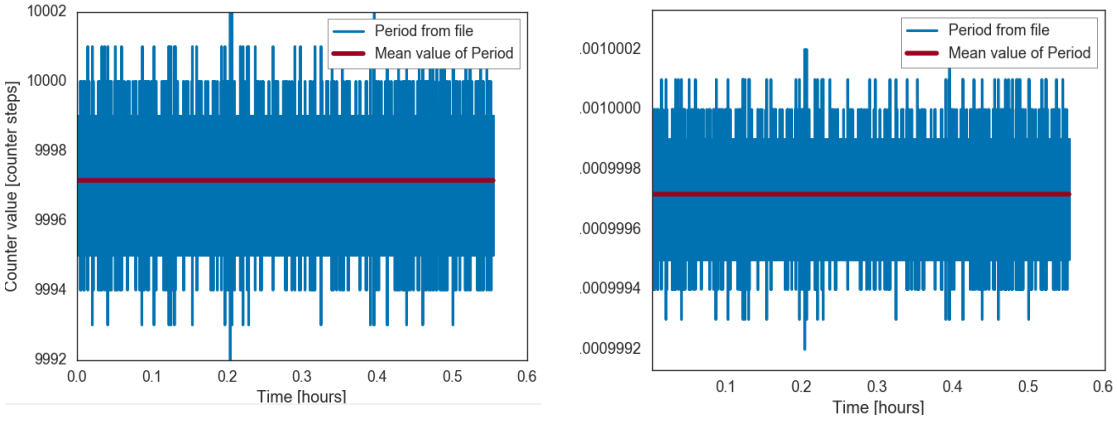

Figure 84. Period, direct from file with counter value and converted into time. (testfile_7.12.2018.8.28)

7.5.3. Phase

The first step into the time difference data is to unfold the accumulated error.

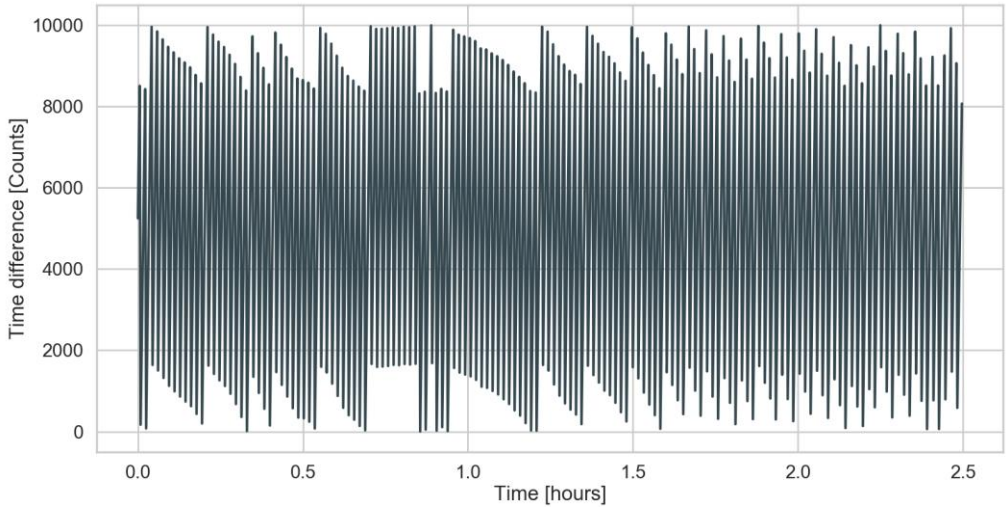

Figure 85. Time difference measured by the Counters.

To convert this value to accumulated time error first we need to unfold the time difference.

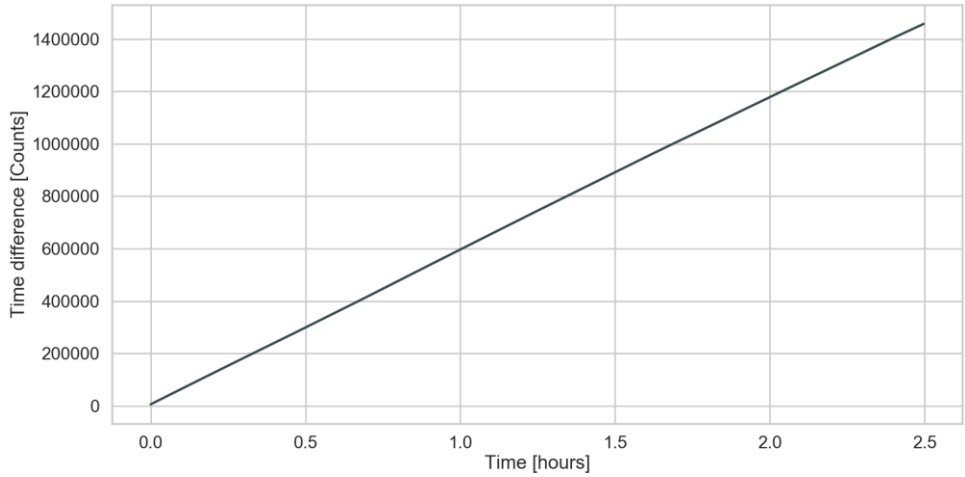

Figure 86. The unfolded time difference in Counter counts.

To convert this counter value into time in seconds, this value is divided by the value of the frequency of the clock used for the counter, in our case the PLL output frequency. And to this, we include the zooming effect of the DMTD which is the ratio between the beat frequency and the nominal frequency of the reference clock.

$$\Delta t = \Delta_{counter} \frac{1}{f_{PLL}} \frac{f_{beat}}{f_{CLK}}$$

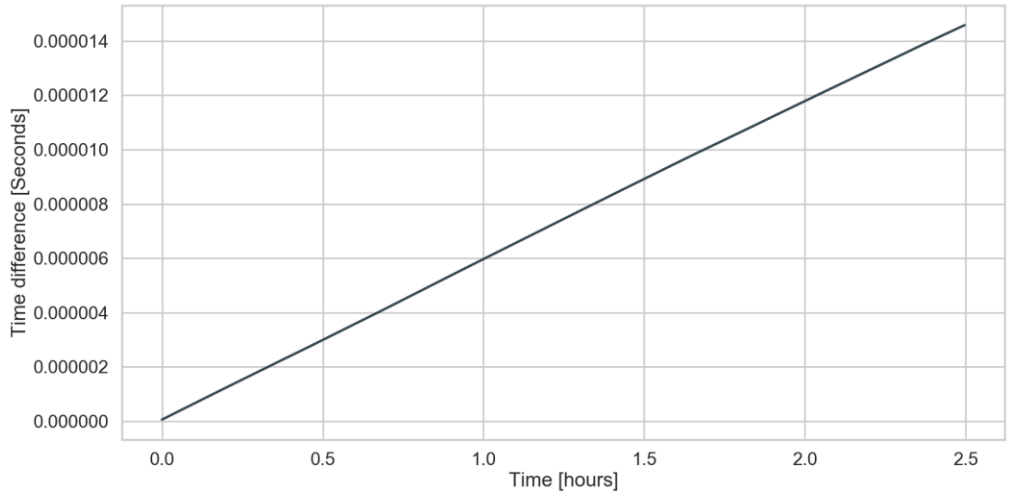

Figure 87. The unfolded time difference in Seconds, which accounts as the accumulated time error between both clocks.

Now with this accumulated time error and knowing the nominal frequency is possible to obtain the phase error between both clocks for the complete measurement.

7.6. One clock test

The one clock test is used to obtain the floor noise of the test bench. In this case, both inputs receive the same clock with the same noise, and the PLL synthesizes the common clock synchronized to the only clock. If the two inputs are not delayed the noise coming from the clock is negligible and the only noise in an Allan Variance analysis is the one generated by the test bench.

First, the data must be plotted to search outliers that could compromise the analysis. If any, this outliers can be corrected via interpolation of the adjacent values. Then an analysis with Allan or modified Allan variance can give the type of noise that is embedded in the system. For this, the phase data is converted to fractional frequency, the difference of contiguous phase values divided by the time between samples. This value is a dimensionless quantity.

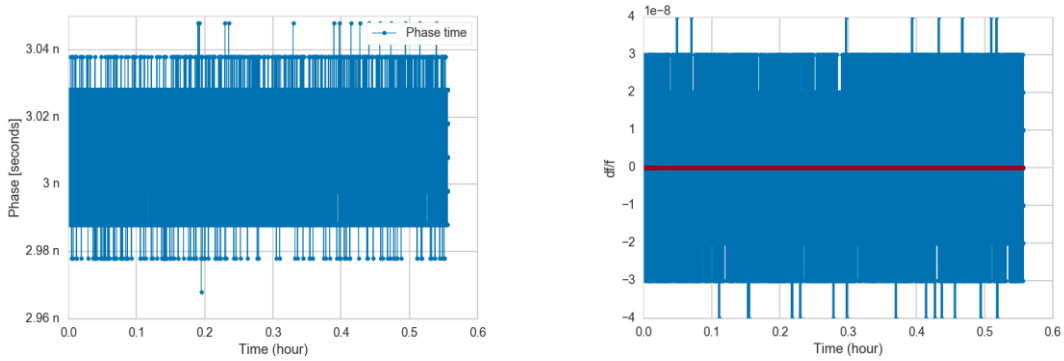

Figure 88. Phase in time and the conversion to fractional frequency. (testfile_7.12.2018.8.28)

The fractional frequency is then used for the modified Allan variance analysis. From the Allan Variance is possible to see that it cannot distinguish between white phase noise and white frequency noise. But the modified Allan version shows that the noise before 0.1 seconds is white phase noise. After that we notice some ripple in the Allan plot. This means that in the data we have a periodic noise. This noise for this test is referred completely to the external PLL. When using the FPGA internal PLL (with integer dividers) this process is not observed in the plot.

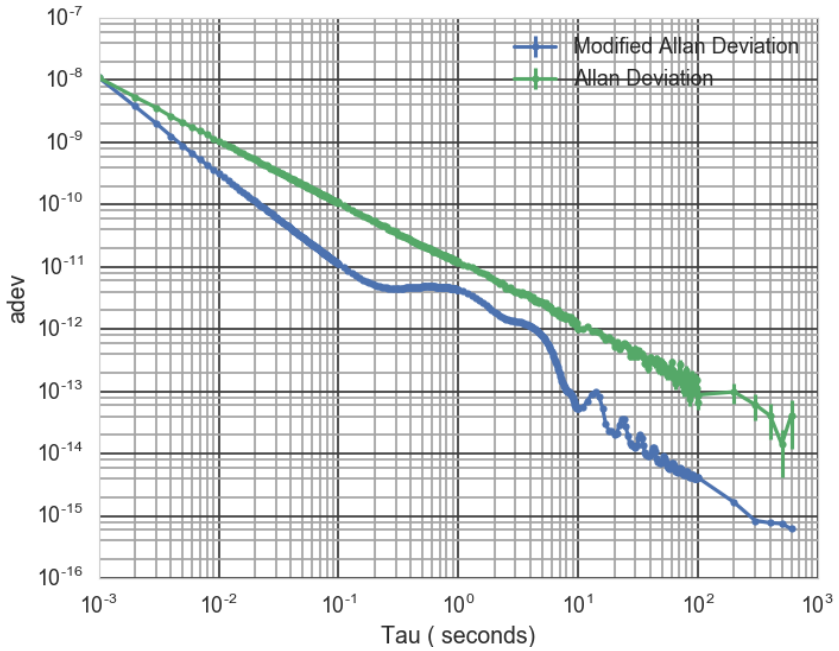

Figure 89. Modified and Allan Deviation, for the fractional frequency data.

For the files, the noise in the range of millisecond to hours the noise proves to be totally white phase noise. Meaning that the normal standard deviation and mean value are the best descriptors for the noise.

The noise is suspected to come directly from the FPGA PLL and from the glitch effect caused by the “fast” rising edges.

7.7. Two clock tests with fridge

For this test one clock was inside a fridge the fridge can be used from -40 to -18 °C. In our case the fridge was used from -30 to-18 °C, being -30°C the minimum temperature for operation of the clock. The other clock and the FPGA board were at an ambient temperature ranging from 28 to 35 °C (summer weather).

In this case, we notice how the phase between both clocks derives one from the other. Period of the reference clock is equal to the one observed in the one clock test.

The fractional frequency plot shows no drift. After fitting a line to the fractional frequency data, we observe that the slope is almost negligible for our time scale in the order of 10^{-18} and the frequency difference between both clocks is 6.31×10^{-9}.

Moving average completely reduces the Allan variance plot, by 3 orders of magnitude with a 1000 points average. Even though with this average the fractional frequency plot doesn’t show any relation with the temperature, the plot did in fact show more movement than without the average but it not follows completely the temperature curve.

Appendix B.

Random Noise generation from phase noise profile

The phase noise is often expressed with a sum of power-law noises, the most often encountered in an oscillator are the $1/f$ and f^0 noises, known as flicker and white frequency noises, but it will depend on the clock to know which type of noise is present. So a general model includes all five different noise types where i could go from 0 to 4.

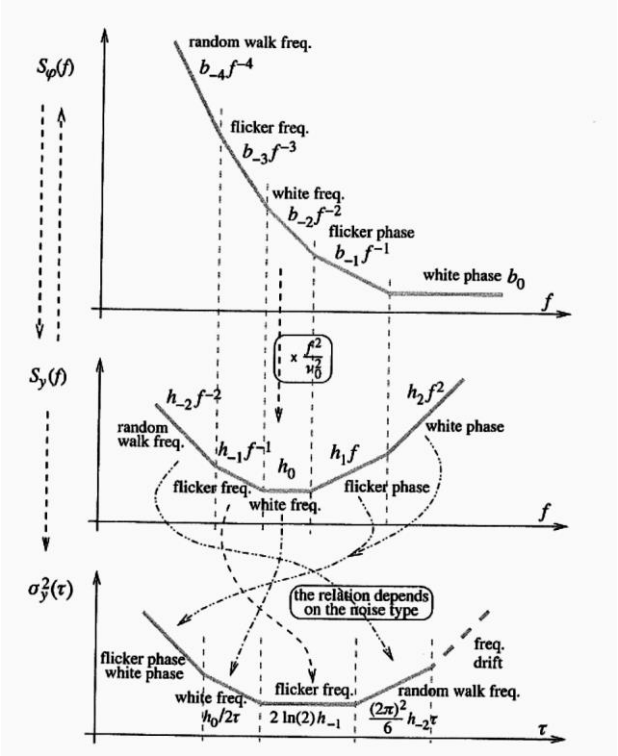

Figure 90. The relation between phase spectrum, frequency spectrum and Allan Variance (Rubiola, 2008).

So the power spectral law of phase noise is expressed like:

$$S_{\varphi_i}(f) = \sum_{\substack{i=-4 \\ or\ less}}^{0} b_i f^i$$

Or another form in terms of the fractional frequency where the exponent of the frequency ranges between –2 and 2

$$S_{y_i}(f) = \sum_{i=-2}^{2} h_i f^i$$

Where $S_y(f)$ denotes the spectral density of the fractional frequency random fluctuations and the fractional frequency is:

$$y_i = \frac{dx_i}{dt}$$

Which is a dimensionless quantity and where τ is the interval of time between samples. There are some forms to transform these frequency-domain values into time domain:

Noise type	$S_{\varphi}(f)$	σ_y^2
White Phase	$b_0 f^0$	$\frac{3 f_H b_0}{(2\pi)^2} \frac{f^0}{f_0^2} \frac{1}{\tau^2}$
Flicker Phase	$b_{-1} f^{-1}$	$[1.038 + 3\ln(2\pi f_H \tau)] \frac{b_{-1}}{f_0^2} \frac{f^1}{(2\pi)^2 \tau^2}$
White Frequency	$b_{-2} f^{-2}$	$\frac{1}{2} \frac{b_{-2}}{f_0^2} \frac{f^2}{\tau}$
Flicker Frequency	$b_{-3} f^{-3}$	$\frac{2\ln(2)}{f_0^2} b_{-3} f^3$
Random Walk Frequency	$b_{-4} f^{-4}$	$\frac{(2\pi)^2}{6 f_0^2} b_{-4} \tau f^4$

Where b_i is the power amplitude of each noise type, f^n is the frequency in the phase noise profile and f_H is the cutoff frequency of a low pass filter needed for the noise to remain finite.

Noise generation

Taking the data coming from a common datasheet of an oscillator, we can find the phase noise profile. In Figure XX we show a common phase profile found in datasheets of oscillators.

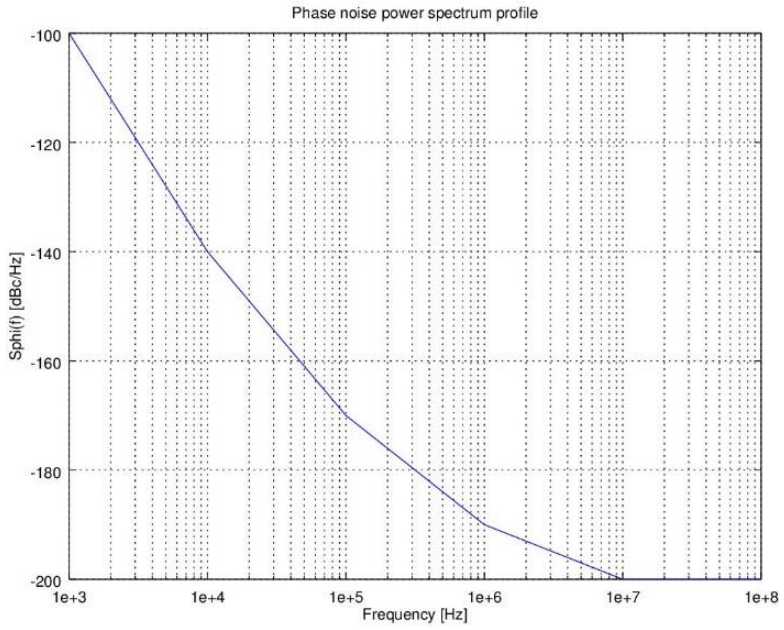

Figure 91. Phase noise profile

This plot represents the single sideband to have the complete power of the profile

$$\mathcal{L}(f) = \frac{1}{2} S_{\varphi}(f)$$

If the plot is given in dB it is also possible to do

$$S_{\varphi}(f) = \mathcal{L}(f) + 3dB$$

The conversion between frequency and phase spectrum is as follows

$$S_y(f) = \frac{f^2}{v_0^2} S_{\varphi}(f)$$

Converting the phase noise profile to a frequency spectrum.

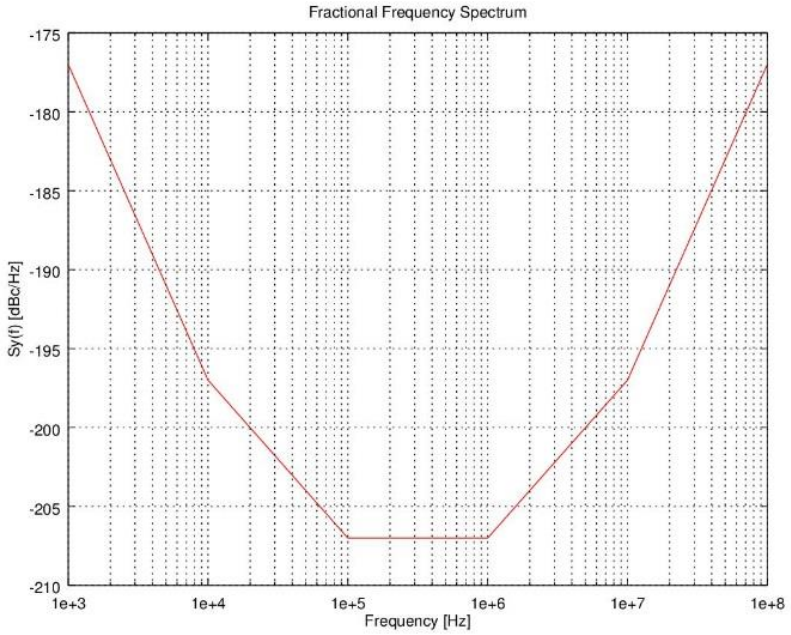

Figure 92. Fractional frequency profile obtained from phase profile noise.

These noise profiles are measured in Hz from the carrier and from 0 dB of the signal.

For this to complete the profile we can add the 0 Hz frequency with a 0 dB power to include the carrier component.

Depending on the number of points of noise needed we can interpolate the values to create. We create 2 Gaussian distributed random numbers. One of this will be considered the real part and the other the imaginary part, we will multiply this random complex number with the phase profile. We must take care that $f(Nyquist)$ should always be real. To obtain a real-valued time series the negative part of the spectrum should be the complex conjugation of the positive spectrum. This complete spectrum can be then transformed with the inverse Fourier transform to obtain a time series in time domain.

To test the Noise generator we can create all the different type of noises in the power law, and analyze it with the Allan Variance and observe If the slope corresponds to the expected noise.

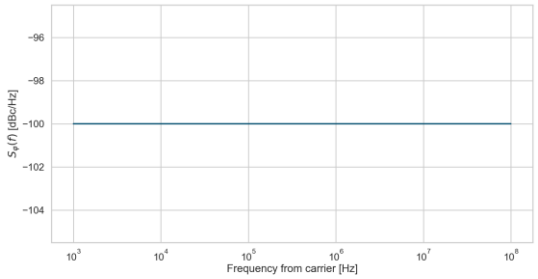

−96
−98
−100
−102
−104
$S_\varphi(f)$ [dBc/Hz]
10^3
10^4
10^5
10^6
10^7
10^8
Frequency from carrier [Hz]

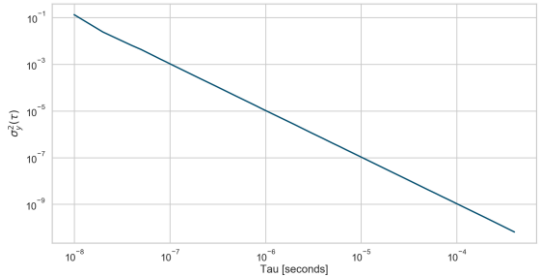

10^{-1}
10^{-3}
10^{-5}
10^{-7}
10^{-9}
$\sigma_y^2(\tau)$
10^{-8}
10^{-7}
10^{-6}
10^{-5}
10^{-4}
Tau [seconds]

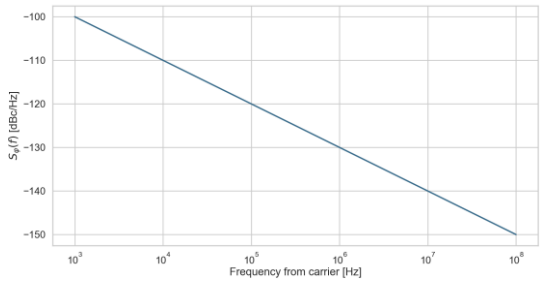

−100
−110
−120
−130
−140
−150
$S_\varphi(f)$ [dBc/Hz]
10^3
10^4
10^5
10^6
10^7
10^8
Frequency from carrier [Hz]

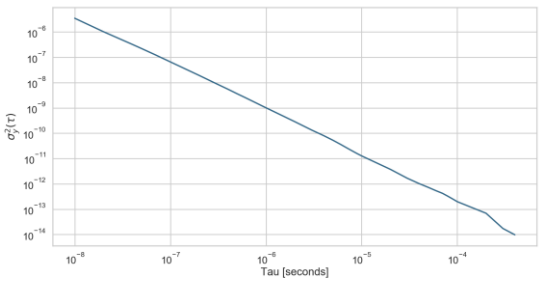

10^{-6}
10^{-7}
10^{-8}
10^{-9}
10^{-10}
10^{-11}
10^{-12}
10^{-13}
10^{-14}
$\sigma_y^2(\tau)$
10^{-8}
10^{-7}
10^{-6}
10^{-5}
10^{-4}
Tau [seconds]

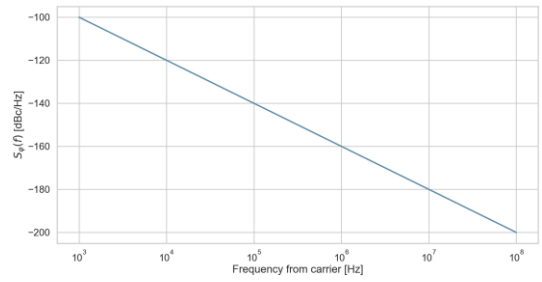

−100
−120
−140
−160
−180
−200
$S_\varphi(f)$ [dBc/Hz]
10^3
10^4
10^5
10^6
10^7
10^8
Frequency from carrier [Hz]

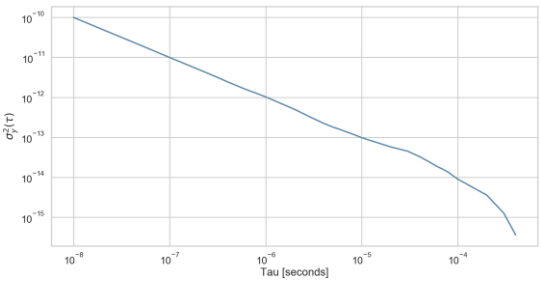

10^{-10}
10^{-11}
10^{-12}
10^{-13}
10^{-14}
10^{-15}
$\sigma_y^2(\tau)$
10^{-8}
10^{-7}
10^{-6}
10^{-5}
10^{-4}
Tau [seconds]

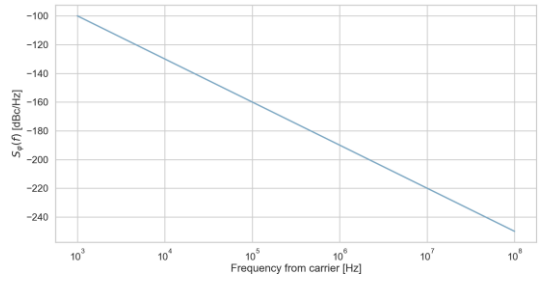

−100
−120
−140
−160
−180
−200
−220
−240
$S_\varphi(f)$ [dBc/Hz]
10^3
10^4
10^5
10^6
10^7
10^8
Frequency from carrier [Hz]

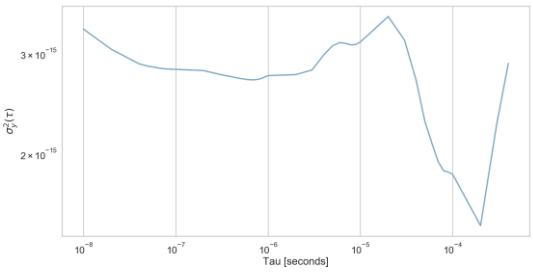

3×10^{-15}
2×10^{-15}
$\sigma_y^2(\tau)$
10^{-8}
10^{-7}
10^{-6}
10^{-5}
10^{-4}
Tau [seconds]

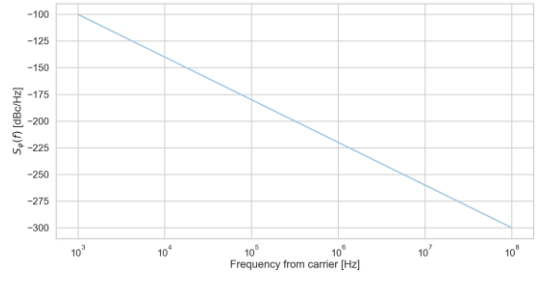

−100
−125
−150
−175
−200
−225
−250
−275
−300
$S_\varphi(f)$ [dBc/Hz]
10^3
10^4
10^5
10^6
10^7
10^8
Frequency from carrier [Hz]

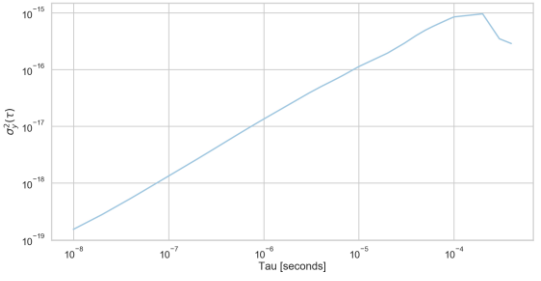

10^{-15}
10^{-16}
10^{-17}
10^{-18}
10^{-19}
$\sigma_y^2(\tau)$
10^{-8}
10^{-7}
10^{-6}
10^{-5}
10^{-4}
Tau [seconds]

Appendix C. Coherent accumulation requirement definition

We consider a complex sinusoidal signal

$$s(t) = e^{j(\omega t)} = \cos(\omega t) + j \cdot \sin(\omega t)$$

Going discrete

$$s(nT_s) = \cos(\omega n T_s) + j \cdot \sin(\omega n T_s)$$

For an accumulation of M codes with time period each code of $\mathcal{T}$,

$$\mathcal{T} = symbol\ time \cdot number\ of\ symbols$$

$$s_{Acc}(nT_s) = \sum_{m=0}^{M-1} C\big(\omega(nT_s - \mathcal{T}m)\big)\big[e^{j\omega(nT_s - \mathcal{T}m)}\big]$$

Where $C(nT_s - \mathcal{T}m)$ is the code signal multiplying the periodic complex signal.

As the signal is periodical the power is defined as

$$p_{s_{Acc}}(t) = \lim_{N\to\infty} \frac{1}{N} \sum_{n=0}^{N-1} |s_{Acc}(nT_s)|^2$$

Where $N = C/T_s$

For a random signal with normal distribution and zero mean the accumulation of N consecutive pieces of signal

$$n_{Acc}(t) = \sqrt{N}\sigma$$

While the power

$$p_{n_{Acc}}(t) = N\sigma^2$$

And the SNR

$$SNR = \frac{p_{s_{Acc}}(t)}{p_{n_{Acc}}(t)}$$

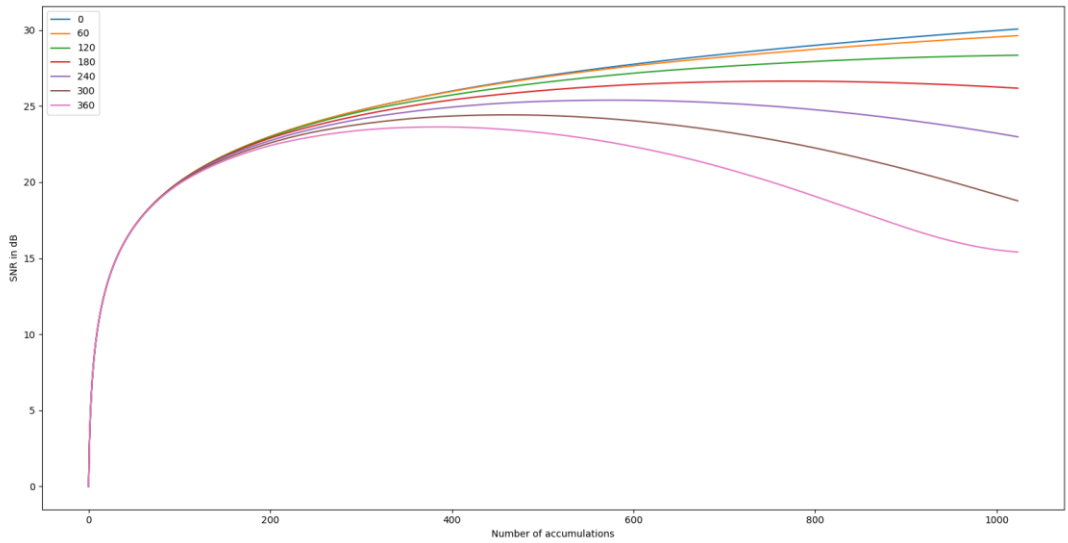

Figure 93. SNR between white Gaussian noise and accumulation of signal with clock drift. Each line represents the total phase shift of the signal at the end of the 1024 accumulation.

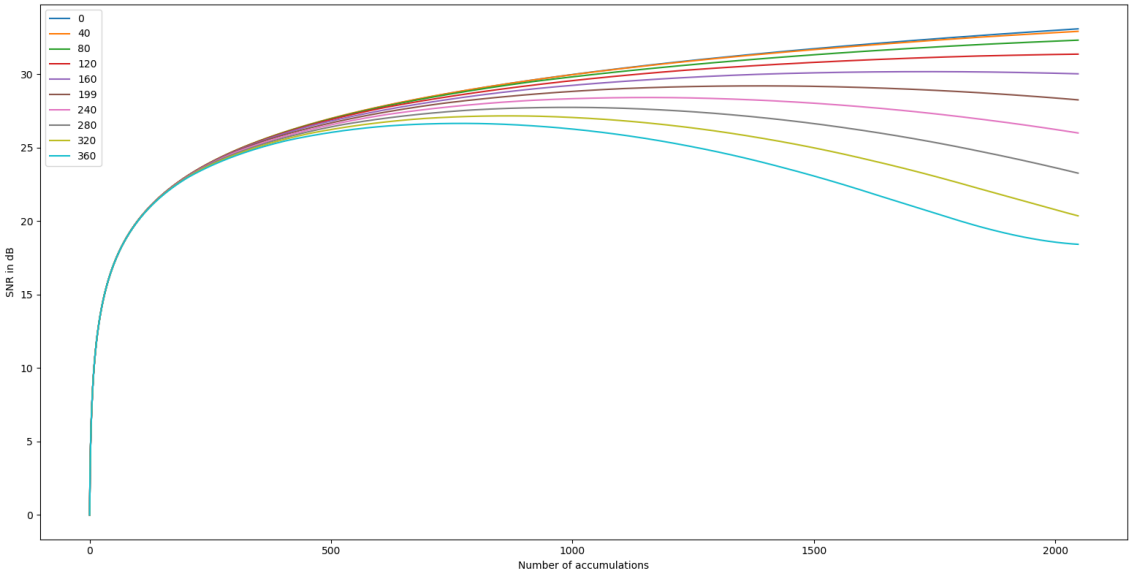

Figure 94. SNR between white Gaussian noise and accumulation of signal with clock drift. Each line represents the total phase shift of the signal at the end of the 2048 accumulation.

The 3dB drop from the no drift to the ones with drift occurs in 160° for 1024 codes accumulated. For 2048 accumulated codes the 3 dB drop is for 80°.

Appendix D. Data sets

The datasets gathered by the first version of the test bench are not extensive. Most of the data sets used in this thesis were collected for 24 hours, almost at the same times. Trying to be the most homogenous possible. During the gathering of the data, the test bench suffered diverse modifications in the digital design due to some problems in the saving of the data. Therefore some datasets contained some errors and it was used the part of the file that was not corrupted. The decision for the test bench improvement was taken after the first results with the first version. And as the second version of the test bench took more time than expected, the available data for the processing was limited.

The first six datasets were used for the floor noise analysis of the test bench, the 3 data sets with the use of the fridge were used to test the temperature sensor integrated with the boards of the clocks. And for a first approximation over the temperature drift impact. The last data set in the table was used to validate use of the external PLL as an input in the board. Therefore this test was not as long as the others.

Data set	Number of clocks	PLL type	Fridge	Duration
Data Set A In	1	Internal	No	27 hrs.
Data Set B In	1	Internal	No	27 hrs.
Data Set C In	1	Internal	No	27 hrs.
Data Set A Ex	1	External	No	27 hrs.
Data Set B Ex	1	External	No	27 hrs.
Data Set B Ex	1	External	No	27 hrs.
Data Set A diff	2	Internal	Yes	27 hrs.
Data Set B diff	2	Internal	Yes	27 hrs.
Data Set C diff	2	Internal	Yes	27 hrs.
Data Set A diffEx	2	External	No	2.5 hrs.